UNIVERSITY OF CALIFORNIA

Los Angeles

In situ Studies of Zn and ZnO Growth Kinetics during Electrodeposition

A dissertation submitted in partial satisfaction of the

Requirements for the degree of Doctor of Philosophy

in Materials Science and Engineering

by

Dian Yu

2017

ABSTRACT OF THE DISSERTATION

In situ Studies of Zn and ZnO Growth Kinetics during Electrodeposition

by

Dian Yu

Doctor of Philosophy in Materials Science and Engineering

University of California, Los Angeles, 2017

Professor Suneel Kodambaka, Chair

Electrodeposition of Zn and ZnO have attracted attention from both academia and industry because of their broad applications in energy storage and optoelectronic devices. The goal of this dissertation work is to develop fundamental understanding of the growth kinetics of Zn and ZnO during electrodeposition.

In situ characterization techniques are employed for the investigation of Zn and ZnO electrodeposition kinetics. First, Zn dendrite formation and oscillatory growth were analyzed using *in situ* optical microscopy. Second, the morphological evolutions of Zn and ZnO during electrodeposition were studied with *in situ* atomic force microscopy. Finally, the phases involved in and the mechanism underlying the ZnO electrodeposition were revealed by *in situ* wide-angle X-ray scattering and *in situ* electrochemical quartz crystal microbalance measurements.

In this dissertation, I investigated the morphological evolution of Zn dendrites during electrodeposition and developed fundamental insights to the growth behavior, which then set the foundation for the study of Zn growth kinetics under oscillatory conditions. A growth model for spontaneous oscillatory Zn dendrite growth was suggested based on the considerations of growth

dynamics and structural characteristics. The understanding of Zn growth kinetics was then achieved by direct monitoring the nucleation and growth on both poly- and single- crystalline substrates. In addition, a pH-dependent morphological evolution was observed during Zn growth, triggering the studies of ZnO electrodeposition, whereby ZnO formation was demonstrated to be an electrochemical induced chemical precipitation process. *In situ* observations of ZnO nucleation and growth allowed me to understand the electrochemical reaction pathways leading to the formation of ZnO during electrodeposition.

The dissertation of Dian Yu is approved.

Mark S. Goorsky

Yunfeng Lu

Suneel Kodambaka, Committee Chair

University of California, Los Angeles

2017

Table of Contents

List of Figures

List of Tables

List of Movies

Acknowledgment

First of all, I would like to acknowledge my advisor, Prof. Suneel Kodambaka, for his support throughout my academic and professional endeavors. I would also like to thank him for guiding and motivating me in pursuing my research in the right direction. Also, I would like to extend my appreciation to Prof. Mark Goorsky, Prof. Yunfeng Lu and Prof, Jenn-Ming Yang for serving as members of my dissertation committee.

I gratefully acknowledge Dr. Christine Orme for being my co-advisor and mentoring me at Lawrence Livermore National Laboratory. I would like to thank her for showing me, by her example, what a good scientist should be. I am also grateful that Dr. Christine Orme granted her wholehearted support in my personal and academic endeavors.

I am also indebted to Dr. Yixuan Yu, who has provided a lot of help during my last year in Lawrence Livermore National Laboratory, especially during the writing of this dissertation. I would also like to thank him for the friendship and moral support.

I would like to thank the research staff and graduate student at University of California, Los Angeles for helping me out with my research. I would especially thank Mr. Chao Li, Mr. Noah Bodzin, Ms. Tingyu Bai, Dr. Sergey Prikhodko, Dr. Ivo Atanisov and Dr. Goorsky for providing experimental resource and essential help for my research. I would also like to thank the research and administrative staff at Lawrence Livermore National Laboratory who have offered help during my stay.

I would like to thank my group members, Dr. Chilan Ngo, Dr. Abbas Ebnonassir, Mr. Michael chin, Mr.Pedro Arias, Mr. Josh Fankhauser, Mr. Hongyang Li, for their help on my research. For the fellow students, Dr. Charlotte Chou, Dr. Xiao Ma, Ms. Yuan Lin, I would like to

thank them for always being there for me. Finally, I would like to thank my parents for their encouragement, inspiration and selfless support.

Vita

2012	B.S., Materials Science and Engineering, Southeast University, Nanjing, China
2013	M.S., Materials Science and Engineering, University of California, Los Angeles

Publication

- D. Yu, Y. Yu, S. Kodambaka, and C. Orme, "New Insights into the Electrodeposition Kinetics of ZnO" *manuscript*
- D. Yu, Y. Yu, S. Kodambaka, and C. Orme, "*In situ* Atomic Force Microscopy studies of Electrodeposition Kinetics of Zn" *manuscript*
- D. Yu, C. Orme, and S. Kodambaka "*In situ* optical microscopy study of dendrite formation during Zn electrodeposition in sulfate solution" *manuscript*
- Y. Yu, D. Yu, and C. Orme, "Reversible, Tunable, Electric Field-Driven Assembly of Silver Nanocrystal Superlattices" *Nano Letters* **17**, 3862-3869 (2017).
- Y. Yu, D. Yu, and C. Orme, "Electric Field Driven Assembly of Supracrystals Probed with *in situ* Space-/Time-resolved Small Angle X-ray Scattering" *manuscript*
- Y. Yu, D. Yu, and C. Orme, "Interaction between Nanocrystal and Substrate Switches Superlattice Structure between Face Centered Cubic and Body Centered Tetragonal" *In progress*
- J. Fankhauser, M. Sato, D. Yu, A. Ebnonnasir, M. Kobashi, M.S. Goorsky, and S. Kodambaka, "Growth and Characterization of Epitaxial Zr (0001) Thin Films on Al2O3 (0001)" *Journal of Vacuum Science & Technology A: Vacuum, Surfaces, and Films* **34**, 050606(2016).

Chapter 1

1 Introduction

Rechargeable batteries have been an integral part of our society since the invention of lead-acid batteries in the mid-1800s.[1] Recently, with the growing demand for clean and sustainable energy, recyclable and rechargeable batteries have received renewed attention.[2]

A rechargeable battery is an electrochemical storage device, where electrical energy is stored and released in chemical bonds via redox reactions. When a battery discharges, the metal electrode oxidizes and releases electrons. To restore electrical energy in a rechargeable battery, an external current is applied to reverse the reactions and reduce the metal ions. As a result, each charge-discharge cycle involves deposition and dissolution of metal at the electrode.

Among the rechargeable batteries, metal-air batteries are considered promising because of their high energy density, reliable lifetime, minimal environmental impact, and low cost. In metal-air batteries, metal is the anode and oxygen gas is the cathode with an aqueous, non-aqueous, or a solid electrolyte. Of all the metal-air battery systems, Li-air and Zn-air are extremely attractive because of their high energy densities.[3] While Li is highly reactive with water, Zn is relatively more stable and desirable because of its mild response to moisture, low cost, abundance, and easy manufacturability. However, the drawbacks associated with Zn-based batteries include relatively low operating potential, poor stability of the air electrode, and poor recyclability. One of the critical factors affecting the rechargeability of zinc-air batteries is the formation of unstable growth morphologies during deposition, notably dendrites -- highly anisotropic and porous structures.[4] These dendrites are fragile and vulnerable to mechanical vibrations and can cause catastrophic failure by shorting the anode and cathode.

In the literature, the study of dendrite formation during Zn electrodeposition has focused on growth kinetics, additives, and impurities. The formation of ZnO was found to be a crucial factor affecting Zn morphology. In the electrochemical community, ZnO first attracted attention due to its contribution to interesting phenomena, such as oscillatory growth[5] and Hecker's effect[6], observed during electrodeposition. ZnO is known to the materials science and device physics communities as a semiconductor with a wide and direct band gap. ZnO is widely used in applications including but not limited to optoelectronic devices (e.g., light emitting diodes, lasers, etc.), sensors, and piezoelectric devices.[7] The potential for low-cost, large-scale production of ZnO with tunable morphologies has generated considerable interest in electrodeposition of ZnO.[8, 9]

The aims of my doctoral thesis are: to investigate the dendrite formation during Zn electrodeposition in aqueous solutions, to examine the growth behavior and morphological evolution of ZnO during electrodeposition of Zn, and to study the growth mechanisms of ZnO electrodeposition.

Chapter 2

2 Overview of Zn and ZnO electrodeposition

This chapter overviews the Zn and ZnO electrodeposition in two separate sections. These two sections introduce the theory, growth morphologies, and unique growth behaviors that have been reported in literature. At the end of this chapter, a scope of my dissertation work is presented.

2.1 Zn electrodeposition

This section starts with a background of electrochemistry associated with Zn electrodeposition and a discussion of dendrite formation. The section continues with an overview of morphological studies based on quasi two-dimensional (2D) cells. Finally, this section discusses the morphological transitions discovered within the 2D cell geometry such as oscillatory growth and the Hecker's effect.

2.1.1 Zn electrochemistry and dendrite formation

Zn is one of the most commonly used battery electrode materials because of its low equilibrium potential, high specific energy, high energy density, abundance, and low toxicity. Primary Zn batteries are widely used in the applications, where moderate specific energy and low manufacturing cost are main considerations. However, Zn electrodes have found limited use as secondary (rechargeable) batteries due to their poor cyclability and unpredictable life time. State-of-the-art Zn rechargeable batteries operate only up to 1000 charge-discharge cycles[10]. This problem of rechargeability has been attributed to the redistribution of Zn active material, and more importantly, the formation of detrimental growth instabilities during charging cycle. These highly directional and anisotropic growth instabilities, also known as dendrites, can grow outward and short circuit the battery cell.

Dendrites are multi-branching tree-like structures that develop during crystal growth at far-from-equilibrium conditions. (A classic example of far-from-equilibrium growth is the formation of dendritic crystals during rapid solidification of an undercooled melt.) The shapes of crystals grown at near equilibrium conditions is mainly governed by the crystal surface free energies and can be determined using the Wulff construction. Typically, the equilibrium crystal shapes are simple and compact with well-developed facets that minimize the total surface energy of the crystal. As the system is driven farther from equilibrium, surface and bulk mass transport kinetics play a major role in determining crystal shapes. These kinetic processes often result in complicated growth structures such as dendrites, which are energetically not necessarily the most stable geometries. The dendritic growth at far-from-equilibrium conditions has been a subject of great interest for the past several decades with many theories describing the formation of fractals and diffusion limited aggregates (DLA).[11-13]

During electrodeposition of Zn, growth instabilities occur, and dendrites form, when the growth rate is limited by the Zn(II) mass transport rate.[14-16] As the growth rate increases, minor fluctuations in the growth front lead to steeper concentration gradients and the deposition at the interface becomes more anisotropic resulting in the formation of dendritic structures. The charging current density, which is directly related to the growth rate, plays a crucial role in the formation of these detrimental morphologies. The higher the current density, the more likely dendritic morphologies will form. Furthermore, Zn is a hexagonal closed packed (HCP) crystal, where the c axis serves as the main axis for rotational symmetry, and gives rise to its inherent anisotropy. The anisotropic nature of Zn has been reported as one of the major contributions in forming dendritic structures[17], because growth occurs preferentially along $\langle 10\bar{1}0 \rangle$[18], which is the direction of prismatic planes and normal to the basal {0002} planes (see Fig. 2.1).

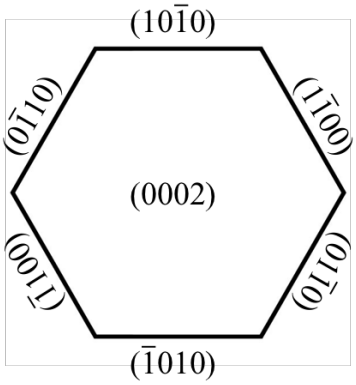

Figure 2.1, Schematic of Zn hexagonal close packed (HCP) crystal structure. Basal plane (0002) is aligned with the plane of the paper. The arrows indicate the prismatic planes.

2.1.2 Thin-layer electrochemical cell

Thin-layer cells have been extensively employed in studying electrodeposition pattern formation during electrodeposition, since they allow direct visualization of individual dendrite branches and eliminated the influence of gravity.[20-23] A thin-layer cell is typically a few hundred micrometers in thickness and consists of two electrodes and a thin layer of electrolyte solution. Cells with thickness below 300 μm are considered as quasi two-dimensional cell, because gravity and convection have negligible effect. Most studies use either a linear cell, where the cathode is parallel to anode, or a radial cell, also known as a Hele-Shaw cell, where cathode is concentric with anode.

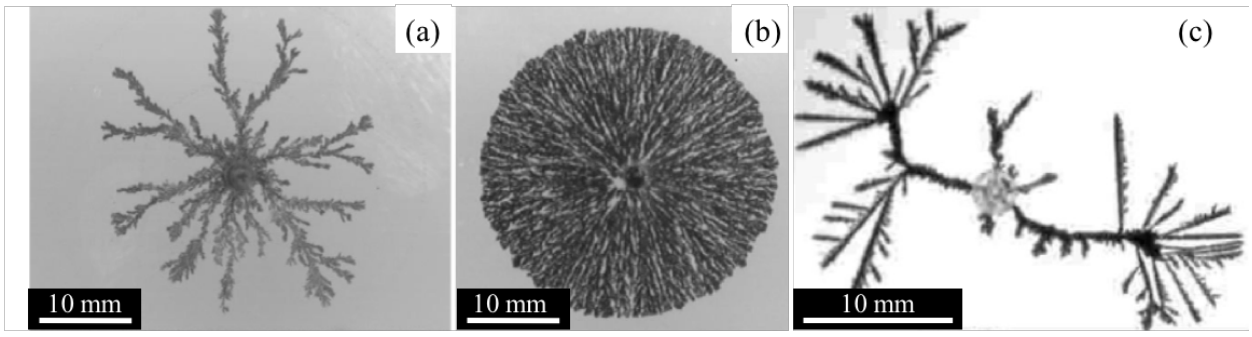

Figure 2.2, Optical micrographs showing typical morphologies of (a) diffusion limited aggregate (DLA), (b) dense branched, and (c) dendritic structures of Zn electrodeposited in Hele-Shaw cells.[19]

One of the main applications of a thin-layer cell is to understand the morphological variations associated with pattern formation. Morphologies described as DLA type, dense-branching, and fractal structures have been observed under various conditions (Fig. 2.2)[19]. A morphological diagram was reported based on a survey of potential and ion concentration.[24-26] A thin-layer geometry also facilitated studies of measuring concentration fields based on laser interferometry and optical absorption.[27] In addition, the quasi two-dimensionality of thin film geometries is amenable to numeric and analytic solutions[28] for the spatial distribution of ion concentrations. These calculations are useful in predicting the onset and the rate of growth. Experimentally, the roles of electrical and diffusion fields are also determined by altering anode geometry.[29] Modified versions of such quasi-2D cells were also to study the effects of temperature[30], solution viscosity[31], and even with applied magnetic field[32, 33] on electrodeposition process.

2.1.3 Hecker's effect and oscillatory growth

During the morphological studies of zinc electrodeposition in a thin-layer cell geometry, Hecker *et al.*[6] observed rapid and dramatic morphological transitions that occurred under various experimental conditions.[34] The Hecker's effect was originally used to describe a sudden change in color, roughness, and number of deposited branches at a certain distance from cathode to anode. In electrodeposition, the morphological transition associated with the Hecker's effect has been shown to result from either impurities (dissolving anodic metal ions) or a change in solution pH that alters metal growth.

Oscillation or alternating morphological transition is another interesting finding that can occur during electrodeposition. The phenomenon of oscillatory growth in electrodeposition was first reported during electrodeposition of Zn within a thin-layer cell geometry.[35, 36] As the dendrite

grew, the current (voltage) and the dendrite growth rate exhibited periodic oscillations at a constant applied voltage (current). Similar oscillatory behavior has also been observed during electrodeposition of other metals such as Sn[37], Cu, and Pb[38] and is often accompanied with ordered microstructures or even nanostructures[39].

The mechanisms leading to oscillatory behavior are not well understood. One of the original theories related this oscillatory behavior to side-branching nature of the dendrites.[35] Fleury[5] suggested that oscillatory growth arose from the combination of repetitive nucleation and a subsequent recovery phase needed for reconstructing local electrical field. Kuhn and Argoul[40] addressed the Zn oscillatory growth with interfacial chemical variations resulting from H+ reduction. Fukami *et al*.[41, 42] suggested that alternating and self-catalytic growth processes caused the oscillatory behavior. Ming's group observed that a periodic change in the concentration field in front of the dendrite tip played an important role.[43, 44] They also postulated that a thin-layer of ZnO electrodeposited alternatingly with Zn due to the reduction of dissolved oxygen.[45, 46] A similar mechanism was postulated in the study of oscillations during Cu/Cu_2O electrodeposition and its layered nanostructure.[39, 47]

2.2 ZnO electrodeposition

The first part of this section overviews the theory of ZnO electrodeposition and discusses what has been reported in previous studies involving various aqueous electrolytes. Later part of this section presents potential benefits of using electrodeposited ZnO for device applications. The last part of this section overviews the current techniques used to study ZnO electrodeposition in literature.

2.2.1 Overview of ZnO electrodeposition

ZnO is a direct wide band gap (3.37 eV) semiconductor, which has gained substantial interest during the past decade,[7] due to its potential use in electronics and optoelectronics among other applications.[9] The piezoelectric property of ZnO also makes it promising for applications such as sensors and energy generators. Nanostructures and thin films of ZnO were extensively studied for their controllable enhancement of electroluminescence, sensing, photocatalytic, and photovoltaic characterizations.[8] Optically transparent ZnO thin films are also attractive for transparent display technologies.

Many methods have been developed to synthesize ZnO with various grain sizes and morphologies, including chemical vapor deposition[48, 49] and a variety of vacuum based deposition methods[50, 51], hydrothermal[52, 53], sol-gel[54], and electrodeposition processes[55]. Among all of these methods, electrodeposition of ZnO is considered to be a low-cost process that is uniquely suited for thin film preparation and morphological control.[56-58] Existing literature indicates that the electrodeposition of ZnO from solution requires precursors, such as dissolved oxygen, nitrate ions, or hydrogen peroxide. Therefore, most of the ZnO electrodeposition experiments have been carried out in $Zn(NO_3)_2$ or $ZnCl_2$ electrolyte solutions. The role of additives or buffer solutions, such as, KCl[59], hexamethylenetetramine (HMT)[60], and ethylenediamine (EDA)[61] on the development of ZnO nanostructures has also been investigated.

2.2.2 Mechanistic study of ZnO electrodeposition

A widely accepted reaction pathway for ZnO electrodeposition involves the reduction of oxygen to hydroxyl ions, followed by chemical precipitation using the following reactions[62]

$$O_2 + 2H_2O + 4e^- \rightarrow 4OH^- \qquad [2.1]$$

$$Zn^{2+} + 2OH^- \rightarrow Zn(OH)_2 \rightarrow ZnO + 2H_2O \qquad [2.2]$$

The overall reaction is

$$Zn^{2+} + 0.5O_2 + 2e^- \rightarrow ZnO \quad [2.3]$$

However, the mechanistic understanding of ZnO formation remains unclear due to the complexity of chemical reactions in aqueous systems. For example, discrepancies exist on the discussion about the formation of intermediate phase $Zn(OH)_2$.[63] Systematic studies are necessary to understand the growth process the results of which can help develop methods for precise control of the morphologies and nanostructures for desired applications.

2.3 Scope of dissertation

The aim of my doctoral thesis is to develop mechanistic understanding of the electrodeposition kinetics of Zn and ZnO. To achieve this goal, I carried out a suite of *in situ* experiments and followed the electrodeposition of Zn and ZnO at length scales ranging from nanometers up to centimeters. *In situ* techniques offer many advantages over *ex situ* characterization tools for understanding the electrodeposition of Zn and ZnO. *In situ* characterization can not only enable direct observation of the growth and accurate measurements of growth kinetics, but also eliminate artefacts caused by *ex situ* characterization of air-exposed samples.

I used *in situ* optical microscopy and electrochemical atomic force microscopy (AFM) to directly observe the growth and to measure the growth kinetics. *In situ* electrochemical quartz crystal microbalance (EQCM) and wide-angle X-ray scattering (WAXS) techniques facilitated the mechanistic study by providing compositional and structural information. From all of these results, I developed a comprehensive model for Zn and ZnO morphological evolution.

Chapter 3 describes *in situ* optical microscopy studies of morphological evolution in electrochemical cells at millimeter and micrometer length scales. The following chapter (Chapter

4) focuses on the spontaneous oscillatory growth behavior during electrodeposition with the help of *in situ* optical microscopy. Next, Chapter 5 describes the role of pH on the dynamics of Zn electrodeposition by *in situ* AFM coupled with *in situ* EQCM. In Chapter 6, the prior *in situ* AFM investigation is extended to ZnO electrodeposition and its role on Zn electrodeposition morphology. This chapter also discusses the mechanism of ZnO electrodeposition. In the final chapter, summary and conclusions are presented followed by a discussion on future work (Chapter 7).

Chapter 3

3 *In situ* optical microscopy studies of dendrite formation during Zn electrodeposition in sulfate solution

Dendrite formation is one of the major obstacle in developing reliable rechargeable zinc-air battery. In electrodeposition, dendrite formation has attracted lots of attention because dendrites exhibit various morphologies and unique growth behaviors. Thin-layer liquid cell was used to study the growth morphologies and pattern formation during electrodeposition. This chapter focuses on the dendrite formation of electrodeposited Zn within the zinc sulfate ($ZnSO_4$) system and sets the foundation for my study on the Zn and ZnO electrodeposition in the following chapters. The first part of this chapter overviews the methods and experimental procedure. Section 3.2 includes the results from dendrite growth experiments. This section also discusses the influence of zinc salt concentration and applied voltage on the resulting dendrites.

3.1 Methods

This section starts with an introduction to the Hele-Shaw cell followed by an overview of the electrochemical techniques including chronoamperometry and ends with a description of the experimental procedure and characterization tools.

3.1.1 Electrochemical Hele-Shaw cell

The Hele-Shaw cell is a device that originated from investigations of growth instabilities, also known as viscous fingering, in fluids. This geometry is composed of a thin layer of liquid sandwiched between two parallel plates. The Hele-Shaw cell was widely used to simulate 2D flow in porous media. In the studies of electrodeposition, Matsushita *et al*.[20] first reported utilizing this geometry and demonstrated that the Hele-Shaw cell has several advantages in studying morphological evolution during electrodeposition. The first advantage is that in a thin layer of

electrolyte, the growth of the electrodeposit can be considered to be two-dimensional. Second advantage is that, within this thin cell, concentration gradients can be measured using laser interferometry or optical absorption[27, 31]; the knowledge of concentration gradients helps establish relationship between the growth behavior and Zn^{2+} concentration.

3.1.2 Electrochemical setup during electrodeposition

Two-electrode and three-electrode cell

An electrochemical cell is defined most generally as two electrodes separated by one or more electrolyte phases. In most cases, study focuses on only one of these electrodes, and it is known as the working electrode (WE). The other electrode is called counter electrode (CE), which is used to close the current circuit. The reference electrode (RE), which has a stable composition and fixed potential, provides a standardized potential for the potential control and measurement. Two-electrode and three-electrode configurations are two commonly used electrochemical cell setups. A two-electrode cell is built when the CE and RE are shorted. The three-electrode cell setup is the most common electrochemical cell setup in electrochemistry. In this case, the RE is placed in close proximity to the WE and used to measure the potential difference between the WE and the RE. In this chapter, the Hele-Shaw cell is built as a two-electrode cell, where the WE and RE/CE were reconfigured as the center and circular electrodes, respectively. In Chapters 5 and 6, applications of three-electrode geometry will be described in detail.

Chronoamperometry

Chronoamperometry is an electrochemical method, where the current response is measured versus time when the applied potential is maintained at a constant value or stepped from one constant value to another. In this chapter, all of the electrodepositions are carried out under constant applied potential and the current response is monitored as a function of time.

3.1.3 Instrumentation and procedure

All the *in situ* optical microscopy experiments are carried out using home-built electrochemical Hele-Shaw cells, schematically shown in Fig. 3.1 below.

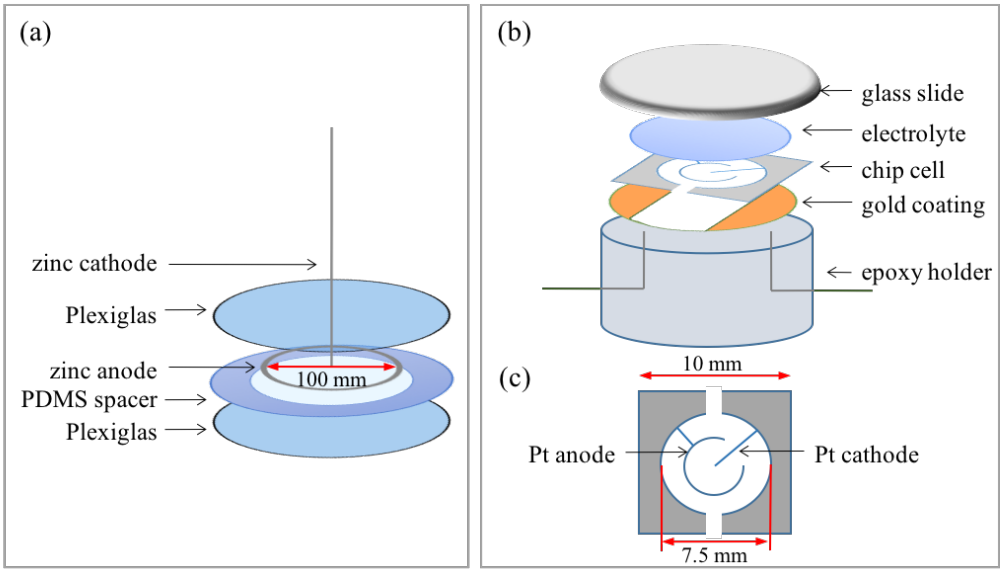

Figure 3.1, Schematics of electrochemical Hele-Shaw cells custom-designed for *in situ* optical microscopy observations at (a) millimeter and (b) micrometer length scales. (c) Pt electrode designed for micrometer length scale optical experiments. Similar designs were also used in *in situ* atomic force microscopy (AFM) experiments.

The larger cell [Fig. 3.1(a)] consists of a circular electrode (100 mm in diameter, CE/RE, anode) made from Zn wire (99.994% purity) sandwiched between two Plexiglas plates, separated by a 200-μm-thick polydimethylsiloxane (PDMS) spacer. A vertical Zn electrode (1 mm in diameter) is placed at the center of the cell through a 2-mm-diameter hole in the upper plate and served as the WE (cathode). Electrolyte is introduced carefully through the hole in order to prevent bubble formation in the thin layer of electrolyte. To ensure quasi-2D growth and under conditions similar to those used during *in situ* AFM experiments, a small-scale Hele-Shaw cell [Figs. 3.1(b) and (c)] with ultra-thin electrolyte film is also used to inspect the growth process. In this design, Pt thin films sputter-deposited and patterned on a 0.5-mm-thick glass substrate served as electrodes. The Pt pattern consisted of two parts: a circular pattern [left half in Fig. 3.1(c)], which was pre-

coated with zinc and served as CE/RE (anode); and a line pattern connected to the right half, which served as the WE (cathode). Pt layers are also deposited on the back-side and on all edges of the glass substrate to allow electrical contact from the back. In addition, the surface of the epoxy holder in contact with the glass is coated with a gold thin film. By placing a transparent glass slide on top, ~10-μm-thick liquid film can be confined within the cell because of capillary forces.

In situ optical experiments are conducted by placing the Hele-Shaw cell under an optical microscope (Leica M80). Images are acquired every 3 s. The images are digitally processed and morphological evolution data extracted using ImageJ, an image processing software. Electrochemical experiments are conducted using a Bio-Logic SP-200 potentiostat. For all experiments, the electrodeposition conditions are the same: the potential applied to the WE is -3 V with respect to the CE/RE. The $ZnSO_4$ electrolyte is prepared using distilled water and anhydrous $ZnSO_4$ powder (Aldrich). The solution concentration varied from 0.01 M to 1 M.

Morphologies of the electrodeposits are determined *ex situ* using a FEI Nova Nano 230 scanning electron microscope (SEM). In order to preserve the structure, the electrodeposited samples are carefully collected from the solution and then rinsed using deionized (DI) water.

3.2 Data analysis and discussion

Zinc sulfate solution is used as the electrolyte for Zn electrodeposition. At the cathode, Zn(II) ions are oxidized and are deposited on the electrode through the following reaction:

$$Zn^{2+} + 2e^- \longrightarrow Zn,\ E = -0.76\ V\ vs.\ NHE \qquad [3.1]$$

At the anode, Zn(0) wire is reduced and dissolved into electrolyte as Zn(II) ions by the reaction:

$$Zn - 2e^- \longrightarrow Zn^{2+} \qquad [3.2]$$

In an electrochemical Hele-Shaw geometry, the Zn electrodeposits are observed to form on the center cathode with various morphologies as a function of concentration. In Chapter 4, oscillatory growth behavior during the electrodeposition is discussed.

3.2.1 Morphological evolution

In situ optical microscopy movies (e.g., Movie 3.1) acquired during electrodeposition of Zn using 0.01 M $ZnSO_4$ solution in the large Hele-Shaw cell show the growth of dendrites from the center electrode. Fig. 3.2(a) is an individual frame extracted from the movie 3.1.

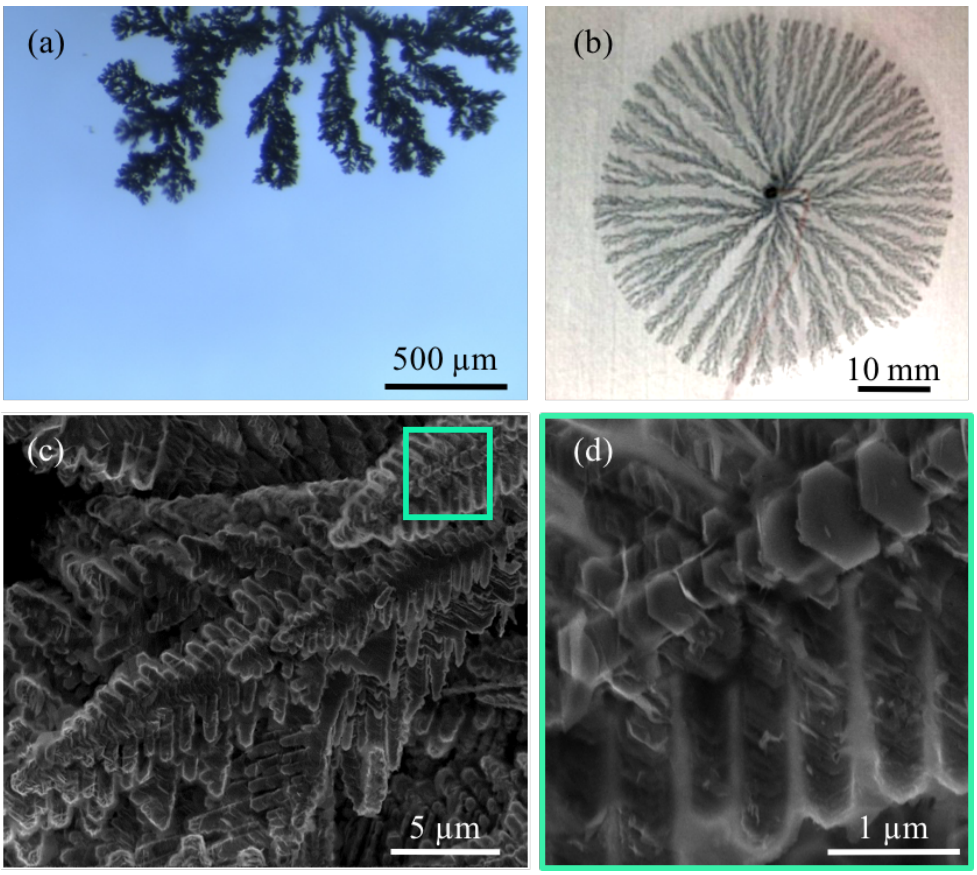

Figure 3.2, Morphologies of Zn dendrites electrodeposited from 0.01 M $ZnSO_4$ solution. (a) *In situ* optical microscopy image of a portion of the growth front extracted from Movie 3.1 acquired *in situ* during electrodeposition. (b) Photograph of the entire electrodeposit obtained *ex situ* after the deposition. (c) Scanning electron microscopy (SEM) image of the dendrites. (d) Higher magnification SEM image of a dendrite highlighted by a green box in (c).

As observed in the movie, the dendrite morphologies are qualitatively similar to the DLA-type growth structures. The individual dendrites are flexible and porous. As the branches grow and spread out, they interact with each other. The overall shape of the deposit is circular [Fig. 3.2(b)], as expected for the growth in a Hele-Shaw geometry with radially symmetric diffusion and electrical fields. Microscopic morphology of these dendrites is investigated through *ex situ* SEM imaging [Figs. 3.2(c) and (d)]. The porous branches are found to be highly faceted structures. Higher magnification SEM images revealed that the faceted branches are composed of platelets with hexagonal shape, consistent with the hexagonal crystal structure of Zn.

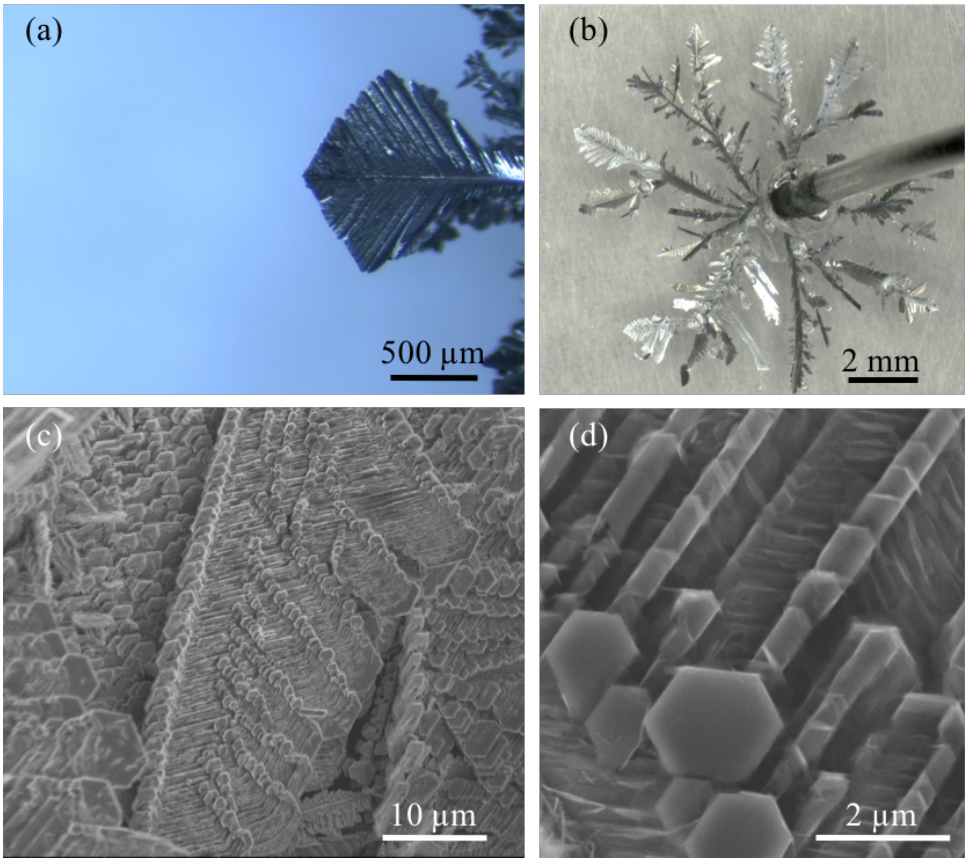

Figure 3.3, Growth morphologies of Zn structures electrodeposited from 0.1 M $ZnSO_4$ solution. (a) *In situ* optical microscopy image of growth structures, part of Movie 3.2, acquired during electrodeposition. (b) Photograph showing the overall shape of the electrodeposit obtained after the deposition. (c) SEM image obtained from one of the branches. (d) Higher magnification SEM image of Zn crystallites visible in (c).

In situ optical microscopy movie (e.g. Movie 3.2) of Zn electrodeposition using 0.1 M $ZnSO_4$ solution in the larger Hele-Shaw cell shows the growth of more compact and leaf-like structures [Fig. 3.3(a)], different from the Zn dendrites formed in 0.01 M $ZnSO_4$ solution. Edges of each dendrite manifest six-fold symmetry with 120° angles. The overall macroscopic shape of the entire deposit is circular [Fig. 3.3(b)], similar to the dendrites in Fig. 3.2, due to the radially symmetric electrical and diffusional fields. However, the deposits composed of fewer but larger branches with several sub-branches, each of which is at 60° with respect to the parent branch. From the SEM image in Fig. 3.3(c), the midribs of these branches appear to be a superposition of multiple Zn crystallites, based upon which I speculate that the branch formation is a consequence of repeated nucleation along the growth direction. Fig. 3.3(d) is a typical higher magnification SEM image of an individual Zn crystallite. The observed hexagonal shape of the Zn crystallites can be attributed to the preferential lateral growth of basal {0001} planes bounded by $\{10\bar{1}0\}$ prism facets.

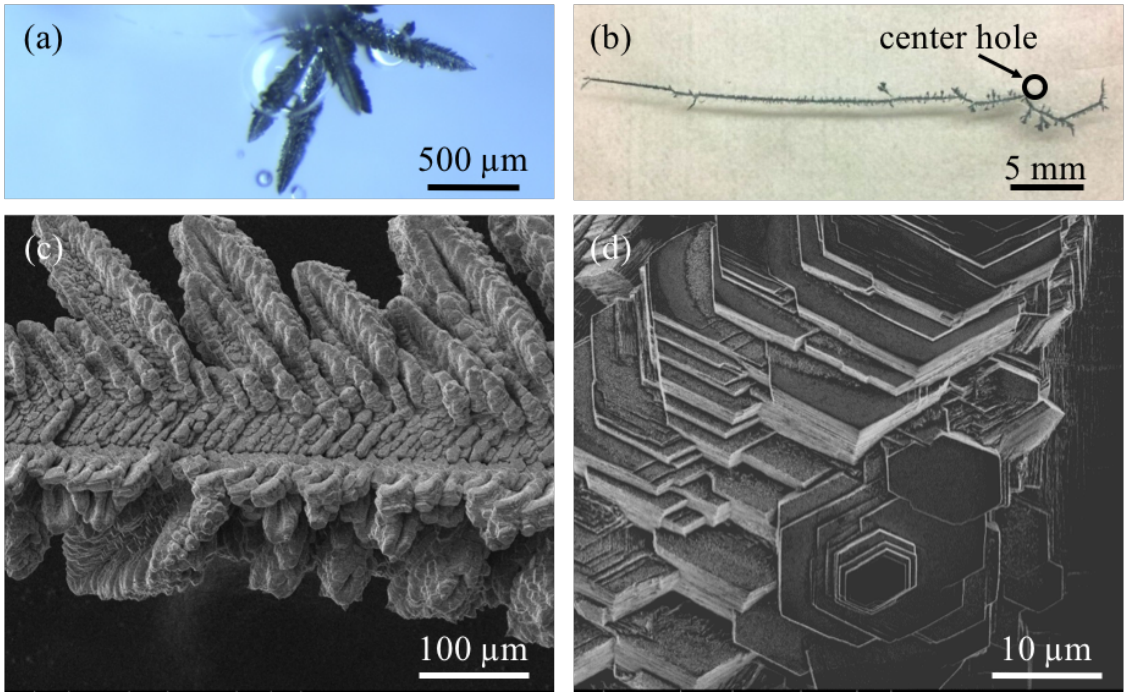

Figure 3.4, Growth morphologies of Zn dendrites electrodeposited from 1 M $ZnSO_4$ solution. (a) Optical micrograph acquired *in situ* during electrodeposition. The image is part of the

measurement sequence recorded as Movie 3.3. (b) Photograph of the entire dendrite obtained after electrodeposition. (c and d) Lower and higher magnification SEM images of the dendrite.

Figure 3.4(a) is an individual frame extracted from an *in situ* optical microscopy movie (e.g. Movie 3.3) acquired during electrodeposition of Zn using 1 M zinc sulfate solution. Within this field of view, I found four dendrites. Fig. 3.4(b) is a photograph taken after deposition, which shows the growth of only one dendrite. Figs. 3.4(c) and (d) are lower and higher magnification SEM images obtained from a portion of the dendrite. These images indicate that the Zn dendrite is made up of thick hexagonal platelets stacked along the basal planes on top of each other as shown in Fig. 3.4(d). These hexagonal platelets appear to be even more compact than those obtained from 0.1 M solution. Crystal anisotropy of Zn is well pronounced in this growth morphology.

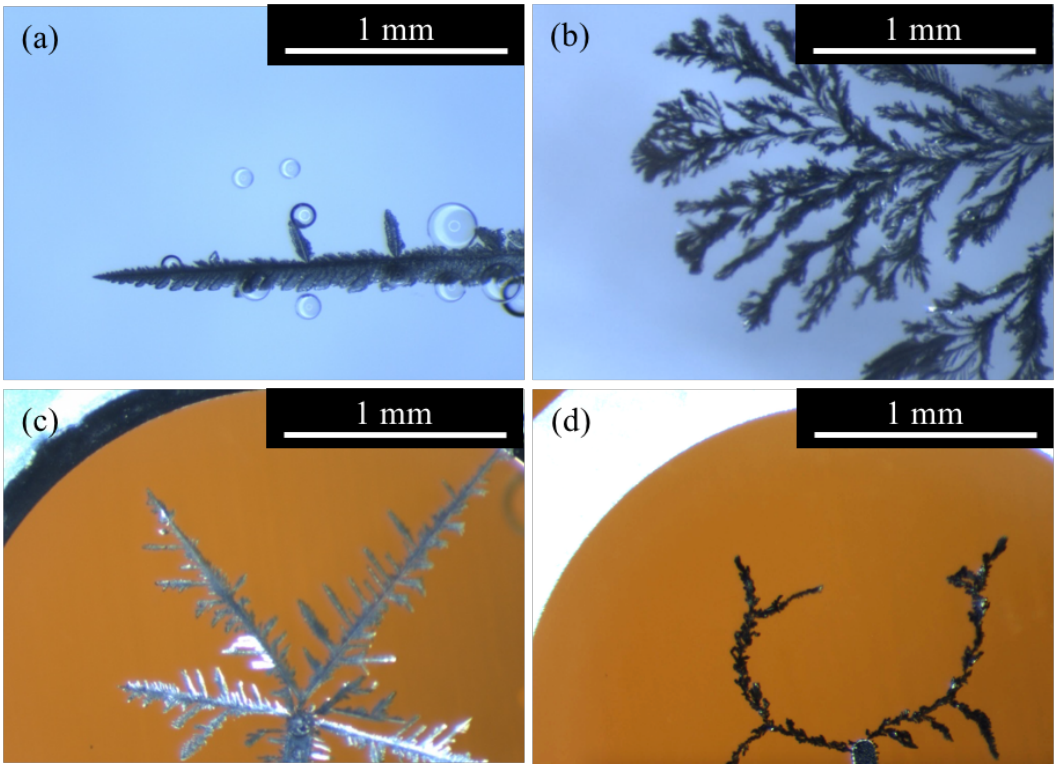

Figure 3.5, Comparison of morphologies of Zn structures electrodeposited in the large (millimeter-scale) and small (micrometer-scale) Hele-Shaw cells. *In situ* optical microscopy images of growth structures acquired during Zn electrodeposition in the large cell using (a) 1 M and (b) 0.01 M

$ZnSO_4$ solutions. (c) and (d) are optical photographs of the electrodeposits obtained *in situ* in the smaller cell with 1 M and 0.01 M $ZnSO_4$ solutions, respectively.

Figures 3.5(a)-(d) present a comparison of the morphologies of Zn structures electrodeposited from 1 M and 0.01 M $ZnSO_4$ solutions in large (millimeter-scale) and small (micrometer-scale) Hele-Shaw cells. Figs. 3.5(a) and (b) are optical micrographs acquired *in situ* during electrodeposition in millimeter-scale Hele-Shaw cells [Fig. 3.1(a)] from 1 M and 0.01 M $ZnSO_4$, respectively. Figs. 3.5(c) and (d) are optical micrographs showing the growth morphologies obtained after electrodeposition using 1 M and 0.01 M $ZnSO_4$, respectively in micrometer-scale cell [Fig. 3.1(b)]. In both the large and small cells, overall shapes of the electrodeposits are radially symmetric. In all the deposits, a primary trunk and side branches (orientated 60˚ with respect to the trunk) are observed. At higher electrolyte concentration, i.e. 1 M, the electrodeposition of Zn is highly anisotropic resulting in higher aspect ratio and more compact structures. The hexagonal crystal symmetry is evident in the structures. At lower concentration, i.e. 0.01 M, hexagonal crystal symmetry is no longer observed and the electrodeposited structure in Fig. 3.5(d) appears to be flimsy and porous.

3.2.2 Growth kinetics

In situ optical microscopy data facilitate accurate measurements of growth rates because the images of growth structures are acquired during electrodeposition as a function of time. Figs. 3.6(a)-(c) are series of outlines of the growth deposits measured from *in situ* optical microscopy images acquired during electrodeposition in (a) 0.01 M, (b) 0.1 M, and (c) 1 M $ZnSO_4$ solutions. For each set of data presented in Figs. 3.6(a)-(c), the shapes of the growth deposits are extracted from individual frames and overlaid to form the stacks of outlines as shown. From the time-dependent changes in projected areas of the deposited material, areal growth rates are determined. However, one should note that the projected area represented the lateral growth in 2D, and does

not account for the growth along the third dimension. The projected areas of the deposits obtained at the three different electrolyte concentrations are plotted as a function of time in Fig. 3.6(d). Electrodeposits in 0.01 M grew the fastest. The growth in 0.1 M was slower, and the growth in 1 M was found to be the slowest. Growth rates obtained by linear least-squares fits to the experimental data are 1.27×10^4, 0.67×10^4, and 0.18×10^4 $\mu m^2/s$ for 0.01 M, 0.1 M, and 1 M, respectively. In Fig. 3.6(e), the amount of material deposited (mmol), as calculated using the amount of charge transferred, dQ(C), is plotted as a function of time. In this plot, the fastest growth is obtained from 1 M solution followed by 0.1 M, with the slowest growth in 0.01 M solution.

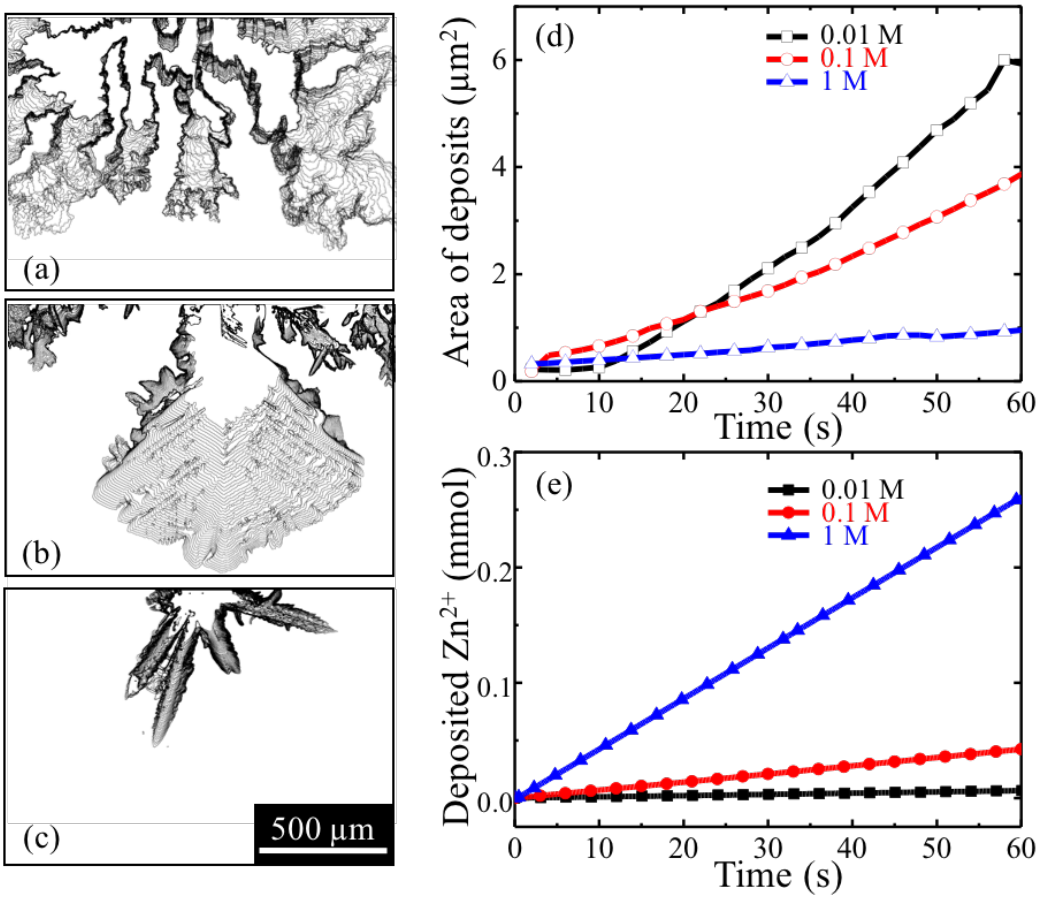

Figure 3.6, (a-c) Stacks of dendrite shape contours extracted using ImageJ software from *in situ* optical microscopy movies acquired as a function of time during electrodeposition. The electrolyte concentration and the number of images stacked in the panels (a-c) are: (a) 0.01 M, 33 frames, (b) 0.1 M, 46 frames, and (c) 1 M, 50 frames. (d) Plots of two-dimensional (2D) projected area of the deposits as a function of deposition time. (e) Plot showing the expected amounts of electrodeposited Zn, calculated using the amount of charge transferred, as a function of time.

3.2.3 Discussion

At low electrolyte concentration (0.01 M), I found that the electrodeposits resembled DLA-type structures, i.e. disordered fractals with no apparent symmetry. Since 1980s, DLA morphologies have been observed during electrodeposition of Cu and Zn under conditions promoting 2D growth and are expected when the depositing species (atoms, molecules, radicals, etc.) undergo random walk before attaching to an existing cluster in the vicinity.

At 0.1 M concentration, the electrodeposits exhibit pronounced crystal anisotropy, such as, straight edges, 60˚ splitting angles, and parallel secondary branches [Fig. 3.5(c)]. At higher concentration of 1 M, the electrodeposits are acicular with hexagonal shapes due to the HCP structure of Zn. Fig. 3.7 shows a morphological diagram developed by Grier *et al.*[24] based on the growth structures observed during Zn electrodeposition, where the terms DLA, transition region, and dendrites are used to describe the different fractal or needle-like morphologies. My results are consistent with their observations and fit well within the categories defined in their work.

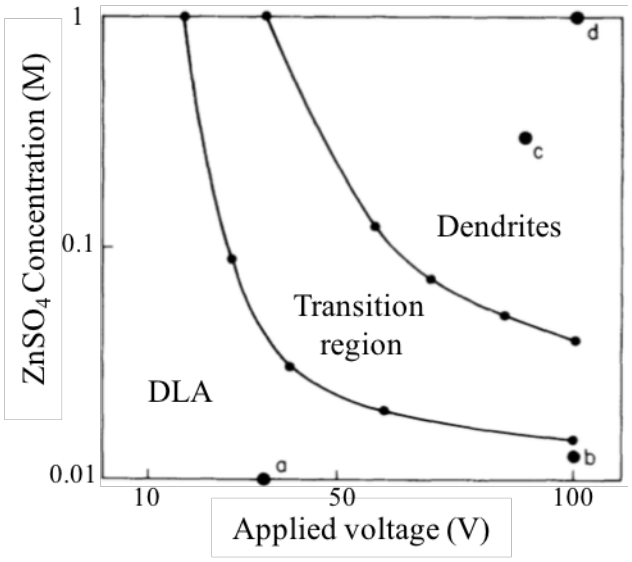

Figure 3.7, Morphology diagram by Grier *et al.*[24] for Zn electrodeposited from $ZnSO_4$ solution.

Based on my SEM images, I noticed that that crystal anisotropy plays a role in the nucleation and growth of both the dendrites and DLA-like patterns. The hexagonal shaped crystallites are observed to be the building blocks of porous DLA structure. In addition, these crystallites form an ordered structure instead of agglomerating randomly as predicted in DLA model. Therefore, throughout all concentrations, crystalline nature of Zn plays an important role in the formation of electrodeposition morphologies.

The experimentally measured variations in growth rates as a function of electrolyte concentration are opposite to the expected behavior. Theoretically, the growth rates of electrodeposits at higher concentration are expected to be higher than those obtained in lower concentrations. However, in my experiments, the growth at lowest concentration exhibited the highest rate. I attribute this discrepancy to the measurement procedure, where I measure the 2D projected areal growth rates and ignore the 3D nature of the electrodeposits. Even though my experimental design is based on the assumption that the growth is quasi-2D, my observations of the microstructure have demonstrated that variations in thicknesses cannot be neglected for quantitative description of the electrodeposition in different solution concentrations. In addition, side reactions, such as, hydrogen evolution, which tend to occur at higher concentration, could cause a lower deposition efficiency. As a result, the amount of Zn deposited, and hence the growth rate, at higher concentration are less than those theoretically expected based on the charge transferred.

3.3 Conclusions

In this chapter, I introduced different morphologies obtained during electrodeposition of Zn in electrochemical Hele-Shaw cells. At low Zn^{2+} concentration, the macroscopic growth morphology reflects the radially-symmetric diffusion and electrical fields. As the Zn^{2+} concentration increases, Zn crystal anisotropy manifested in macroscopic structures. Detailed investigation of the microstructures indicated that even at low electrolyte concentration, where DLA-type structures are observed, crystal anisotropy plays an important role during electrodeposition.

My *in situ* optical microscopy studies helped improve the understanding of electrodeposition of Zn in zinc sulfate solution. During the course of these investigations, I

discovered interesting phenomena such as Hecker's effect and oscillatory growth, described in Chapter 4.

Chapter 4

4 *In situ* optical microscopy studies of spontaneous oscillatory growth of Zn dendrites

4.1 Overview of oscillatory behavior in electrodeposition

In the study of growth morphology and pattern formation during electrodeposition, morphological transitions were observed in various experimental conditions. Oscillatory growth, an alternating morphological transition, was first discovered during the dendrite formation in Zn electrodeposition. The growth rate along with the current (voltage) exhibit spontaneous oscillations when a constant voltage (current) is applied. Spontaneous growth oscillations were also observed during the electrodeposition of Sn[37], Cu, and Pb[38] with ordered micro/nanostructures. Theories of the growth mechanism have been developed to relate the oscillatory behavior to variations in interfacial chemistry[40], nonlinear interfacial kinetics[43], crystal nucleation[5] and growth kinetics[35, 41, 42], and mass transport[43, 44].

In this chapter, I present the phenomenon of spontaneous oscillation as studied using *in situ* optical microscopy along with other *ex situ* characterization tools. The growth oscillations are monitored *in situ* and the optical microscopy images are used to quantify the behavior. The morphology and crystallinity of the electrodeposits are determined using SEM, cross-sectional transmission electron microscopy (XTEM), and x-ray diffraction (XRD) techniques. Based on the growth dynamics and structural information, a growth model is suggested.

4.2 Methods

4.2.1 Experimental procedure

Electrochemical deposition is carried out in a Hele-Shaw electrochemical cell [Fig. 3.1(a)]. All the results presented in this chapter are obtained using $ZnSO_4$ as the electrolyte and the most

commonly used concentration is 0.1 M adjusted to pH = 3.0. The pH values are adjusted by adding small amounts of either KOH or H_2SO_4 and are measured using an Accumet gel-filled pH electrode.

Electrodeposition is carried out at a constant potential, E, using a Bio-logic SP-200 potentiostat. In the Hele-Shaw geometry, the constant potential is applied on the center electrode (WE) with respect to the circular electrode (CE/RE). Current (I) response versus time (t) is measured with a time resolution of 0.05 s. The Ohmic drop across the cell is not compensated during these experiments. After growth, the electrochemically deposited Zn dendrites are extracted from the electrolyte and rinsed carefully in distilled water to remove the dissolved salts.

4.2.2 Digital image processing

In situ optical microscopy videos are acquired during electrodeposition at a rate of 28 frames/s using aVHX-1000 digital microscope (200X). Pixel resolution in the frames is 800 × 600 pixels. Image processing macros customized for ImageJ software are employed to batch-process the frames extracted from the videos and to determine the contours and projected areas of the deposits from the images.

4.2.3 Characterization techniques

Free-standing, air-dried, dendrite samples required for characterization are collected from the electrolyte since all of the electrodeposition experiments are carried out in a Hele-Shaw cell. Special care was taken during rinsing and drying to avoid damage to the fragile samples. The free-standing samples are then transferred onto a carbon tape for SEM imaging and for TEM sample preparation. Morphology, composition, and crystallinity of the dendrites are determined *ex situ* using a Nova Nano 230 SEM, a focused ion beam (FIB) Nova 600 Nanolab-DualBeam equipped with SEM, a 300 kV FEI Titan scanning TEM (S/TEM), and a Jordan Valley D1 x-ray diffractometer.

TEM sample preparation

XTEM samples are prepared using the FIB system. Prior to ion beam milling, the sample surface [Fig. 4.1(a)] is protected by sequential deposition of 0.5 μm and 1-μm thick layers of Pt from trimethyl platinum ($C_9H_{16}Pt$), a metalorganic precursor, using 5 kV, 6.3 nA electron beams and 30 kV, 0.3 nA ion beams, respectively. The XTEM sample is prepared by removing materials above and below the region of interest (ROI). First, trenches are milled on two sides of the ROI using 30 kV and 20 nA ion beams [Figs. 4.1(b) and (c)]. Then the sample is cut out, attached to a Kleindiek nanomanipulator needle using electron-beam-deposited Pt, and transferred onto a 4-post Cu grid, where the sample is secured using electron-beam-deposited carbon. The final thinning step is carried out carefully so as to minimize mechanical damage to the thin (<100 nm) sample [Fig. 4.1(d)]. The sample is then stored in a vacuum desiccator until TEM examination.

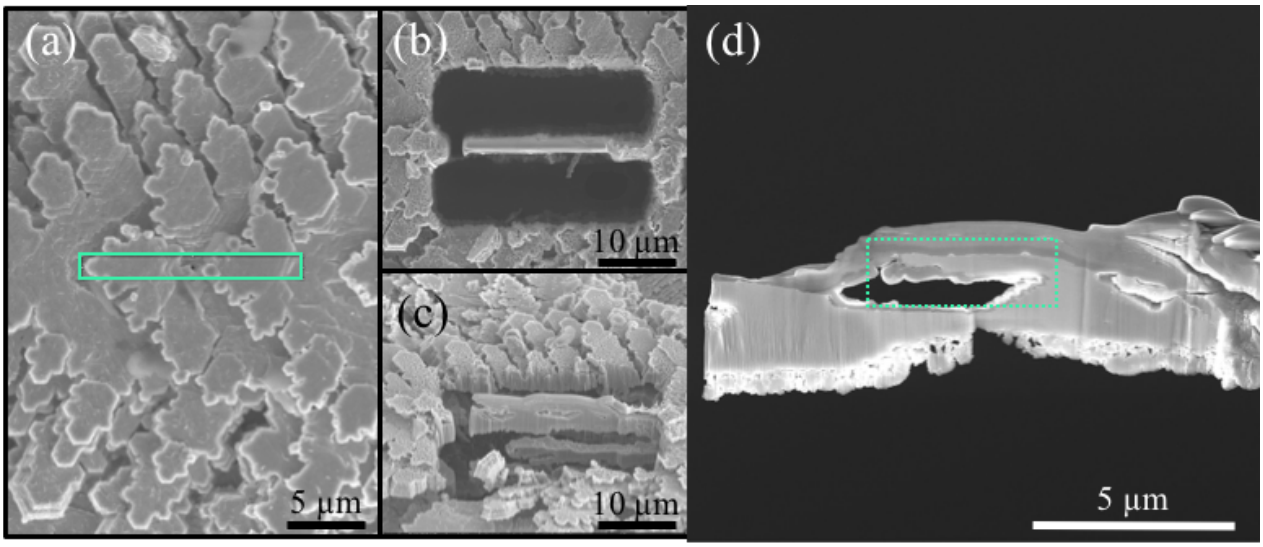

Figure 4.1, Representative SEM images acquired during a typical cross-sectional transmission electron microscopy (XTEM) sample preparation. (a) Top view of the original dendrite. A green box highlights the desired region of interest from which XTEM sample is extracted. (b) Top and (c) 52° tilted views of trenches created by focused ion beam (FIB) milling of the sample. (d) XTEM sample removed from the bulk and adhered to a TEM grid before thinning to the final electron transparency. The green dashed box shows the area of interest for TEM observation.

X-ray diffraction and pole figure measurements

X-ray diffraction (XRD) spectra are obtained using a Jordan Valley D1 diffractometer with copper $K\alpha_1$ radiation and a parallel beam source. The out-of-plane and in-plane orientations of the electrodeposits are determined using the Bragg (θ), rocking (ω), tilting (χ), and azimuthal rotation (φ) angles. The incident beam aperture is a 1 mm diameter hole. Electrodeposited dendrite samples (~1 mm in width and 2-4 mm in length) are attached to a Si(001) wafer using amorphous carbon tape. First, the x-ray source and detector (θ)are aligned to achieve maximum intensity. Then, ω and φ are calibrated with respect to the Si(004) peak. The sample is aligned visually with the help of a laser pointer. Rocking curves (ω scans) are obtained around Zn(0002) peak, $2\theta = 36.32^{o}$. 2θ-ω data are acquired with a step size of 0.05° from 2θ = 20° to 100°.

In Chapter 5, I present X-ray pole figure measurements used to examine crystallinity of the electrodeposited Zn film on single-crystalline Cu(111) substrate. Pole figure measurements are performed using the same diffractometer. The incident aperture size is 4 mm in diameter and Soller slits are used as the receiving slits with an acceptance angle of ~1°. The sample is mounted vertically on a Si(001) wafer to eliminate any background signal from the diffractometer stage. Pole figure data are collected at a given diffraction angle 2θ by varying tilt angle χ (measured with respect to the sample surface normal) from 0° to 90° with a step size of 2° and azimuthal rotation angle φ (measured around sample surface normal) from 0° to 360° with a step size of 1°. The dwell time at each data point was 0.5 s. Pole figures are plotted with the obtained diffracted intensity data as a function of χ and φ.

4.3 Data analysis and discussion

4.3.1 Oscillatory behavior

I discovered oscillatory growth behavior during my study of electrodeposited Zn morphologies as a function of pH. I observed leaf-like growth morphologies consistently in all the electrodeposited samples from 0.1 M $ZnSO_4$ solutions with pH values between 3 and 4.3. Through a series of electrodeposition experiments carried out while systematically varying the parameters (electrolyte concentrations from 0.01 M to 1 M, pH from 3 to 4.3 in 0.1 increments, and applied voltage from –0.5 V to 3.5 V), I found that stable and sustained periodic oscillations occur at pH = 3 ± 0.1, 0.1 ± 0.025 M $ZnSO_4$ solution with applied potential at –2 ± 0.1 V.

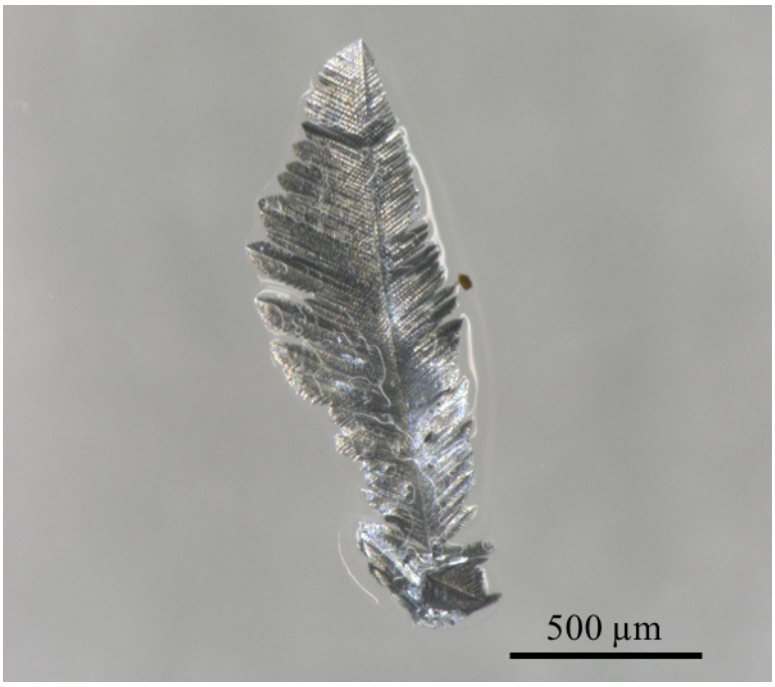

Figure 4.2, Optical micrograph of an electrodeposited Zn leaf acquired during oscillatory growth from 0.1 M $ZnSO_4$ (pH = 3.0) at a constant applied potential E = -2.0 V.

Movie 4.1 is a typical *in situ* optical microscopy video showing the oscillatory growth of dendrites during electrodeposition of Zn at a fixed potential of -2 V from 0.1 M $ZnSO_4$ solution with pH = 3. In this measurement sequence, the tips of the dendrites grew alternatingly at faster and slower rates and the growth rates varied periodically with time. Although the *in situ* movie

focused on one of the many branches, the oscillatory growth is a global phenomenon and will be discussed later in section 4.3.1. Fig. 4.2 shows an optical microscopy image of a dendrite, grown under the same conditions as in Movie 4.1, taken after it was removed from the solution. The shape and dimension observed under optical microscope are similar compared to other dendrites that grew without oscillatory condition (Fig. 3.3). Detailed morphological studies will be discussed later in this chapter.

4.3.2 Growth rate analysis

In this section, I present quantitative analysis of oscillatory growth phenomenon. Contours and 2D projected areas of the dendrites observed *in situ* are extracted from the optical microscopy image sequences and analyzed. Figs. 4.3(a) and (b) are 2D and 3D plots, respectively illustrating the shape evolution as a function of time. Note that the midrib of the leaf grows in the direction aligned with electrical field. The side branches are oriented at a 60^{o} angle to the midrib.

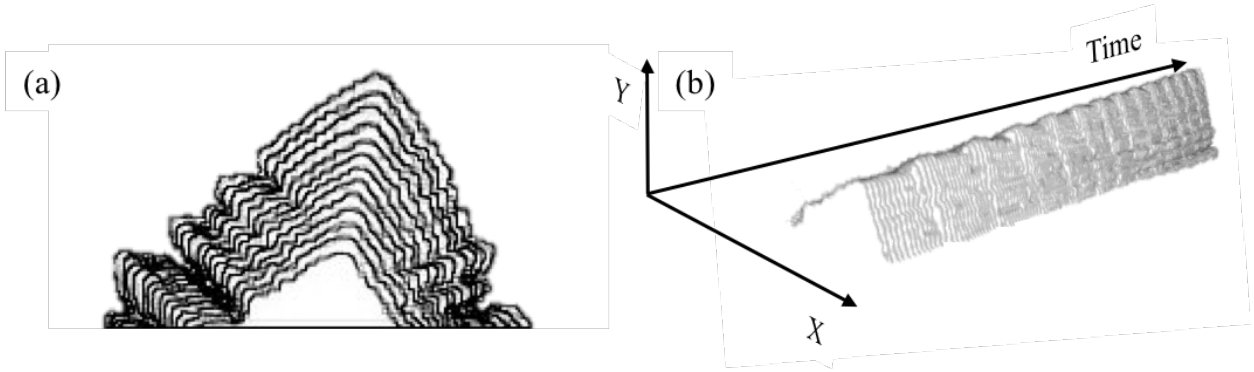

Figure 4.3, Evolution of the growth front during potentiostatic electrodeposition of Zn in $ZnSO_4$ solution. (a) Representative stack of contours of a typical dendrite extracted from an *in situ* optical microscopy video (Movie 4.1). (b) 3D plot of the same dendrite showing its 2D projected shape on x-y plane as a function of time (z axis). This data was generated from 380 image frames, part of Movie 4.1, captured at a rate of 28 frames/s.

In Fig. 4.3(a), I observed the development of protrusions into independent side branches. In both the plots, the white space between any two contours corresponds to the time period during which the dendrite growth was minimal. As shown in Fig. 4.3(b), within each rapid-slow growth cycle, the contour of the dendrite remained stationary for about 10 frames and then a sudden growth spurt was observed within 2 or 3 frames. The nearly even spacing between any two successive contours indicated that the rapid-slow growth cycle is periodic in time, at least during the early stages of growth.

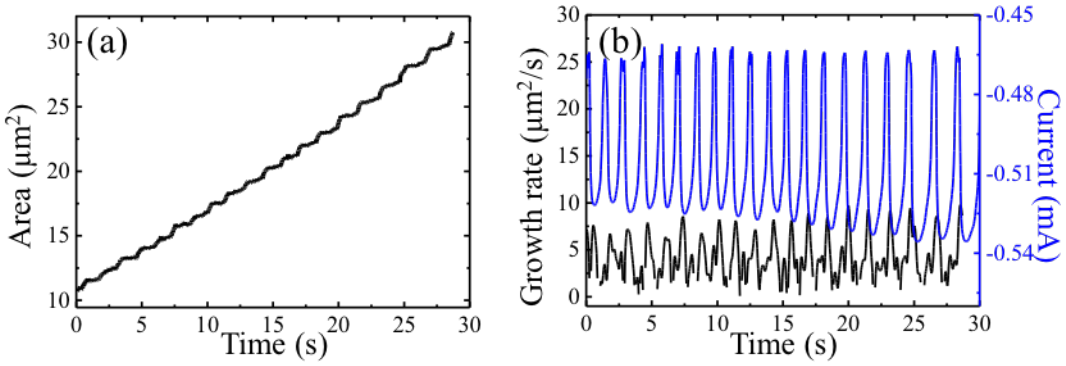

Figure 4.4, Plots of (a) 2D projected areas of the dendrite, and (b) normalized velocity (black curve) of the dendrite tip, and measured current response (blue curve) as a function of the deposition time.

Figure 4.4(a) is a plot of the change in 2D area of the electrodeposits as a function of deposition time. A step-wise increase in area with time is observed. Fig. 4.4(b) shows plots of the normalized growth velocity and current as a function of time. (In these experiments, the applied potential is maintained constant at -2.0 V with respect to CE during the growth.) I found that both the growth rate and the current oscillated periodically. The frequency and phase of current oscillation are in sync with oscillatory areal growth; the current increased in magnitude as the deposited area increased rapidly and the current was at its minimum when the area grew slowly. I also found that the average frequencies of both areal growth rate and current oscillations are equal and increased from ~0.59 s^{-1} to 0.91 s^{-1} with increasing applied potential from 2.0 V to 2.5 V.

4.3.3 Layered morphology analysis

Scanning electron microscopy (SEM)

Figures 4.5(a)-(d) are *ex situ* SEM images of the leaf-like Zn dendrites electrodeposited under conditions, where the growth oscillations are observed. The dendrites appear similar to those seen in optical micrographs, with a periodic microstructure composed of parallel flakes with similar lengths growing out of main trunk [Fig. 4.5(b)]. A higher magnification image and the inset in Fig. 4.5(c) show the orientation of the flake with respect to the trunk. I speculate that the flake grew outward at an angle with respect to the trunk. I have also observed that main trunk is faceted and composed of hexagonal crystallites that are a few hundreds of nanometers in size. SEM image [Fig. 4.5(d)] obtained from cross-sectional samples prepared by FIB confirmed the layered structure. The image also demonstrated that the trunk extends across the field of view, suggestive of continuous growth without any interruptions, while the flakes are discontinuous and grow at an inclination to the trunk.

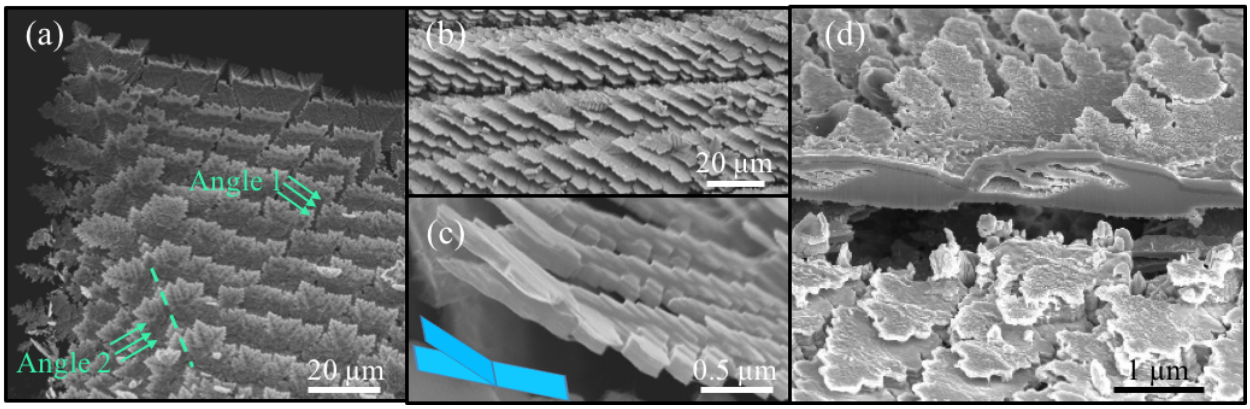

Figure 4.5, SEM images of leaf-like Zn dendrites electrodeposited under conditions, where oscillatory behavior was observed. (a) Top view of a typical dendrite tip, the growth front. (b) The growth front as viewed along angle labeled 1 in (a). This particular SEM image was acquired with the sample tilted to 52°. (c) Higher magnification image of the tip in (b). Inset is a schematic showing the off-axis growth at the tip. (d) Cross-sectional view, as seen along angle 2 in (a), of the midrib of the dendrite highlighted by a dotted line in (a).

Transmission electron microscopy (TEM)

Figure 4.6(a) is a bright-field TEM image of a portion of the Zn dendrite sample in Figs. 4.2 and 4.5. Dashed green lines depict the boundaries between darker and lighter grey contrast regions in the image, which correspond to thicker and thinner sections of the dendrite, respectively.

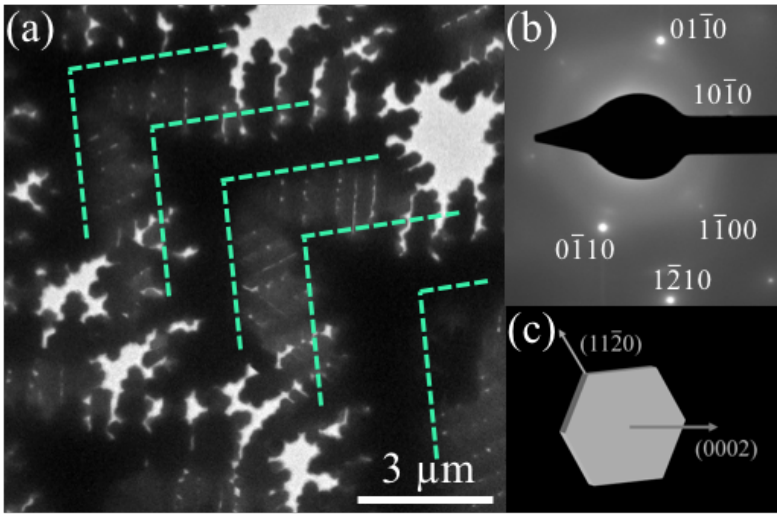

Figure 4.6, TEM characterization of the Zn dendrite structure shown in Fig. 3. (a) Representative bright-field TEM image of a Zn dendrite. The dashed green lines highlight periodically alternating darker and lighter grey contrast, corresponding to thicker and thinner regions respectively, within the dendrite. (b) Selected area electron diffraction (SAED) pattern acquired from one of the thin regions. The diffraction spots are identified as hexagonal close-packed structure. (c) A schematic of Zn hexagonal crystallite. Basal {0001} and prismatic $\{10\bar{1}0\}$ planes are labeled as shown.

Given that the TEM image is acquired from one of the dendrite tips, i.e. the growth front, the nearly equal spacing between the dashed lines along the tip suggests that these thickness variations occur periodically during electrodeposition. Selected area electron diffraction (SAED) pattern obtained from one of the thinner regions indicated that the dendrite is a {0001}-oriented single-crystal with [0001] normal to the plane of the paper. As demonstrated from previous SEM images, the dendrites are made of hexagonal Zn crystallites, stacked in the same orientation as illustrated in Fig. 4.6(c). From the TEM image [Fig. 4.6(a)] and the SAED pattern, I determined the tip direction as $[11\bar{2}0]$. In the SAED pattern, I observed additional diffuse arc-shaped reflections radially along the $\{10\bar{1}0\}$ spots but closer to the central reflection. I attribute these additional spots to the presence of ZnO. The formation of ZnO is unavoidable and could occur

during electrodeposition due to the presence of dissolved oxygen in the electrolyte and/or upon air-exposure prior to TEM characterization. The arc-shaped reflections are indicative of texture (preferred orientation) rather than epitaxial growth of the oxide. As shown in Fig. 4.6(a), the dendrites are generally too thick for TEM imaging. In order to accurately determine the crystal orientation relationships within the dendrite, I utilized FIB and milled out a single repeating unit of the periodic structure. SEM image in Fig. 4.7 shows the FIB sample containing an out-of-plane flake and the supporting continuous main trunk. SAED patterns of the flake (area labeled A in the SEM image) and the trunk (area labeled B) showed that they are both single-crystals and with the same zone axis $\langle 01\bar{1}0 \rangle$. However, the two patterns are rotated by ~19° with respect to each other indicating that the out-of-plane flake is oriented at ~19° to the basal plane. SAED pattern acquired from the area C containing both the flake and trunk is a superposition of the two patterns. Streaks visible in the pattern are likely due to mechanical deformation of the dendrite during the preparation of TEM sample via FIB milling.

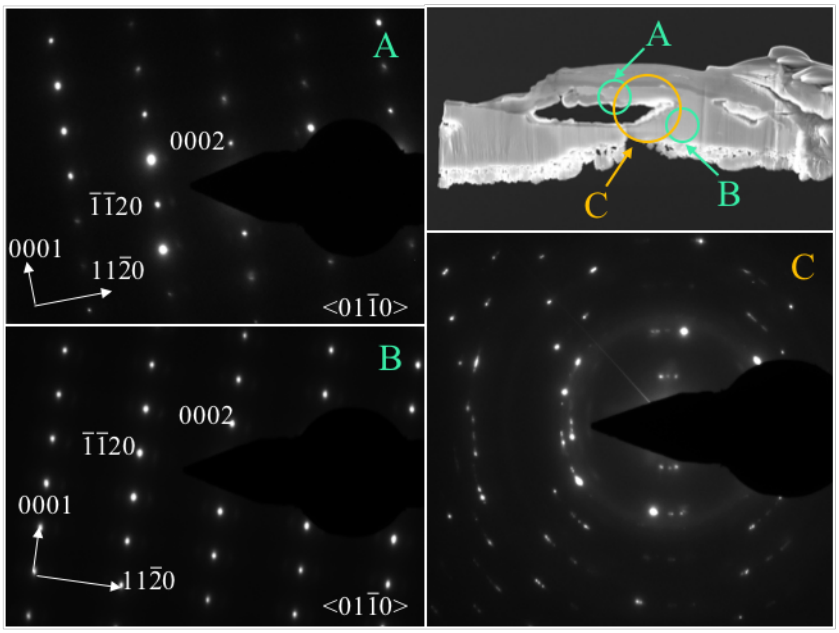

Figure 4.7, SAED patterns acquired from regions labelled A, B, and C in a SEM image of the FIB-milled TEM sample of the dendrite.

X-ray diffraction analysis

TEM studies have been useful in the determination of local crystal structure, crystallinity, and crystallographic orientation within the dendrites. X-ray diffraction (XRD) can help determine the crystallinity and the orientation relationships between the flakes and trunks over larger sizes of the sample and hence verify whether the TEM data is representative of the entire electrodeposit. Fig. 4.8(a) is a typical 2θ-ω scan obtained from a millimeter-sized electrodeposited dendrite. Only 0002 and 0004 reflections of HCP-Zn are observed indicating that the dendrites are single-crystals with the basal planes parallel to the substrate plane. Fig. 4.8(b) shows representative ω-rocking curve obtained around 2θ = 37.62° from the same sample. Two peaks are observed, a higher intensity peak around ω = 0° and a secondary peak around ω ~ 18°. Full width half maximum of the higher intensity peak was about 2.3° indicating that the deposit has a fairly good single crystalline nature. I attribute the second peak to diffraction from the out-of-plane flake.

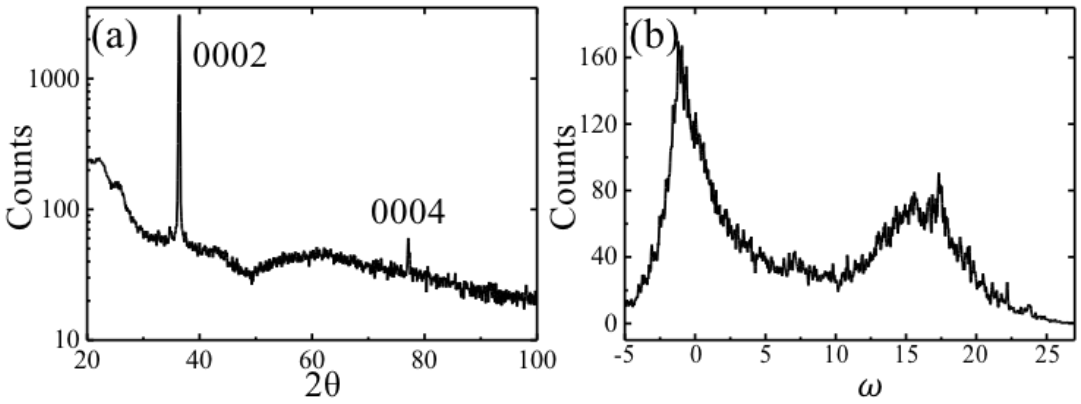

Figure 4.8, X-ray diffraction (XRD) data, (a) 2θ-ω and (b) ω scans, obtained from a millimeter-scale electrodeposited dendrite sample.

As demonstrated in the TEM SAED patterns, the out-of-plane flakes and the trunk are both {0001}-oriented single-crystals whose $\langle 01\,\bar{1}\,0\rangle$ are rotated by ~19° with each other. This relationship is further verified by XRD data.

4.3.4 Discussion

In our experiments, oscillations in the current (I) and in the growth rate occurred during electrodeposition at a constant potential [Fig. 4.9(a)]. Out-of-plane flakes are found to be growing in sync with the current oscillations. Based on these observations, I propose a model for the growth of Zn dendrites. The schematics A, B, and C in Fig. 4.9(b) illustrate three different stages corresponding to stages I, II, and III, respectively of the dendrite growth process. While a constant potential is applied to the electrodes, Zn(II) ions near the vicinity of cathode are driven towards the electrode surface by the electrical field. The maxima in current |I| (stage I), coincide with the maxima in the rate of Zn electrodeposition. I suggest that this fast growth occurs on the prism planes of the Zn, as illustrated by the arrows in the image labeled A in Fig. 4.9(b). This is plausible since higher current density is known to favor electrodeposition along the prism planes. The fast growth causes a rapid depletion of the Zn ions and consequently the electrodeposition process

becomes diffusion limited. As Zn ions are depleted, the current values begin to decrease. In the diffusion-limited regime, the depletion layer width reaches its maximum. And it takes longer time for Zn ions to reach the electrode surfaces. Thus, the current and growth rate are both low. When the stage II is reached, the Zn concentration at electrode surface becomes zero, which leads to a sudden decrease in the current. During this period, the electrodeposition continues to occur as indicated by a secondary growth peak in the black curve in Fig. 4.9(a) and results in the out-of-plane flakes, as shown in image labeled B. However, the reasons leading to growth at an angle are not clear. After stage II, when current density is low, the trunk growth with basal plane orientation is favored but the growth rate is low due to the low flux (current density). Zn ion concentration gradually recovers, and greater Zn flux is reestablished in stage III and the growth on the prism plane is recovered (image C). By repeating this process, the current oscillates synchronized with the flake and the trunk growth.

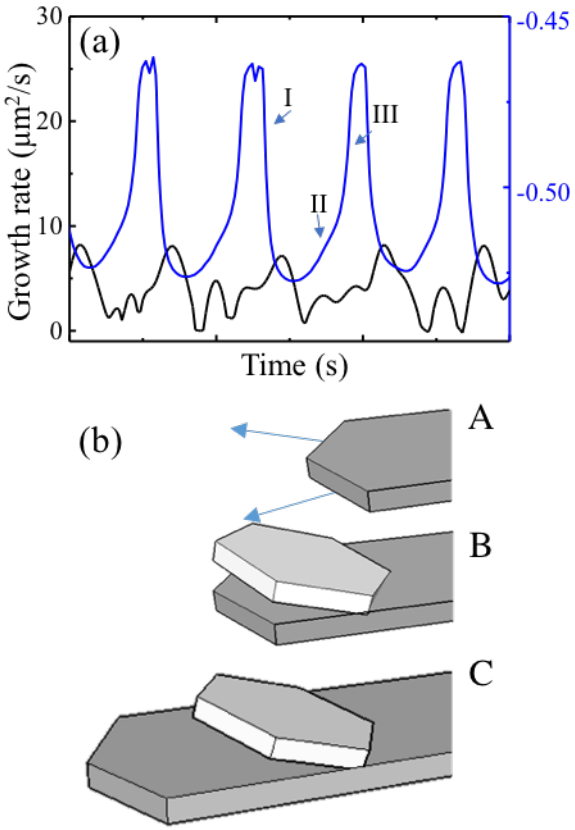

Figure 4.9, (a) Plot of growth rate and current oscillation as function of deposition time. (b) A schematic showing the oscillatory growth mechanism.

During electrodeposition at constant voltage, I observed oscillatory growth of Zn dendrites with periodic changes in both morphology and current. From *in situ* optical microscopy data in combination with the measured current responses, I determined that the oscillations in the dendrite growth rates are in sync with those in the current. Using electron microscopy and x-ray diffraction, I identified the three-dimensional microstructure of the dendrites. Based upon my data, I propose that at higher current densities, electrodeposition occurs at a fast rate along the prism direction. As the Zn ions are depleted, electrodeposition continues in the diffusion-limited regime during which nucleation occurs on the basal plane and leads to the formation of out-of-plane flakes. This oscillatory phenomenon is observed over a certain range of pH and overpotential values. The future

aspect of this study aims to understand the kinetics of nucleation of the out-of-plane flakes, which will provide new insights into the factors leading to the formation of high aspect ratio dendrites.

4.4 Conclusions

In summary, spontaneous oscillatory growth behavior is observed during Zn electrodeposition under specific conditions. I used *in situ* optical microscopy coupled with electrochemical Hele-Shaw cell to investigate the Zn dendrite growth behavior. From the analysis of *in situ* optical microscopy movies and concurrently measured current signals, I verified that the growth oscillations are synchronized with the current fluctuations. Cross-sectional SEM and TEM measurements demonstrated that the oscillatory growth resulted in a multi-layer growth morphology. In addition, the layered structure originated due to branching in a new crystallographic direction. Electron diffraction data in combination with XRD omega scans helped establish that the dendrites are made of {0001}-oriented Zn crystallites and the layered microstructure is a consequence of growth along two directions.

Chapter 5

5 *In situ* atomic force microscopy studies of Zn electrodeposition and the effect of pH

In situ atomic force microscopy (AFM) enables direct observation of Zn nucleation and growth during electrodeposition. With resolution capable of imaging atomic steps, AFM has demonstrated itself to be the one of the best tools for the determination of surface morphology. In addition, AFM operation is noninvasive and requires minimal sample preparation, which makes it an ideal *in situ* technique for studying a variety of surface dynamical phenomena including nucleation and growth of thin films, surface phase transitions, reactions, etc.

5.1 Introduction to *in situ* atomic force microscopy (AFM)

5.1.1 *In situ* AFM imaging

AFM is a scanning probe technique that involves rastering a fine tip over the surface of sample, measuring the local tip-sample forces. An AFM is typically built on four components, namely, a cantilever, a piezoelectric transducer, a position sensitive photodetector, and a feedback control loop. To acquire an AFM image, the deflection of cantilever is measured using the optical lever. The optical lever operates by reflecting a laser on the back of cantilever and being received by a position sensitive photodetector. As a result, the deflection of the cantilever is measured by the position of the laser spot on the position sensitive photodetector. The height of the AFM cantilever is controlled by the piezoelectric transducer, which expands under applied potential. The feedback loop is used to adjust the height of the cantilever holder to restore the deflection to a constant and pre-defined value. Therefore, the height of the cantilever driven by the piezoelectric transducer represents the sample surface topography.

AFM scanning probes are sharp pyramidal-shaped, a few micrometers-high, tips, typically made from silicon and silicon nitride, fabricated at the end of a cantilever, which is also typically

made of silicon or silicon nitride. The aspect ratios of AFM tips may vary depending on the application. When the tip is brought into proximity of a sample surface, the cantilever deflects due to repulsive forces between the tip and sample surface. This force is measurable using Hooke's Law when the length and spring constant are known for the cantilever.

AFM can be operated in two major modes: contact mode and tapping mode. During contact mode imaging, the AFM tip is in direct contact with the sample. The surface topography is measured using the deflection of the cantilever (constant height) or the feedback responses required to keep the deflection at a constant value (constant force). In tapping mode, the cantilever is driven to oscillate at resonant frequency. A known driving signal near resonant frequency results in a constant cantilever oscillation amplitude. When the tip is brought closer to the surface, the tip-surface interaction causes the amplitude to change. This change in amplitude is then used as the feedback to restore the tip-sample distance via feedback loop. AFM tapping mode is therefore a dynamic imaging mode with reduced sample damage.

5.1.2 *In situ* AFM analysis

AFM images are not just pictures; they reflect accurate topographic information that can be used for quantitative surface analysis. AFM images are typically presented as color maps, where the intensity of each pixel represents a measured height value at that position.

Surface roughness is one of the measurable parameters, accessible through AFM image analysis. Among all the different forms of roughness expressions, the most commonly used one is root-mean square roughness (RMS) that can be calculated by formula:

$$\mathrm{RMS} = \sqrt{\frac{1}{n}\sum_{i=1}^{n}\left|y_i^2\right|}, \qquad [5.1]$$

where n is the number of data points and y is the height measurement of the data point i. Higher RMS value implies a greater variation in surface roughness.

Topographic measurements such as grain sizes, step heights, and particle shapes can be obtained from the AFM images. Gwyddion 2.45 software is employed to process the AFM images and to extract the data presented in this chapter.

5.2 *In situ* AFM experimental

This section overviews the experimental procedure for *in situ* AFM analysis of Zn electrodeposition. First, a detailed description is given of the electrochemical cell assembly. Second, the instrumentation is briefly described. Third, this section introduces the preparation methods for various types of substrates used in my experiments.

5.2.1 Electrochemical cell assembly

All the *in situ* AFM experiments are carried out in a commercially available electrochemical cell fabricated by Asylum Research using a MFP-3D original AFM. The electrochemical cell is made of polyether ether ketone (PEEK), which is known for its excellent chemical resistant. The reservoir for electrolyte is about 7 mL in volume. On the sidewall of the PEEK cell, four ports are designed for multiple purposes. One is used as a feedthrough for CE, a Zn wire (Alfa Aesar, 99.995%). Prior to assembly, the CE was cleaned in 0.5 M H_2SO_4 for 10 s to remove surface oxide and then dried using nitrogen gas. Another port is connected to a solution reservoir that serves as a salt bridge connecting a RE. The other two ports are used to allow flow of solution in the cell. Figure 5.1 is a photograph showing the final electrochemical AFM cell assembly.

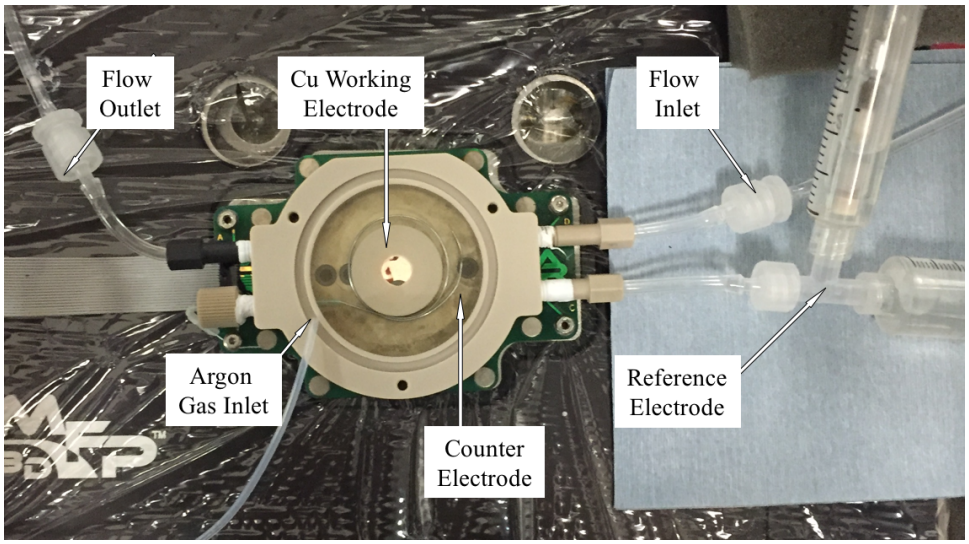

Figure 5.1, *In situ* electrochemical AFM cell assembly.

5.2.2 Instrumentation

Atomic force microscopy (AFM)

I used an Asylum MFP-3D AFM system to conduct my experiments. In most of the studies, I used a silicon nitride cantilever with a silicon nitride tip (OLYMPUS TR800PSA). These tips have a thin gold coating on the back-side of the cantilever to enhance the reflection of the laser. All the *in situ* electrochemical experiments are carried out using a Bio-Logic SP-300 potentiostat with a three-electrode cell with a stable RE.

Reference electrode (RE)

A mercury sulfate electrode (MSE) is employed as RE during *in situ* electrochemical experiments. The MSE potential is E = 0.64 V with respect to the normal hydrogen electrode (NHE). Prior to use, the MSE potential was calibrated with respect to silver chloride electrode (Ag/AgCl). In this chapter and following chapters, MSE will be the used as the primary RE.

Flow apparatus

When the pH needed to be precisely controlled, a pump (Harvard Apparatus PHD 200) is connected to provide a constant flow of solution at an adjustable flow rate. In cases where the

electrolyte needed to be changed (for example from pH = 3 to pH = 4), 36 mL (~5 times of reservoir volume) of new solution is purged through the cell.

5.2.3 Substrates and sample preparation

In the first set of pH experiments described in this chapter, polycrystalline copper and platinum are used. Later experiments will describe deposition on single-crystalline Cu(111) substrates.

Polycrystalline Cu foil

Polycrystalline Cu foils (10 mm × 10 mm × 25 μm) are used as working electrodes. Prior to the experiments, substrates were plasma cleaned for 10 minutes and submerged in 0.5 M H_2SO_4 for 2 minutes to remove the surface oxide. Subsequently, the electrode is well rinsed with Millipore water and dried with nitrogen gas. In order to prevent oxidation, the substrate is placed without delay in the cell and immersed in electrolyte solution.

Cu(111) single-crystal

Single-crystalline Cu(111) (MTI) (10 mm × 10 mm × 1 mm) substrates are also used as working electrodes. Electropolishing was carried out to prior to the experiments in 85% phosphoric acid. Detailed operating procedure is given in section 6.2.1.

Sputter-deposited Pt microelectrode

Pt thin films are also used as electrode material. Approximately 600-nm-thick layers of Pt are sputter-deposited within a 1-mm-diameter circular pattern on a 0.5-mm-thick, square-shaped glass wafer (see Fig. 5.2). Electrical contacts are achieved by depositing Pt on all the edges and on the backside. The cleaning procedure for Pt electrodes involves 10 minutes of plasma cleaning, followed by rinsing with ethanol, and Millipore water.

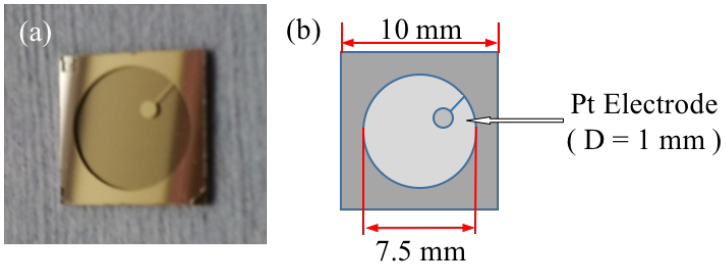

Figure 5.2, Pt electrode used in *in situ* AFM experiments.

5.3 Electrochemical methods

This section starts with an introduction to cyclic voltammetry (CV) technique followed by a presentation of the CV results obtained in the electrochemical AFM cell. With the help of the CV results, the electrochemical procedure used during *in situ* AFM is described in detail in this chapter.

5.3.1 Cyclic voltammetry

Cyclic voltammetry (CV) is an electrochemical method during which current response is measured while applying a linearly swept potential. CV analysis is often applied to obtain fundamental information about the redox reactions occurring in an electrochemical cell. It can also be useful in determining the reversibility of a reaction, the electron stoichiometry of a system, and the presence of intermediate products.

In this chapter, CV is primarily used to measure the formal reduction potential of Zn in $ZnSO_4$ electrolytes at various pH values. The cathodic (negative) current corresponded to the reduction of Zn(II) to Zn(0), while the anodic (positive) current corresponded to the oxidation of Zn(0) back to Zn(II). Figs. 5.3(a) and (b) show representative CVs of Zn electrodeposition in 0.1 M $ZnSO_4$ solutions with various pH. All the data are collected at a scan rate of 10 mV/s. The anodic peak positions are all approximately -0.9 V vs. MSE. Fig. 5.3(b) shows a portion of the plot

in Fig. 5.3(a) magnified around the zero current position, where I hold the electrodeposition process and acquired AFM images. At the zero current position, the surface is neither reducing nor oxidizing and thus I do not expect any deposition or dissolution.

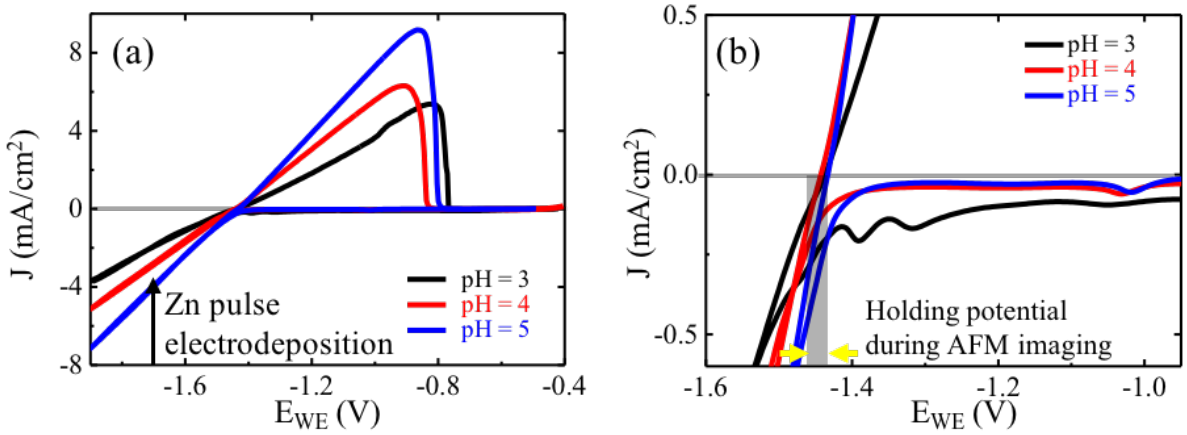

Figure 5.3, Cyclic voltammogram of (a) 0.1 M $ZnSO_4$ at pH = 3, 4, and 5. (b) Magnified view of the same data presented in (a).

5.3.2 Electrodeposition procedure

All the Zn electrodeposition experiments are carried out in 0.1 M $ZnSO_4$ solution prepared by dissolving anhydrous $ZnSO_4$ powder (Aldrich) in Millipore water. The solution pH is adjusted to 3.0, 4.0, and 5.0 by adding droplets of concentrated H_2SO_4 or KOH. Electrodeposition pulses are applied at a constant potential E_{WE} = -1.70 V vs. MSE [Fig. 5.3(a)]. The duration of each pulse is set to electrodeposit 100 monolayers (ML) of Zn. In Table 5.1, calculated amounts of charge transferred assuming 100% efficiency are presented. During electrodeposition, Zn^{2+} ions adsorb onto the electrode surface and subsequently reduce to Zn. In this chapter, the term 'pulse' will be used to refer to deposition thickness. During pulsing, the AFM cantilever is raised above the solution to prevent possible screening effects. AFM images are acquired between the pulses while holding the working electrode at a small reducing potential with negligible cathodic current passing through the cell. This holding potential is -1.42 ± 0.5 V vs. MSE [Fig. 5.3(b)] and is

determined from the zero current position in CV data at which point the deposit neither grows nor dissolves.

Table 5.1, Charge transferred in 100 ML of Zn electrodeposition.

	Polycrystalline Cu	Sputtered Pt
Area (mm^2)	31.7	0.785
Charge transferred (mC)	16.5	0.41

5.4 *In situ* electrochemical quartz crystal microbalance (EQCM)

5.4.1 Introduction to EQCM method

Quartz crystal microbalance (QCM) allows measurements of mass variations (Δm_{QCM}) through changes in oscillation frequency (Δf) of the crystal using Sauerbrey equation, which can be simplified as:

$$\Delta f = -C_f \cdot \Delta m_{QCM}, \qquad [5.2]$$

where C_f is the sensitivity factor of the crystal. QCM combined with the capability of measuring electrical response is known as electrochemical quartz crystal microbalance (EQCM). Using EQCM, mass variations and electrical responses can be measured simultaneously. The ratio of mass deposited during electrodeposition to the total charge transferred can be determined *in situ*.

5.4.2 Instrumentation and calibration

A Stanford Research QCM200 quartz crystal analyzer equipped with a 5 MHz AT-cut quartz crystal sputtered with Ti/Au is used for *in situ* EQCM measurements during electrodeposition at a constant current density -4 mA/cm^2 with a three-electrode setup in a beaker cell. The active electrode area is 40 mm^2. The quartz crystal holder is made of Teflon.

In order to ensure accurate measurements in my electrochemical setup, I first calibrated the QCM using the following method. Zn is electrodeposited in 0.1 M $ZnSO_4$ with pH = 3 at a constant

current of -4 mA/cm^2 for 10 minutes and the corresponding Δf recorded. Then the crystal is carefully rinsed in Millipore water and dried with nitrogen. The mass Δm_{QCM} of the resulting Zn film is measured by analytical balance (Mettler Toledo XP2u). The sensitivity factor, C_f is then determined using equation [5.2] and is found to be 105.81 Hz μg^{-1}. This C_f value is used in the analysis of all the results obtained for electrodeposition in 0.1 M $ZnSO_4$ solutions with pH = 3.0, 4.0, and 5.0. C_f is considered as a function of electrolyte concentration, however, the concentration varied little with pH in my experiments.

From Faraday's law, the change of mass (Δm_{Theory}) is proportional to the total charge (Q) transferred during electrodeposition and is given by the relation $\Delta m_{Theory} = \frac{Q \cdot MW}{z \cdot F}$, where MW = 65.38 gmol^{-1} is the molecular weight of Zn, z = 2 is the valence number of Zn ions, and F = 96485.33 Cmol^{-1} is the Faraday's constant. Using these values, I calculated Δm_{Theory} and Δm_{QCM} measured from electrodeposition of Zn in pH = 3 solution as described above; the ratio sets the electrodeposition efficiency, $\eta = \Delta m_{QCM}/\Delta m_{Theory}$, which for pH = 3 is found to be 91.92%. I assume the same η for electrodeposition of Zn in pH = 4 and 5 solutions.

5.5 Results and discussion

This section describes the use of *in situ* AFM along with *ex situ* SEM to study the morphological evolution of electrodeposited Zn and *in situ* EQCM to quantitatively relate the amount of material deposited to charge transferred. The section begins with description of surface morphologies and growth characteristics associated with pure Zn deposition in pH = 3, $ZnSO_4$ solution. The effects of substrate crystallinity and structure on the growth morphologies and

surface roughness evolutions are then discussed. Later part of the section deals with the change in surface morphology at higher pH and is shown to be associated with co-deposition of Zn and ZnO.

5.5.1 Morphology evolution

Polycrystalline Cu substrate

Figure 5.4 shows morphological evolution of Zn during electrodeposition on a polycrystalline Cu substrate from 0.1 M $ZnSO_4$ solution. The solution pH is maintained at 3.0 by continuously flowing the electrolyte. Electrodeposition is carried out in pulses at a potential of -1.7 V vs. MSE. Each pulse contained a fixed amount of charge needed to deposit 100 ML of Zn as shown in Table 5.1, assuming 100% efficiency. (However, the experimentally measured efficiency is 91.1%, which corresponds to deposition of ~91 ML per pulse.) Thickness labels in Fig. 5.4 are values expected for 100% efficiency. Between the pulses, the AFM tip is carefully relocated to image the same area so that the surface features can be followed across the scans.

After 100 ML of deposition, small (<100 nm in diameter) crystallites are observed over the field of view. These nuclei grow and coalesce to form a polycrystalline film. Fig. 5.4 shows the growth morphologies at thicknesses between 700 ML and 2900 ML. At 700 ML thickness, individual grains are clearly visible. With increasing thickness, I found that larger crystallites covered the entire surface, which either coalesced with or outgrew neighboring smaller crystals. Crystallographic orientation plays an important role in crystal growth behavior because of anisotropic growth rates and surface energies.

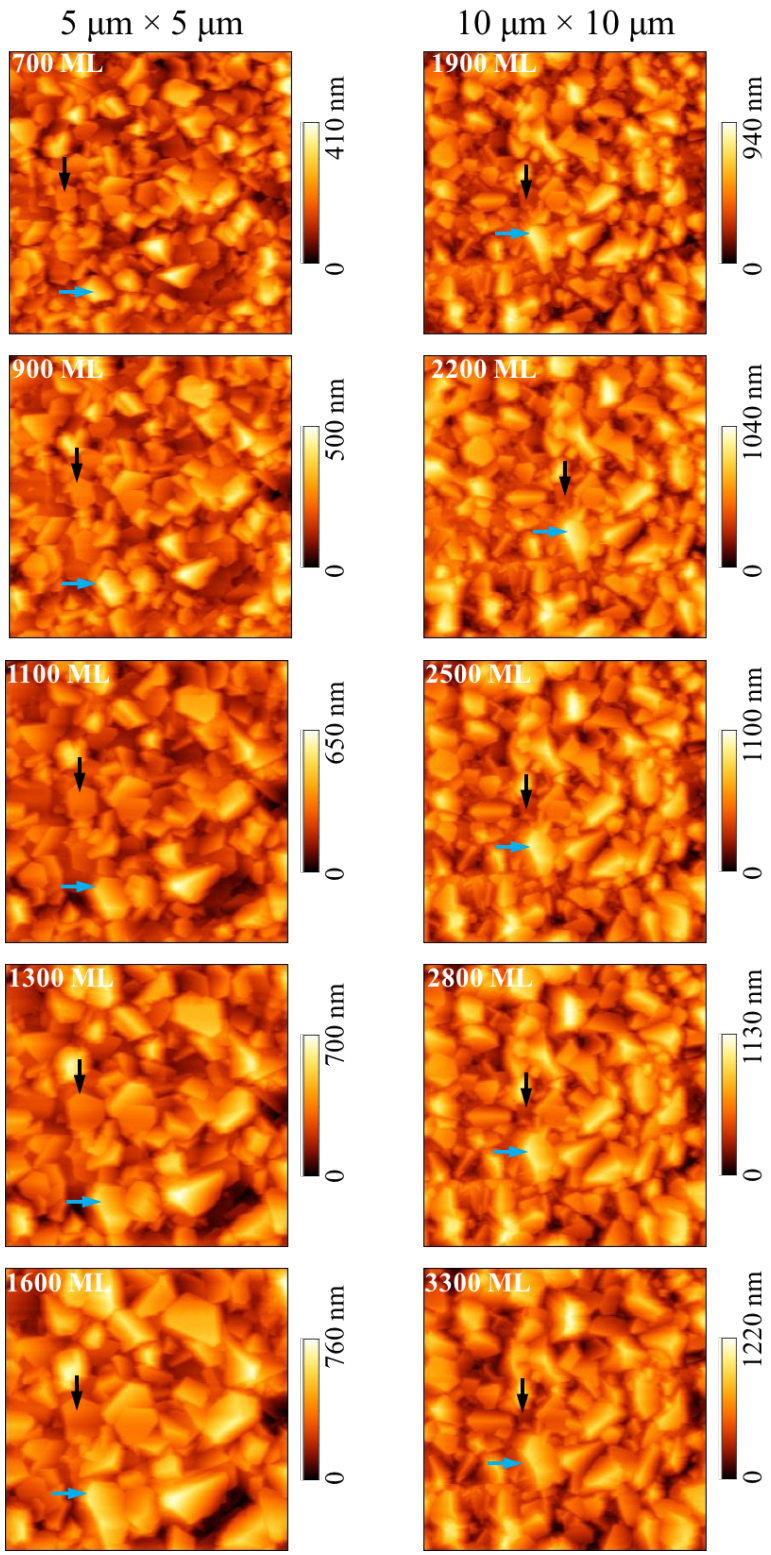

Figure 5.4, Sequential AFM images (height channel) acquired during electrodeposition of Zn on a polycrystalline Cu electrode. Arrows indicate the evolution of two crystallites with different orientation.

To gain more insight into the role of orientation, I tracked individual crystallites with different orientations. Basal oriented crystallite, such as the one highlighted by a black arrow, grew laterally but became covered by surrounding faster growing crystallites. In contrast, crystallite oriented with the prism facets pointing out of the substrate plane, such as the one highlighted by a blue arrow, grew at a much faster rate than the basal oriented crystallites. The fastest growth direction is the vector sum of the facet velocities and thus for hexagonal plates will be near the apex between two prismatic facets as is observed here.

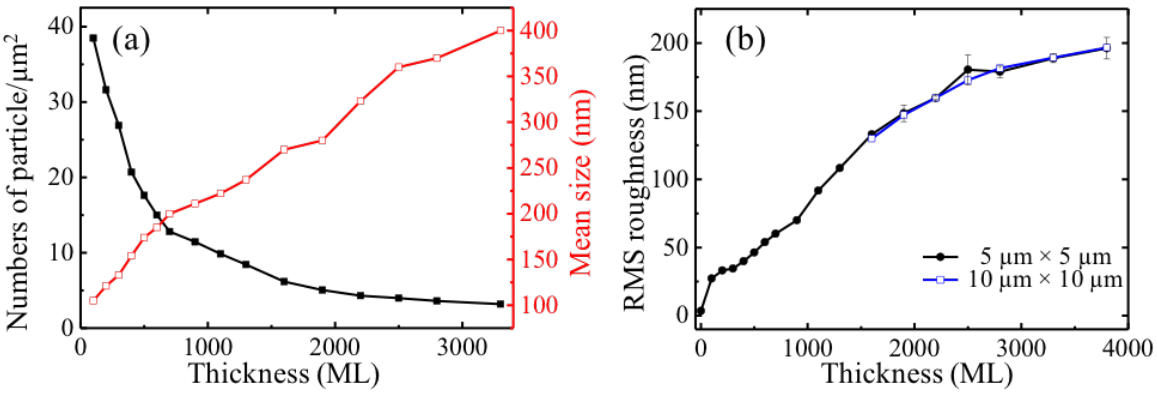

Figure 5.5, Plots of (a) number of crystallites per unit area (black) and mean size (red) and (b) root-mean square (RMS) roughness as a function of deposition thickness.

In Fig. 5.5(a), the areal number density and mean size of crystallites are plotted as a function of deposition thickness. As the growth progressed, the number of crystallites in the same field of view decreased, indicating that the existing Zn crystallites selectively grew instead of nucleating new crystallites. Fig. 5.5(b) is a plot of RMS roughness vs. thickness, which shows that the Zn surfaces become increasingly rougher with increasing thickness. I attribute this behavior to the out-of-plane growth of crystallites bounded by prismatic facets.

Single crystalline Cu(111) substrate

In order to investigate Zn electrodeposition kinetics and to minimize the role of substrate structure influencing the results, I chose Cu(111) single-crystals as the substrates. During *in situ*

AFM experiments, I observed two types of growth morphologies, island nucleation and step flow, depending on the step density of the underlying copper substrate.

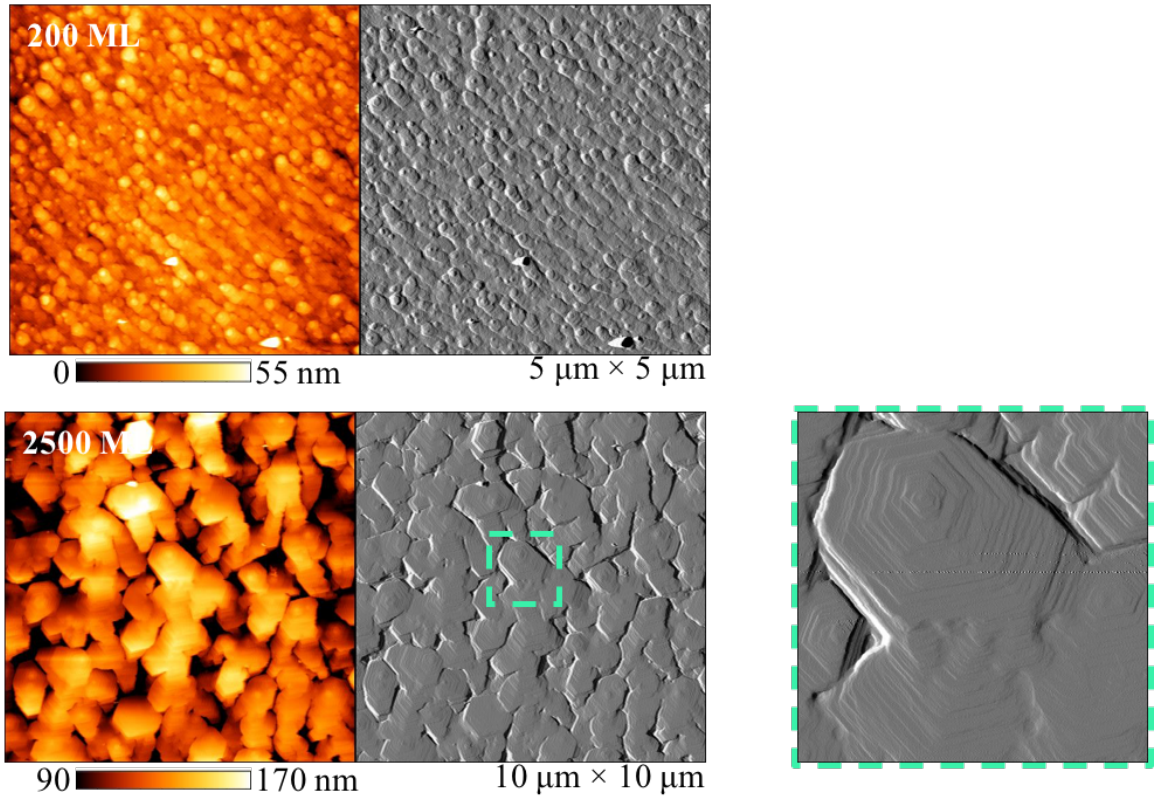

Figure 5.6, *In situ* AFM images (gold color: height channel, grey color: amplitude channel) acquired during Zn electrodeposition on a single-crystalline Cu(111) electrode. The image (2 × 2 μm^2) bounded by a dotted green box is a magnified view of the area highlighted in green.

Figure 5.6 shows island nucleation on relatively flat substrates. After 200 ML of deposition, the single-crystalline substrate surface is covered by crystallites with sizes around 100 ~ 200 nm in diameter. These small crystallites are all oriented in the same direction across the entire field of view, and some of them appear to be hexagonal in shape. With continued deposition, the crystallites increased in size with more pronounced hexagonal symmetry; this suggests that the basal facet is orientated parallel to the substrate. During growth, no new nuclei with different orientations are observed. At a thickness of 2500 ML, the surface appears to be smoother as the individual crystallites grew to similar heights and began to merge with each other. Because the

islands are crystallographically aligned, atomic steps are able to flow from one crystallite to another. Zooming in on a flat domain shows a more detailed view (green-boxed image in Fig. 5.6), where Zn atomic steps are clearly visible. At the center of this domain, steps are generated either from a surface-terminated screw dislocation or two-dimensional island nucleation. These steps then continuously grew out to the edge of the crystallites. Coalescence of domains can occur when steps from one domain propagate to its neighboring domain with a similar height.

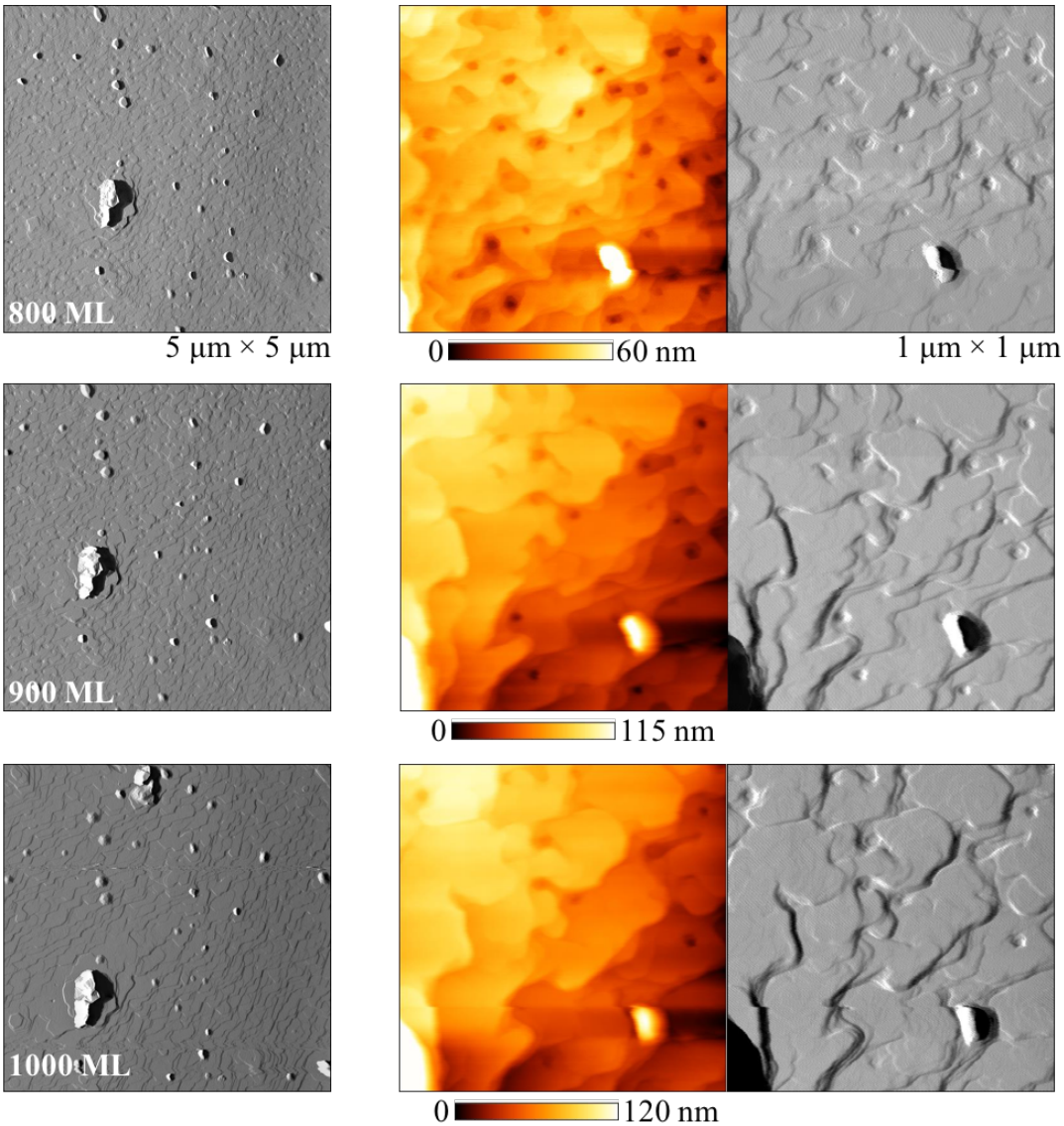

Figure 5.7, *In situ* AFM images (gold color: height channel, grey color: amplitude channel) acquired during Zn electrodeposition on a single-crystalline Cu(111) electrode. Left column shows the growth morphology on a larger scale. The center and the right columns show magnified views of central regions.

Figure 5.7 shows the second type of morphological evolution, which occurred on vicinal copper surfaces. In this case, growth is dominated by Zn steps that template the underlying copper. At a thickness of 800 ML, Zn surface with terraces and steps is observed (Fig. 5.7). After 1000 ML of deposition, wider and flatter terraces separated by steps or step bunches are visible. As shown in the higher magnification AFM images, steps appear less kinked and the surfaces increasingly smoother with increasing thickness.

In the same experiment, small 3D mounds with similar sizes (~250 nm in diameter, ~50 nm in height) are observed on the surfaces during deposition. Between 800 ML and 1000 ML, lateral or vertical sizes of these mounds did not change substantially. Figs. 5.8(a) and (b) show higher resolution images of two such mounds. The mound in Fig. 5.8(a) retained the same size although terrace steps around it continued to grow. This particular mound has a regular hexagonal shape; however, other mounds exhibit more complex polyhedral morphologies.

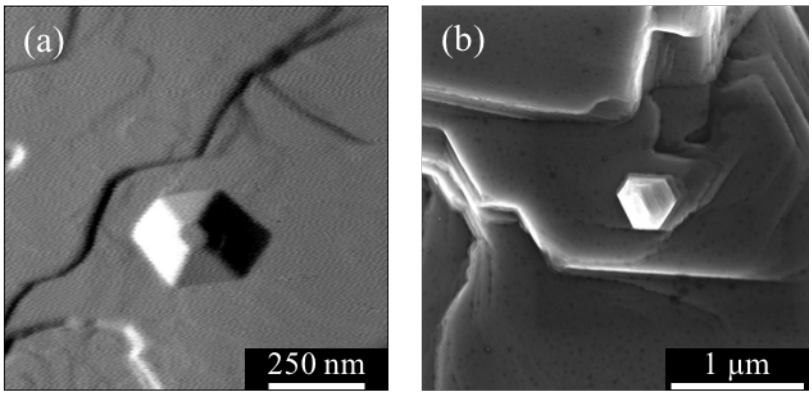

Figure 5.8, (a) *In situ* AFM image (amplitude channel) of a Zn mound. Image: 1 μm × 1 μm. (b) SEM image of the Zn mound.

As previously observed in the AFM images, electrodeposited Zn film appears to be crystallographically well-aligned both in-plane and out-of-plane with respect to the single-crystalline Cu(111) substrate. XRD data are obtained to determine the crystallinity of the as-deposited Zn layers. Fig. 5.9(a) shows a typical 2θ-ω scan obtained from the electrodeposited Zn film on Cu(111). In this plot, only the (0002) and (0004) reflections of HCP-Zn are present

indicating a strong out-of-plane [0001] orientation. Fig. 5.9(b) shows a ω-rocking curve for (0002) Zn reflection; the full width at half-maximum (FWHM) value of the (0002) peak is found to be 1.26°. In comparison, the FWHM value for the (111) peak of the single-crystalline Cu(111) substrate is measured to be 0.89°, indicating that mosaic spread of Zn film is fairly small and the crystallinity of the Zn film is comparable to that of the single-crystal Cu substrate. Fig. 5.9(c) shows x-ray pole figure generated by tilting (χ) the sample from 0° to 90°, and rotating (φ) the sample in 360°. To obtain this data, the diffractometer is set to a 2θ value, at which the Bragg condition for diffraction is satisfied. The pole figure data provides further evidence that the Zn films electrodeposited on single-crystalline Cu(111) are also single-crystalline.

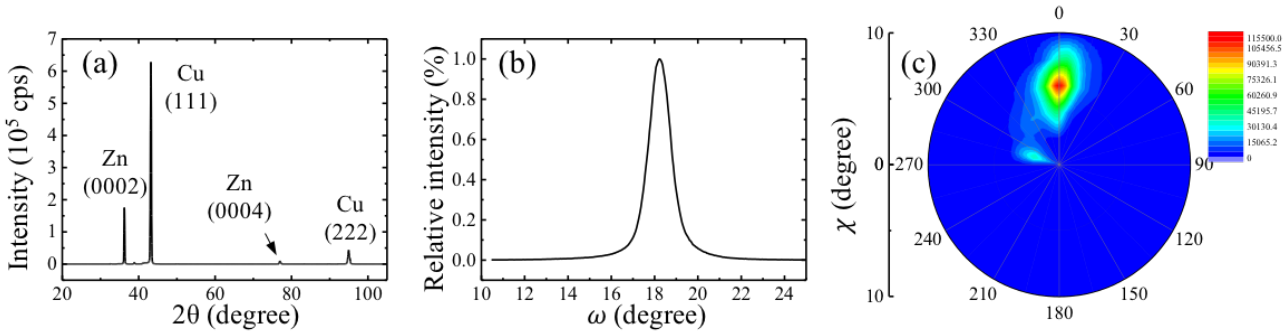

Figure 5.9, X-ray diffraction (XRD) measurements performed on a Zn film electrodeposited on single-crystalline Cu(111) substrate. (a) 2θ-ω spectrum. (b and c) rocking curve and pole figure for Zn(0002) reflection, respectively.

Sputter-deposited Pt microelectrode

I have also carried out Zn electrodeposition on sputter-deposited Pt microelectrodes using 0.1 M $ZnSO_4$ solution with pH = 3 under conditions similar to those used for the growth on polycrystalline Cu substrates. Fig. 5.10 shows a comparison of morphological evolution of Zn films on polycrystalline Cu and Pt microelectrode substrates.

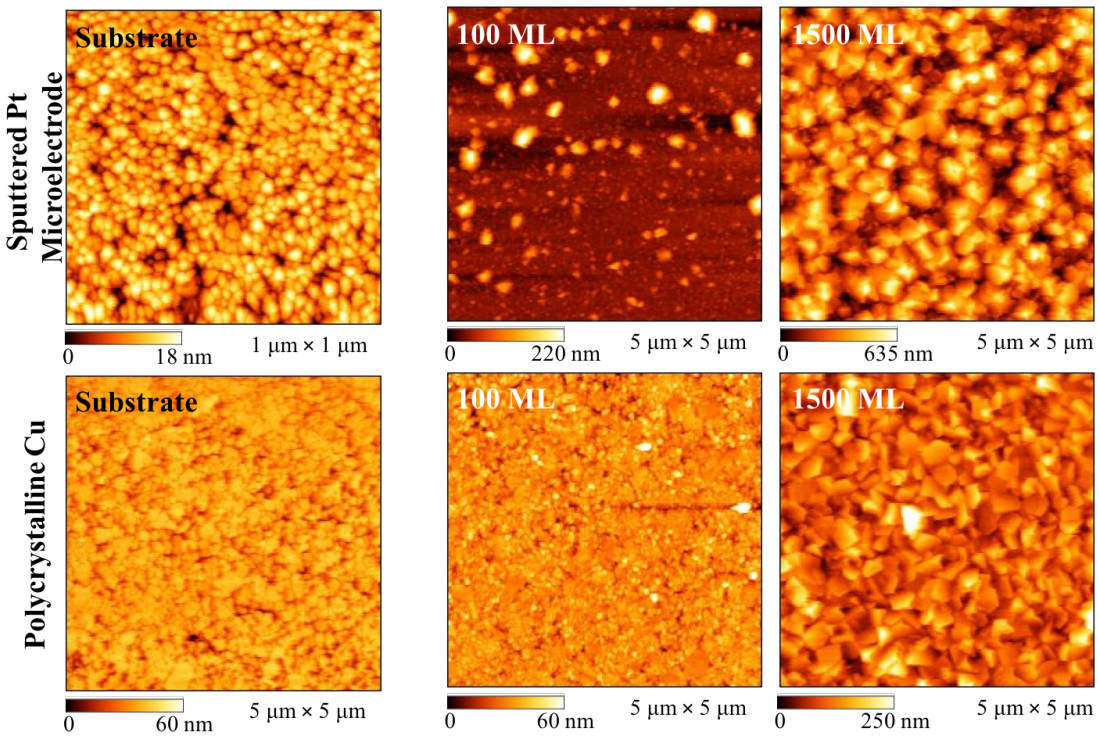

Figure 5.10, *In situ* AFM images acquired from the surfaces of the sputter-deposited Pt microelectrode and polycrystalline Cu substrate (left column), and from the surfaces of electrodeposited Zn at a thickness of 100 ML (middle column) and 1500 ML (right column).

The RMS roughness of bare Pt microelectrode is 2.0 nm, less than the value (5.7 nm) measured on polycrystalline Cu substrates. After the deposition of first 100 ML, I observed fewer crystallites and lower coverage on the Pt microelectrode compared to homogeneous deposition on polycrystalline Cu substrates. With increasing thickness, both the surfaces become progressively rougher. However, Zn layers on Pt electrodes appear less dense with higher aspect ratio features. The AFM images of Zn films deposited on Cu substrates reveal more basal {0001} facets covering the surface, resulting in relatively smoother surfaces. Fig. 11 is a plot of RMS roughness values obtained as a function of Zn film thickness on both Pt and Cu substrates. Clearly, Zn layers on Pt microelectrodes are rougher than on Cu. On Pt, roughness increases sharply during early stages of growth and up to a deposition thickness of 1000 ML beyond which the roughness varies little with increasing thickness. In comparison, roughness of the Zn layers on Cu substrate increase

monotonically with increasing thickness. The observed differences in roughness evolution can be attributed to the differences in the nucleation density and crystallite orientation on the two substrates. On Pt, fewer nuclei form, which then grow into larger crystallites. It is also likely that the Zn layers grow with non-basal facets oriented normal to the substrate. Surface coverage continues to increase as new nuclei form. I speculate that these factors contribute to a sharp increase in roughness during the first 1000 ML of deposition. Within the 1000 ML of deposition, nucleation density becomes saturated and all the deposited material is captured by existing crystallites. As a result, the roughness values vary little at thicknesses above 1000 ML. On Cu substrate, nucleation density is high and preferential growth of basal facets from the onset of deposition leads to relatively smoother films. I attribute the steady increase in roughness with increasing thickness to the polycrystallinity of the Zn layer and the anisotropic out-of-plane growth rates of facets with different orientations.

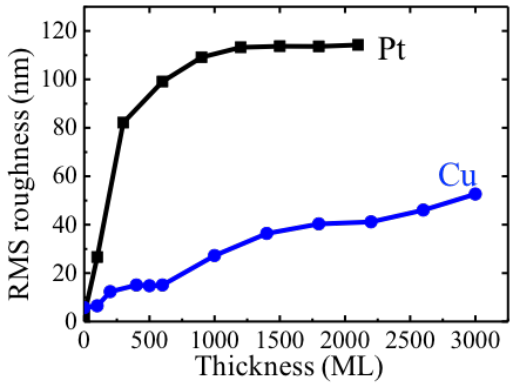

Figure 5.11, RMS roughness plotted versus deposition thickness for the electrodeposited Zn film on sputter-deposited Pt microelectrode (black) and polycrystalline Cu (blue) substrates.

5.5.2 pH effect on Morphology

Solution pH and the formation of ZnO are suggested as the factors contributing to oscillatory growth observed in Hele-Shaw experiments (e.g., Fig. 4.4). In this section, I take the first step towards understanding the effect of pH on the electrodeposited Zn morphology. Base

solutions of 0.1 M $ZnSO_4$ have a pH of approximately 4.3. The solution pH can be modified in two ways: either directly by adding acid or base to the starting solutions, or dynamically by electrochemically reducing dissolved oxygen, which in turn generates OH^- at the electrode interface. As I will demonstrate, higher pH values stabilize ZnO, which will precipitate above a threshold pH value (theoretically 6.3). I found that solutions with pH > 5 are difficult to make because ZnO would spontaneously precipitate (due to locally high supersaturation) while the pH is being adjusted. Therefore, I compare electrodepositions from starting solutions with pH = 3, 4, and 5. *In situ* electrochemical AFM observations presented in this section are acquired in $ZnSO_4$ solutions without flow. The lack of flow allows the surface pH (relative to starting solution) to increase with time due to the reduction of dissolved oxygen to OH^-.

Figure 5.12 shows *in situ* AFM images of the surface morphological evolution during electrodeposition of Zn on polycrystalline Cu substrate in 0.1 M $ZnSO_4$ with starting pH = 3, 4, and 5 in the left, center, and right columns, respectively. In the pH = 3 solution, during the first 100 ML of deposition [Fig. 5.12(a)], I observed small Zn crystallites, which appear to nucleate uniformly across the substrate. I note that Zn alloys with Cu during the electrodeposition process; however, at a deposition thickness of 100 ML, the observed morphology is primarily due to nucleation and growth of Zn. With increasing number of deposition pulses, i.e. increasing thickness, the smaller crystallites grew and coalesced into larger hexagonally-faceted crystals oriented randomly with respect to the substrate [Figs. 5.12(b) and (c)]. Although the surface pH is increasing with time (due to the lack of flow), the observed morphological evolution behavior is qualitatively similar to that observed in Fig. 5.4, where the electrodeposition was also carried out in solution with pH = 3 but with a flowing electrolyte to maintain the electrode pH at 3. I will show later that these morphologies correspond to pure Zn.

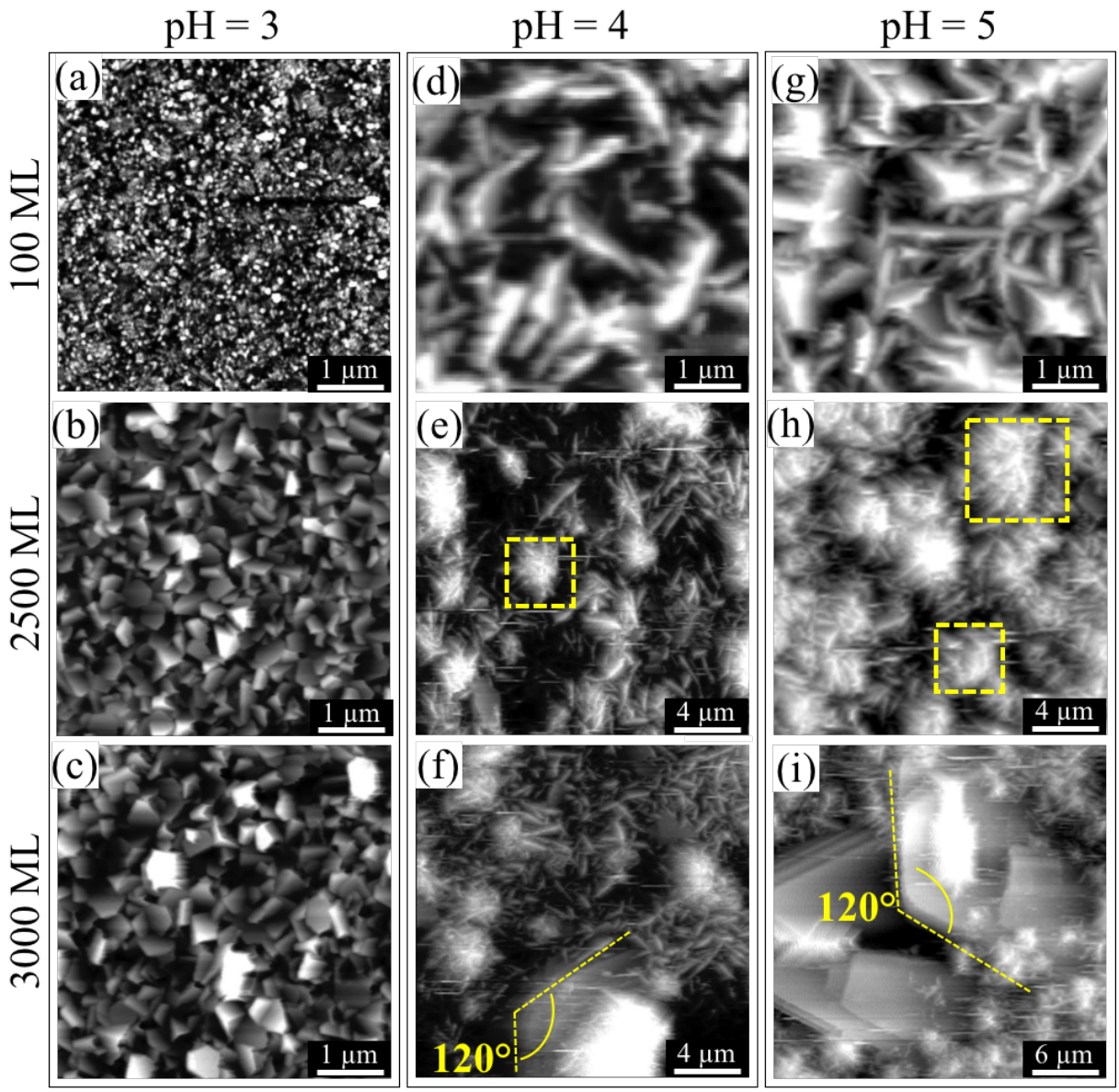

Figure 5.12, (a-i) *In situ* AFM images obtained from polycrystalline Cu samples during electrodeposition of Zn from 0.1 M $ZnSO_4$ solutions with pH adjusted to (a-c) 3.0, (d-f) 4.0, and (g-i) 5.0. The AFM images in the first, second, and third rows show surface morphologies after deposition thicknesses equivalent to 100, 2500, and 3000 ML, respectively.

In contrast to the growth morphologies obtained at pH = 3, AFM images obtained from the Cu foils after the deposition of the first 100 ML in solutions with higher pH, i.e. pH = 4 [Fig. 5.12(d)] and pH = 5 [Fig. 5.12(g)] show the formation of vertical flake-like features with higher aspect ratios. As the film thickness increases, clusters of multiple flakes appear, highlighted by dashed yellow squares in Figs. 5.12(e) and (h). The cluster size and number density increased with increasing deposition thickness and with the pH from 4 to 5.

In 3000-ML-thick Zn films deposited in both pH = 4 [Fig. 5.12(f)] and pH = 5 [Fig. 5.12(i)] solutions, I observed larger and thicker hexagonal plates with 120° vertices, highlighted by dashed yellow lines in Figs. 5.12(f) and (i); the hexagonal plates are larger when deposited from pH = 5 compared to those grown in pH = 4 solution. Growth of these large plates is fast compared to the AFM image acquisition times in my experiments. I was not able to capture the nucleation of these large plates, which appear over the entire field of view (30 × 30 μm^2) upon formation.

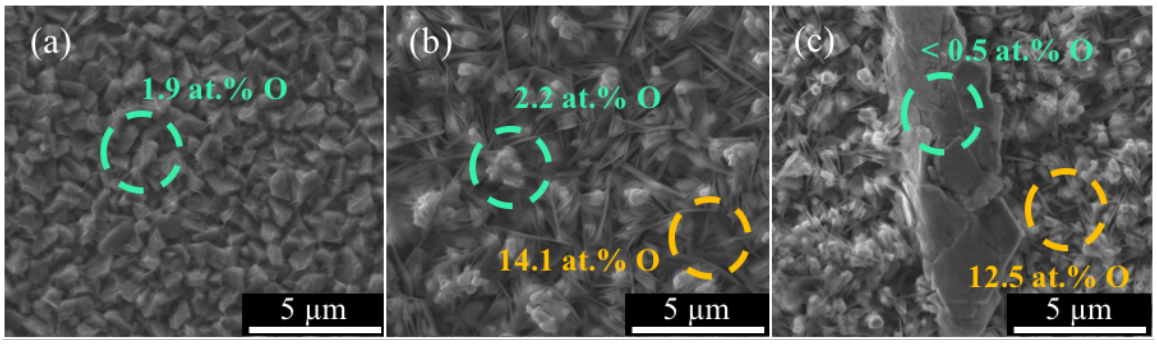

Figure 5.13, *Ex situ* SEM images acquired after electrodeposition of Zn from 0.1 M $ZnSO_4$ solution with starting pH = (a) 3.0, (b) 4.0, and (c) 5.0.

Using energy dispersive spectroscopy (EDS) in the SEM, I determined composition of the deposits. Fig. 5.13 shows typical SEM images along with EDS-measured oxygen contents in selected regions on the surfaces of the electrodeposits. Both the AFM and the SEM images [e.g., Figs. 5.12(c) and 5.13(a)] of surface grown in pH = 3 are consistent and show polycrystalline surfaces composed of blocky hexagonal crystals. Point-mode EDS data acquired from the surface

revealed low (< 2 at.%) oxygen concentration, which I interpret as equivalent to a pure Zn surface that is exposed to air after growth. The AFM and SEM images [e.g., Figs. 5.12(f) vs. 5.13(b) and 5.12(i) vs. 5.13(c)] of surfaces electrodeposited from solutions with higher pH values (= 4 and 5) differed from one another. The AFM measures the true topography of the surface, which is dominated by the high aspect ratio flakes. In contrast, the SEM image contrast depends on electron-surface interactions and electron penetration depth. Because the flakes are electron-transparent, the SEM images display the underlying film. Regions with high density of high aspect ratio flakes, for example, those highlighted by a yellow dashed circles in Figs. 5.13(b) and (c), have high oxygen content (>12 at. %). I suggest that these high aspect ratio flakes are likely ZnO and the measured values of oxygen content (which are considerably lower than 50 at.% expected for O in ZnO) reflect the fact that the ZnO flakes sit on top of a Zn film. I provide supporting evidence below that the formation of ZnO is favored in higher pH solutions. EDS data acquired from regions bounded by green dashed circles in Fig. 5.13 show fairly low oxygen concentrations suggesting that these regions are composed of pure Zn. As seen in Fig. 5.13(c), the large hexagonal plates have negligible oxygen content and are consistent with pure Zn.

5.5.3 EQCM

I used EQCM to perform quantitative analysis on mass changes during electrodeposition. Fig. 5.14 shows typical plots of mass changes measured during and after electrodeposition under conditions similar to those used in my *in situ* AFM experiments. When a constant current (-4 mA/cm^2) is applied [Fig. 5.14(a)], the mass of the quartz crystal (electrode) started to increase linearly as a function of time (t) and charge transferred (Q = It). The growth rate given by the slopes of the curves increased with solution pH. To be specific, the electrodeposited mass growth

rates R_t measured in solutions with pH = 4 and pH = 5 are higher by 0.15 µg/s and 0.27 µg/s, respectively than the rate obtained from pH = 3 solution (see Table 5.2 below).

Table 5.2, Quantitative analysis based on EQCM measurements of mass deposited in $ZnSO_4$ solutions with pH = 3, 4, and 5. $R_q = \frac{\partial m_{QCM}}{z \cdot F^{-1} \cdot \partial Q}$; (Z = 2) is the mass deposited per 2 mol of electrons transferred; R_q* is R_q corrected using 91.92% efficiency; $R_t = \frac{\partial m_{QCM}}{I \cdot \partial t}$ is the deposition rate; ΔR_t (= $R_t - R_{t,\, pH = 3}$) is the difference in deposition rate measured with respect to the rate of deposition in pH = 3 solution; M is the mass deposited during 10 minutes of constant current electrodeposition; r is the average rate of mass deposited in the first 30 s after turning off the current.

pH	R_q(µg/2 mol of e)	R_q*(µg/2 mol of e)	R_t(µg/s)	ΔR_t(µg/s)	M (µg)	r (µg/s)
3	60.90	65.54	1.69	-	1028.44	-0.08
4	64.35	70.00	1.84	0.15	1130.88	0.15
5	68.74	74.78	1.96	0.27	1208.59	0.27

From EDS analysis (and *in situ* WAXS data in Chapter 6), I demonstrated that only Zn is deposited from pH = 3 solution and both Zn and ZnO co-electrodeposited from pH = 4 (and higher) solutions. Based on these results, I suggest that electrodeposition in pH = 4 and pH = 5 solutions is a dual deposition process. The first process is Zn electrodeposition, where Zn^{2+} ions are reduced and Zn is deposited. The second process is consistent with ZnO precipitation because my EQCM data indicated that mass gain increases with increasing solution pH. To identify the mechanism leading to ZnO formation, I carried out the following experiments. After electrodeposition, the coated electrode was left in electrolyte for 10 minutes under open circuit condition. In pH = 3 solution [Fig. 5.14(b)], the mass decreased with time indicative of Zn dissolution. In pH = 4 and pH = 5 solutions, however, I observed an increase in mass at initial times. The deposition rate decreased gradually with increasing time. At later times, there are no detectable changes in the mass of the sample. This demonstrates that ZnO formation continued after the current stopped, and likely prevented Zn dissolution in pH = 4 and pH = 5 solutions. I obtained the ZnO deposition rates under open circuit potential conditions from the QCM data in the first 30 s after the current

was stopped. The average growth rates are 0.15 μg/s and 0.27 μg/s in pH = 4 and pH = 5 solutions, respectively. These ZnO formation rates (in the absence of current) are identical to the rate differences ΔR_t obtained during electrodeposition (see Table 5.2). That is, ZnO deposition rate when the current is on is the same as the rate measured during a short time period after the current is stopped. These EQCM results show that the process of ZnO formation is not a direct redox reaction because it does not require a current but rather a pH-dependent chemical reaction.

The pH is a function of both the starting solution and electrochemical drive. To address the influence of electrochemical drive on the growth rate, I made a fresh Zn-coated electrode using pH = 3 solution (using the same conditions as above) and promptly transferred it into fresh pH = 4 solution right after the current stopped. Fig. 5.14(c) shows the mass change after current is stopped. EQCM measurements for 60 minutes under open circuit condition showed that the mass increase obtained from the fresh pH = 4 solution was much less than in pH = 4 solution, where electrodeposition had already occurred. In addition, the mass increase eventually stopped in fresh solution as indicated by a plateau observed in the black curve in Fig. 5.14(c), while in the other case, the mass gain increased although at a declining rate. This suggested that a pure Zn surface does not dissolve in solution with pH = 4 or higher, presumably due to the formation of a passivating ZnO layer. Additionally, a pH = 4 solution modified by an electrodeposition current would have a higher concentration of OH^- built up leading to a higher precipitation yield of ZnO compared to fresh pH = 4 solution.

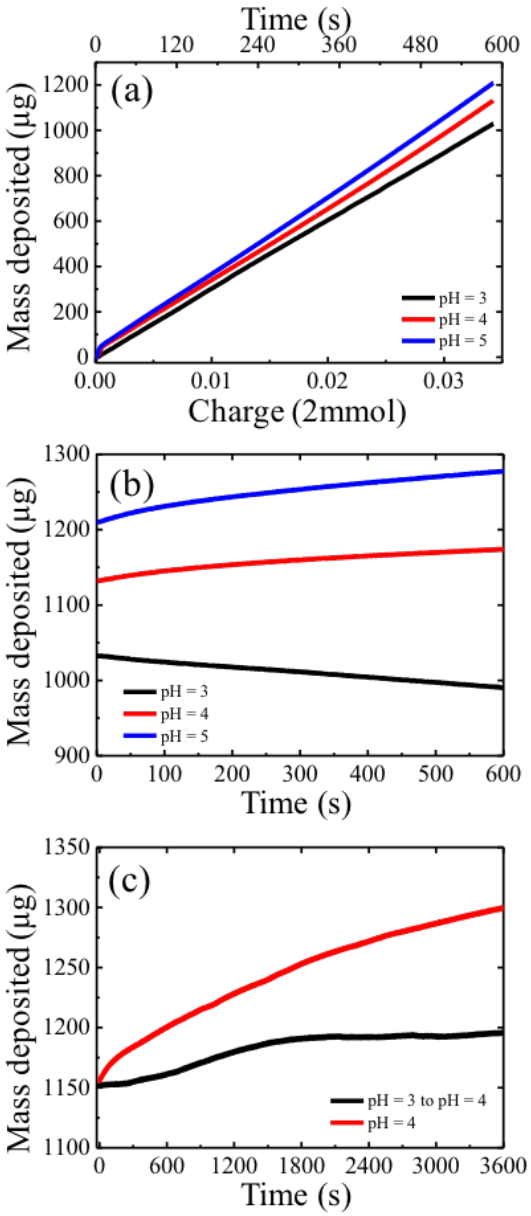

Figure 5.14, Electrochemical quartz crystal microbalance (EQCM) measurements of mass change on active area plotted as a function of time (a) during electrodeposition at a constant current of -5.48 mA (-4 mA/cm^2) for 10 minutes and (b) after electrodeposition, i.e. with the current turned off, in pH = 3 (black), 4 (red), and 5 (blue) solutions. The data in (b) is obtained when a freshly deposited substrate is soaked in the original setup. In (c), time-dependent changes in mass deposited after a substrate deposited in pH = 3 was transferred to a fresh pH = 4 (black) solution are compared with those measured from a substrate deposited and kept in pH = 4 (red).

5.5.4 Discussion

Morphological Evolution

In the study based on polycrystalline substrates, the number of crystallites in the same field of view decreased indicating that the deposited Zn crystallites are selectively growing larger instead of nucleating new crystallites. Each crystallite is composed of atomically-flat surfaces with few steps or islands, typical for growth conditions, where the nucleation rate is slow compared to the step propagation rate. Once an island nucleates, the atomic steps quickly propagate to the crystal edges leaving behind a smooth, step-free terrace. In addition, Zn grew faster in the prismatic direction. The differences in growth rate lead to the final morphology and aspect ratios of the features shown in Fig. 5.4.

In the study of Zn electrodeposition on single-crystalline Cu(111), two types of growth morphologies are observed. In the first type, electrodeposition of Zn occurred via nucleation and growth of 2D islands and/or surface-terminated screw dislocations (spiral steps) and resulted in morphologies observed in Fig. 5.6. In the second type, step flow dominated the growth of Zn layers. Furthermore, polyhedral crystallites appeared on the single-crystalline surfaces. The size and orientation of these 3D crystallites did not seem to change with time and the fact that they did not interact with the terraces during growth indicated that these features are misaligned with respect to the epitaxially deposited Zn layers.

pH effect on morphology

My AFM studies demonstrated that the surface morphologies of electrodeposited Zn depend on the pH of the solution. In order to understand this phenomenon, I focused on the determination of chemical composition of the electrodeposits as a function of solution pH, which is difficult for two reasons: differentiating Zn from ZnO based on *in situ* AFM images of the surface morphologies is challenging because both Zn and ZnO have hexagonal symmetry; *ex situ*

EDS data obtained from air-exposed samples is not conclusive because Zn oxidizes readily when exposed to air and can form ZnO (particularly if high surface area features such as flakes retain some moisture after removal from solution). To address this aspect, I performed *in situ* WAXS experiments (details are presented in chapter 6) and unambiguously determined that ZnO formed during deposition rather than upon exposure to air. Interpretation of my results is made difficult by the fact that gradients in solution concentration and pH can develop over time because the electrolyte is not actively flowed during deposition. To systematically study the effect of pH, I carried out *in situ* electrochemical AFM experiments using a flow cell to maintain a constant pH. The *in situ* WAXS and AFM results are presented in the following Chapter 6.

EQCM

I demonstrated that ZnO deposition rate is the same with and without current. This indicated that ZnO formation is not governed by electrodeposition reactions but is consistent with electro-precipitation process. In the following section, I present a plausible pathway for ZnO formation.

Hydroxyl ions created by reducing dissolved oxygen, can raise the surface pH initiating the chemical precipitation ZnO via reaction 5.3:

$$Zn^{2+} + 2OH^- \rightarrow ZnO + H_2O \qquad [5.3]$$

or the hydroxyl ions can initiate the precipitation of $Zn(OH)_2$, which can then convert to ZnO via reactions:

$$Zn^{2+} + 2OH^- \rightarrow Zn(OH)_2 \quad \text{and} \quad Zn(OH)_2 \rightarrow ZnO + H_2O \qquad [5.4]$$

Both possible precipitation paths are related to hydroxyl ion concentrations through equilibrium reactions

$$Zn(OH)_2 \text{ or } (ZnO + H_2O) \overset{\beta}{\Leftrightarrow} Zn^{2+} + 2OH^- \qquad [5.5]$$

In Eq. (5.5), β represents the equilibrium constant for both paths:

$$\beta = \gamma_{Zn^{2+}}[Zn^{2+}]\gamma_{OH^-}{}^2[OH^-]^2, \quad [5.6]$$

where γ is the activity coefficient. $\gamma_{Zn^{2+}} = 0.3$ (according to Davies equation and with ionic strength μ = 0.4 M for the solutions used here) and $\gamma_{OH^-} = 1$. Near the cathode surface, a higher concentration of OH^- builds up through reduction of dissolved oxygen resulting in a shift of equilibrium towards ZnO precipitation. Similarly, higher bulk solution pH (higher OH^- concentration) leads to an increase in ZnO precipitation. (This is consistent with the experimental result of higher ZnO yield in pH = 5 than in pH = 4 solution, when Zn^{2+} concentration remained the same.) After turning off the current, the supersaturation remained the same for a short time period. As time progresses, the supersaturation decreases as the OH^- concentration near the surface is depleted, because there is no new supply of OH^- from the cathodic reaction. Consequently, the precipitation rates of ZnO decrease gradually with time in both pH = 4 and pH = 5 solutions [Fig. 5.14(b)]. In a separate experiment, as further evidence of OH^- build-up at the interface, I observed a continuous weight gain during the first 60 minutes after the current was stopped.

5.6 Conclusions

During the *in situ* AFM study, I observed the morphological evolution during Zn electrodeposition on poly- and single-crystalline Cu substrates and on sputter-deposited Pt microelectrodes. For the electrodeposition on polycrystalline Cu and Pt substrates, Zn electrodeposition formed polycrystalline films and prismatic facets were preferred growth facets. On single-crystalline Cu(111), 2D island formation and step flow are found to be the two major growth modes. XRD analysis demonstrated the growth of single-crystalline Zn(0002) films on Cu(111).

During the study of the effect of pH on electrodeposition, I first observed that the growth morphologies are sensitive to solution pH when Zn is electrodeposited from 0.1 M $ZnSO_4$ solutions. I found that both Zn and ZnO co-deposited at high pH values leading to both morphological and compositional changes in the film. I further clarified the co-electrodeposition process using *in situ* EQCM. I found that ZnO continued to precipitate after the electrodeposition current is stopped and the precipitation rate is the same during and for short times after the electrodeposition. Based on the electrochemical reactions, I propose that ZnO precipitation originates from increased supersaturation, which is caused by local OH- concentration built-up through the reduction of dissolved oxygen. To conclude, ZnO precipitated simultaneously with Zn electrodeposition through a chemical rather than electrochemical reaction when pH fell within in a certain range.

Chapter 6

6 *In situ* studies of ZnO electrodeposition kinetics

Electrodeposition has received increasing attention as a promising method for synthesizing ZnO films with controllable nanostructure. Methods to electrodeposit in several different electrolytes have been developed but are based on empirical investigations. In this chapter, I describe the use of three *in situ* techniques, *in situ* AFM, EQCM, and WAXS, to investigate the growth mechanisms operating during electrodeposition of ZnO and thereby develop fundamental understanding of the ZnO electrodeposition process. The insights gained from my study will ultimately lead to more precise control of the ZnO nanostructure and hence desired properties.

6.1 Introduction to ZnO electrodeposition

ZnO is a promising wide band gap material for a range of applications that include optical, photovoltaic, and photocatalytic devices. There has been recent interest in the solution-phase synthesis of ZnO because it is a low cost and versatile method to integrate thin films onto substrates. The prevailing mechanistic models for ZnO growth from neutral or acidic solutions describe two different crystallization scenarios. The first scenario proposes that metastable phases such as $Zn(OH)_2$ form initially. These metastable phases serve as reservoir rich in Zn and oxygen from which ZnO nucleation is driven by dehydration reaction:

$$Zn^{2+} + 2OH^- \rightarrow Zn(OH)_2 \rightarrow ZnO + 2H_2O \qquad [6.1]$$

The second scenario proposes that ZnO growth occurs via solution precipitation of ZnO; ZnO colloids nucleate in the solution and then attach to the substrate.

$$Zn^{2+} + 2OH^- \rightarrow ZnO + 2H_2O \qquad [6.2]$$

Nucleation and growth behaviors impact the microstructure and morphology, and hence electrical and optical performances, of the deposited material. Fundamental understanding of the

nucleation and growth mechanisms often requires tools capable of accurate measurements of 2D island formation and atomic step propagation rates. However, there have not been such systematic studies of ZnO nucleation and growth kinetics. In this chapter, I present results from the use of three *in situ* tools: *in situ* AFM to image ZnO nucleation and growth dynamics, *in situ* WAXS to verify material phase and structure, and *in situ* EQCM to measure film growth rates.

To understand the interplay between Zn and ZnO growth, it is helpful to lay out the chemical potentials for important reactions (Fig. 6.1). During ZnO electrodeposition, oxygen is the source of oxidation from the solution and the associated reaction is

$$O_2 + 2H_2O + 4e^- \rightarrow 4OH^-,\ E^0_{OH^-} = -0.24\ \text{V vs. MSE}, \qquad [6.3]$$

where the MSE standard potential E = 0.64 V vs NHE. In the literature, the formation of ZnO is typically reported in terms of an overall reaction:

$$Zn^{2+} + 0.5O_2 + 2e^- \rightarrow ZnO,\ E_{ZnO}{}^{theory} = 0.29\ \text{V vs. MSE}. \qquad [6.4]$$

In Eq. (6.4), $E_{ZnO}{}^{theory}$ is derived based on the thermodynamic data[62]. Theoretically, at potentials more reducing than $E_{ZnO}{}^{theory}$, ZnO electrodeposition will occur. However, experimentally, ZnO is only observed to grow with measurable rates at significantly more reducing potential values ranging from -0.8 V to -1.3 V vs MSE[64-66]. Here, I chose $E_{ZnO}{}^{expt}$ = -0.8 V vs MSE, since most controlled growth is carried out below this deposition potential. Additionally, Zn electrodeposition based on Zn(II) ion reduction follows:

$$Zn^{2+} + 2e^- \rightarrow Zn,\ E^0_{Zn} = -1.44\ \text{V vs. MSE} \qquad [6.5]$$

Thus, at a potential more reducing than E^0_{Zn}, Zn(II) ions will be deposited in the form of Zn(0). Conversely at a potential more oxidizing than E^0_{Zn}, preexisting Zn(0) will dissolve. This provides an opportunity to explore three cases as exemplified by potentials labeled E_1, E_2, and E_3 in Fig. 6.1(a): at E_1, both Zn and ZnO deposit as has been described in chapter 5; at E_2, Zn neither grows

nor dissolves but ZnO grows; at E_3, Zn dissolves but ZnO grows. In all the cases, ZnO deposition is pH dependent and will only grow if the pH is sufficiently high. I would like to point out that all of my experiments are carried out at potentials well above the copper oxidation potential.

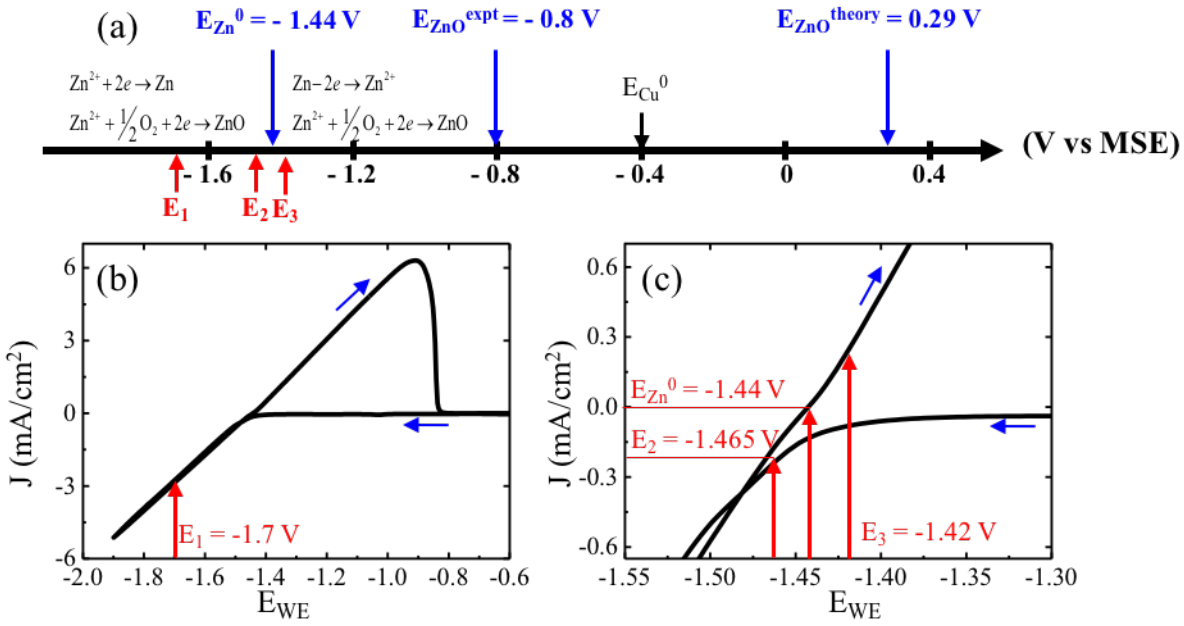

Figure 6.1, (a) Schematic representation of the electrochemical reactions during ZnO and Zn electrodeposition. (b) Cyclic voltammogram and (c) magnified view of the plot in (b) for 0.1 M $ZnSO_4$ at pH = 4.

6.2 *In situ* AFM method

This section describes the experimental procedure based on the previous experimental design used in chapter 5 for *in situ* AFM observations during ZnO electrodepositions. In addition, a detailed procedure of single-crystalline substrate preparation is provided.

6.2.1 Electropolishing: single-crystalline substrate preparation

Electropolishing is a process that gradually removes material through electrochemical etching. During the process, the sample will serve as anode, where material gets oxidized and dissolved into the electrolyte.

In this chapter, single-crystalline Cu(111) (MTI) (10 mm × 10 mm × 1mm) substrates electropolished using 85% phosphoric acid. First, the Cu substrate is mounted on a customer designed sample holder. The sample holder is assembled into a rotating disk electrode. Electrical connection to the substrate is achieved through a gold pin touching the backside of the Cu electrode. A two-electrode arrangement is used with the Cu substrates serving as the anode, and a Pt wire as the cathode. A potentiostat (Bio-logic SP300) ias used to apply a constant current density 10 mA/cm^2 for 10 minutes while the anode is rotated at 500 rpm.

6.2.2 *In situ* AFM experimental procedure

The AFM instrumentation and image acquisition procedure are the same as described in section 5.2 of the previous chapter. Here, I present only the essential electrochemical parameters that are used in these experiments. The standard electrode potentials for Zn (E_{Zn}^0 = -1.44 V) and both theoretical and experimental values for ZnO are indicated by blue arrows in Fig. 6.1(a). Fig. 6.1(b) is a CV diagram acquired in the AFM cell with the pH = 4, 0.1 M $ZnSO_4$ solution at 10 mV/s. E_1 = -1.7 V, is the potential used for Zn electrodeposition. Figure 6.1(c) is a portion of the CV diagram in Fig. 6.1(b) magnified to show the plot details at potentials from -1.55 V to -1.30 V. E_{Zn}^0 = -1.44 V is where cathodic current became zero. E_2 = -1.465 V is under a small reducing current (J_2 = - 0.22 mA/cm^2), where Zn growth is expected to be minimal. E_3 = -1.42 V is under an oxidizing current, where an existing Zn surface would dissolve.

6.3 *In situ* wide-angle X-ray scattering (WAXS)

This section overviews the WAXS technique and experimental methods used to show unambiguously that ZnO formed under my experimental conditions and to determine whether other crystalline intermediates were also present as is hypothesized in literature[63]. This section

starts with a brief introduction to the theory and synchrotron facility and ends with a detailed description of the experimental design.

6.3.1 Introduction to WAXS

Wide-angle X-ray scattering is an X-ray diffraction technique that is used to determine crystalline structure based on Bragg's law. WAXS provides the same structural information as the more commonly used XRD technique. WAXS differs from a related technique, small-angle X-ray scattering (SAXS), in that the detector is positioned to acquire larger angle diffraction peaks.

6.3.2 Facility and specification

The WAXS data are acquired using 24 keV (λ = 0.5166 Å) photons in sector 9 of the Advance Photon Source (APS) located at Argonne National Laboratory, Illinois, USA. In the APS WAXS experimental geometry, the X-ray beam first passes through a monochromator, two mirrors for harmonic energy reflection and beam defining before it is scattered by the sample. A 2D WAXS detector (PILATUS 300K.W) is employed to acquire diffraction patterns. The sample to detector length is calibrated to be 328.00 mm using silver behenate as a standard reference material.

6.3.3 Experimental design

The electrochemical experiments within the WAXS instrument are carried out using a coin cell made using PDMS housing and glassy carbon window. The working electrodes (WE) are made from the same copper foil used in the AFM experiments, and the CE/RE is a Zn wire (Alfa Aesar, 99.995%). The WE is positioned normal to the incident beam. The beam is transmitted through the glassy carbon window, solution reservoir, and then the WE foil. The thickness of the solution layer is 2 mm, and the total volume of solution is about 0.22 mL. Electrodeposition is conducted by applying a constant potential E_{WE} = -1 V vs. Zn (-2.4 V vs. MSE) for 10 min. In

order to maintain current density similar to -4 mA/cm^2, which is used in my other experiments, I chose to use higher potential for this setup. Time series data are acquired by exposing the sample to X-ray beam (spot size 1.5 mm × 0.8 mm) for 10 s at 30 s intervals.

6.4 Data analysis and discussion

This section deals with studies of ZnO formation during electrodeposition using different *in situ* techniques. First, *in situ* WAXS results identified ZnO as an electrodeposition product from 0.1 M $ZnSO_4$ solution with pH = 4. Second, *in situ* AFM is used to monitor the morphological evolution and study the growth kinetics on single-crystalline substrates. At two different applied potentials, deposition of ZnO only (E_2) and co-deposition of Zn and ZnO (E_1) are observed. In addition, the co-deposition of Zn and ZnO growth kinetics is studied on polycrystalline substrates with applied potential at E_1. In order to understand ZnO growth mechanism, *in situ* EQCM results are correlated with *in situ* AFM experiments carried out at similar conditions with an applied potential E_2. Third, ZnO growth is studied at a potential (E_3), where Zn dissolves.

6.4.1 Distinguishing ZnO from Zn

In situ WAXS experiments are carried out to identify ZnO and to investigate changes in composition due to increasing the solution pH from 3 to 4. During the electrodeposition, a constant potential E = -1.0 V vs. Zn CE (-2.4 V vs. MSE) is applied to the WE for 600 s. Fig. 6.2(a) shows the circular integrated X-ray diffraction patterns obtained from polycrystalline Cu foil before and after the electrodeposition for 600 s in pH = 3 and 4 solutions. The WAXS data from bare substrate (black) shows copper reflections, as expected. After deposition in pH = 3 solution (red), characteristic Zn peaks with k = 2.54 Å^{-1}, 2.72 Å^{-1}, 4.68 Å^{-1},4.71 Å^{-1}, 5.59 Å^{-1} etc. (Table 6.1) are observed in the WAXS patterns. In pH = 4 solution (blue), reflections corresponding to both Zn and ZnO are observed.

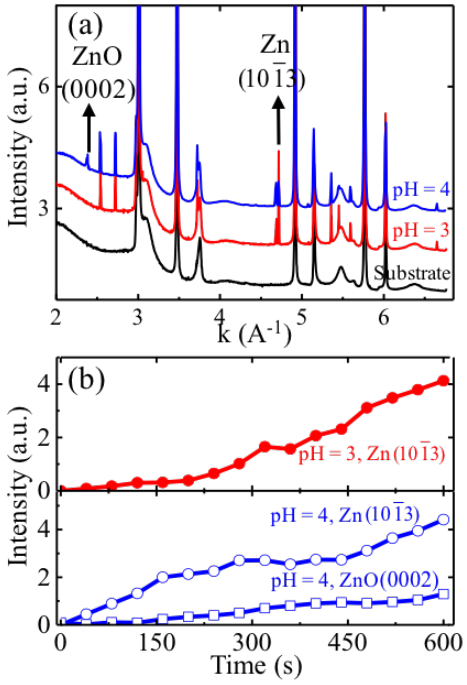

Figure 6.2, *In situ* wide angle X-ray scattering (WAXS) spectra acquired from a bare Cu substrate (black), and from Zn samples electrodeposited for 600 s from 0.1 M $ZnSO_4$ solutions with pH = 3 (red curve) and pH = 4 (blue curve). (b) Plots showing time-dependent changes in the integrated peak intensities of Zn(10$\bar{1}$3) and ZnO(0002) reflections, normalized to the Cu substrate peak at k = 3.00 Å^{-1}.

Fig. 6.2(b) shows time-dependent changes in the structure and/or composition of the deposited material. These WAXS experiments are carried out by taking diffraction data every 30 s (exposure time 10 s). In the upper panel of Fig. 6.2(b), the peak intensity of Zn(10$\bar{1}$3) normalized with respect to the intensity of the Cu(111) peak is plotted as a function of time. The Zn peak intensities increased with increasing deposition time indicating that the Zn films grew thicker. Similar behavior is observed in pH = 4 solution (Fig. 6.2(b) lower panel), i.e. electrodeposited Zn thickness increased with deposition time. At ~120 s, a new peak at k = 2.41 Å^{-1} corresponding to the characteristic peak of ZnO(0002) appeared. The intensity of ZnO peak, normalized with respect to the Cu(111) peak intensity, is low compared to that of Zn because the amount of ZnO deposited

is less than that of Zn. Additionally, the ZnO peak intensity also increased as a function of electrodeposition time, indicating that the amount of ZnO deposited increased with time.

Table 6.1, X-ray powder diffraction peaks for Zn, ZnO, and $Zn(OH)_2$. Eight strongest peaks are selected for each compound.

	Zn			ZnO			$Zn(OH)_2$	
$k_{Zn}(Å^{-1})$	**h k l**	**Intensity**	**$k_{ZnO}(Å^{-1})$**	**h k l**	**Intensity**	**$k_{Zn(OH)2}(Å^{-1})$**	**h k l**	**Intensity**
2.541	0 0 2	53	2.233	1 0 0	57	1.425	1 1 0	100
2.722	1 0 0	40	2.414	0 0 2	44	1.478	1 0 1	80
3.005	1 0 1	100	2.538	1 0 1	100	1.915	1 1 1	100
3.724	1 0 2	28	3.288	1 0 2	23	1.956	2 0 1	80
4.682	1 0 3	25	3.867	1 1 0	32	2.304	2 1 1	80
4.717	1 1 0	21	4.254	1 0 3	29	2.557	0 0 2	60
5.357	1 1 2	23	4.559	1 1 2	23	2.750	0 2 1	80
5.592	2 0 1	17	5.075	2 0 2	4	2.847	3 1 1	80

6.4.2 Electrodeposition of ZnO on single-crystalline substrate

This section deals with ZnO growth behavior on single-crystalline substrates during electrodeposition in 0.1 M $ZnSO_4$ solution with pH = 4. The growth behavior at two deposition potentials are compared using *in situ* AFM images. First set of electrodeposition experiments are carried out at E_2 = -1.465 V, where only ZnO is deposited. The second set of experiments are carried out at E_1 = -1.7 V, where both Zn and ZnO are co-deposited.

Electrodeposition at E_2 = -1.465 V: growth of ZnO while holding Zn static

Figure 6.3(a) shows a typical AFM image of single-crystalline Zn(0001) surface obtained by electrodepositing 3000 ML of Zn on a Cu(111) substrate using 0.1 M $ZnSO_4$ with pH = 3 at E_1 = -1.7 V vs. MSE. The Zn steps are visible in the image and the measured step height of 4.8 ± 0.15 Å corresponds to monoatomic steps on Zn(0002). After the growth of Zn layers, the electrolyte pH is changed from 3 to 4 solution and the potential value to E_2 = -1.465 V. At E_2, which is close to the open circuit potential value (-1.44 V), Zn neither grows nor dissolves. During the solution

exchange, which took about 10 minutes, using a syringe pump, the AFM tip is retracted from the surface and stopped scanning the surface. At t = 25 minutes, scanning was resumed at the same location and the first image at the new potential E_2 and in pH = 4 solution is obtained at t = 33 minutes [Fig. 6.3(b)]. Thus, the potential is held at E_2 = -1.465 V for 25 minutes while the electrolyte pH is changed to 4. In Fig. 6.3(b), an ~16-nm-high ZnO crystallite with an incomplete hexagonal shape is observed on the surface. In the following AFM scan [Fig. 6.3(c)], the ZnO crystallite did not retain the hexagonal shape, became smaller [Fig. 6.3(c)], and eventually disappeared [Fig. 6.3(d)]. This is likely because AFM images are acquired in contact mode. Loosely bonded particles can be removed due to tip-surface interactions. ZnO crystallites removed from the surface would have a higher propensity to re-dissolve because of the local concentration variations. Furthermore, since the potential is maintained at E_2, Zn does not dissolve. This is evident from the AFM images of underlying Zn steps (highlighted by solid blue lines) in Figs. 6.3(c) and (d), which appear to be stationary.

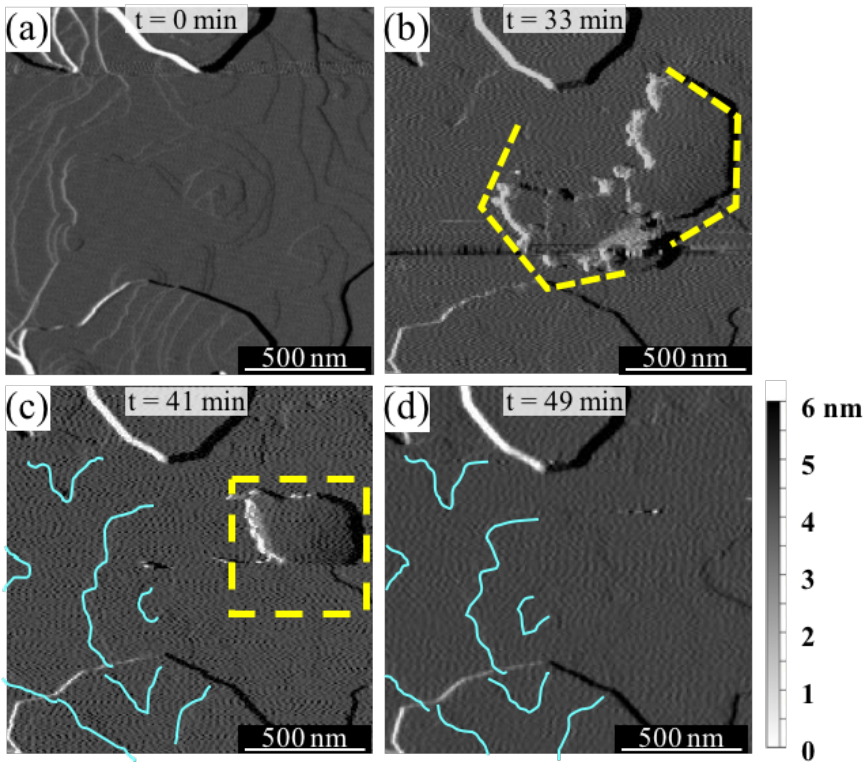

Figure 6.3, *In situ* AFM images (deflection channel) obtained from (a) 3000-ML-thick Zn electrodeposited on Cu(111) at E_1 = -1.7 V vs. MSE in 0.1 M $ZnSO_4$ solution with pH = 3 and (b-d) the same surface at E_2 = -1.465 V with solution pH = 4. The image scan rate is 1.09 Hz, which corresponds to 8 min./scan. The labels denote the times t immediately following the acquisition of AFM images. From t = 0 ~ 10 min., the electrolyte is exchanged with pH = 4 solution and the potential set to E_2 = -1.465 V. Images (b)-(d) are consecutive scans obtained from the location highlighted by a yellow box in (a). Yellow dashed lines and the box in (b) and (c) show a 3D ZnO crystallite. Blue lines in (c) and (d) highlight monoatomic steps on the underlying Zn surfaces.
Electrodeposition at E_1 = -1.7 V, co-deposition of Zn and ZnO

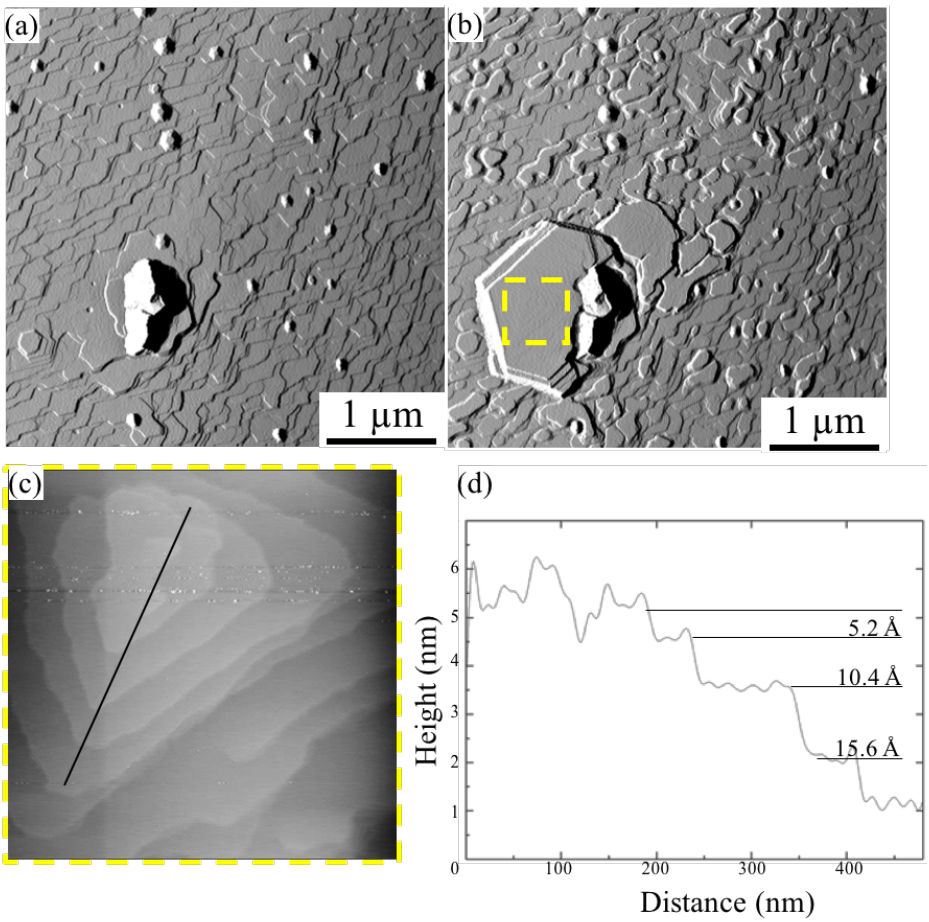

Figure 6.4, *In situ* AFM images (deflection channel) obtained from (a) 1000-ML-thick Zn on Cu(111) in 0.1 M $ZnSO_4$ solution with pH = 3 and (b) after electrodeposition of additional 100 ML in the solution with pH = 4. In this measurement sequence, the electrodeposition potential is held constant at E_1 = -1.7 V. (c) Higher magnification AFM image (height channel) obtained from the area highlighted by a yellow dashed box. (d) Surface height profile obtained along the black line shown in (c).

Figure 6.4(a) shows a representative AFM image of single-crystalline Zn(0002) surface obtained after electrodeposition of 1000 ML of Zn from 0.1 M $ZnSO_4$ at pH = 3 at E_1 = -1.7 V.

As described in Chapter 5, the pure Zn surface grows primarily via step flow creating an array of narrow terraces separated by step bunches. Slow-growing, misorientated islands also punctuate the surface. One such larger island visible in the lower left corner serves a nucleation site for the growth of additional layers seen in subsequent frames. Fig. 6.4(b) shows the same area after one deposition pulse in pH = 4 solution. (One pulse corresponds to passing charges equivalent

to deposition of 100 ML of Zn(II) metal.) Under this condition, *in situ* WAXS confirmed the co-deposition of Zn and ZnO. In Fig. 6.4(b), a micrometer-scale ZnO crystal is found at the location of a Zn protrusion seen in Fig. 6.4(a). However, it did not merge with the existing protrusion, and appeared to be 30° rotated with respect to be underlying Zn surface. On top of this 3D ZnO crystal, surface steps are visible and can be seen in the higher magnification AFM image in Fig. 6.4(c). A surface height profile measured across these steps is shown in Fig. 6.4(d) from which the step heights are measured to be 5.2 Å. This value is consistent with step heights on ZnO(0002) and larger than the value (4.8 Å) expected for Zn(0002). Irregular shaped islands formed on the Zn terraces between the step bunches; these islands tend to follow the shape of the terraces. From the morphology, it was difficult to determine the chemical composition of these irregular islands, but the fact that they followed the shape of the terrace makes them likely to be Zn instead of ZnO. The time-lapsed AFM images acquired during this experiment indicate that the Zn step bunches did not move during the deposition. This might be because of surface and step edge passivation by OH^- ions in pH = 4 solution. The observed changes in surface morphology with increasing pH can be attributed to the differences in the nucleation and growth kinetics of Zn and ZnO.

6.4.3 Electrodeposition of ZnO on polycrystalline substrate

I have also investigated the growth of ZnO on polycrystalline Zn surfaces. The electrodeposition process is similar to that described in Chapter 5. First, a polycrystalline Zn surface is obtained by electrodeposition of Zn in pH = 3 solution. This step results in the formation of blocky hexagonal crystallites [see Figs. 6.5(a) and 5.12(a)]. After deposition of 3300 ML of Zn, the solution pH is adjusted to 4.0, and five additional pulses are applied to the WE resulting in co-electrodeposition of Zn and ZnO. The resulting surface morphology is shown in Fig. 6.5(b). By imaging the same location in the two solutions, I could directly compare the growth morphologies.

The formation of ZnO, likely due to a different nucleation and growth behavior, caused a clear change in surface morphology. Figs. 6.5(b) and (c) show the presence of small, irregularly shaped islands, decorating the facets and edges of the existing blocky Zn crystals. These islands are likely to be ZnO and their heights vary from ~10 nm to 90 nm. That is, the ZnO islands are at least 20 layers tall. The surface features can be better visualized by 3D perspective views presented in Figs. 6.5(d) and (e). Compared to the growth of pure Zn facets from pH = 3 [Fig. 6.5(d)], the facets obtained from pH = 4 [Fig. 6.5(e)] are much rougher, likely due to the simultaneous precipitation of ZnO. The observation of ZnO islands on the Zn crystal facets demonstrates that nucleation is not the limiting step during ZnO deposition.

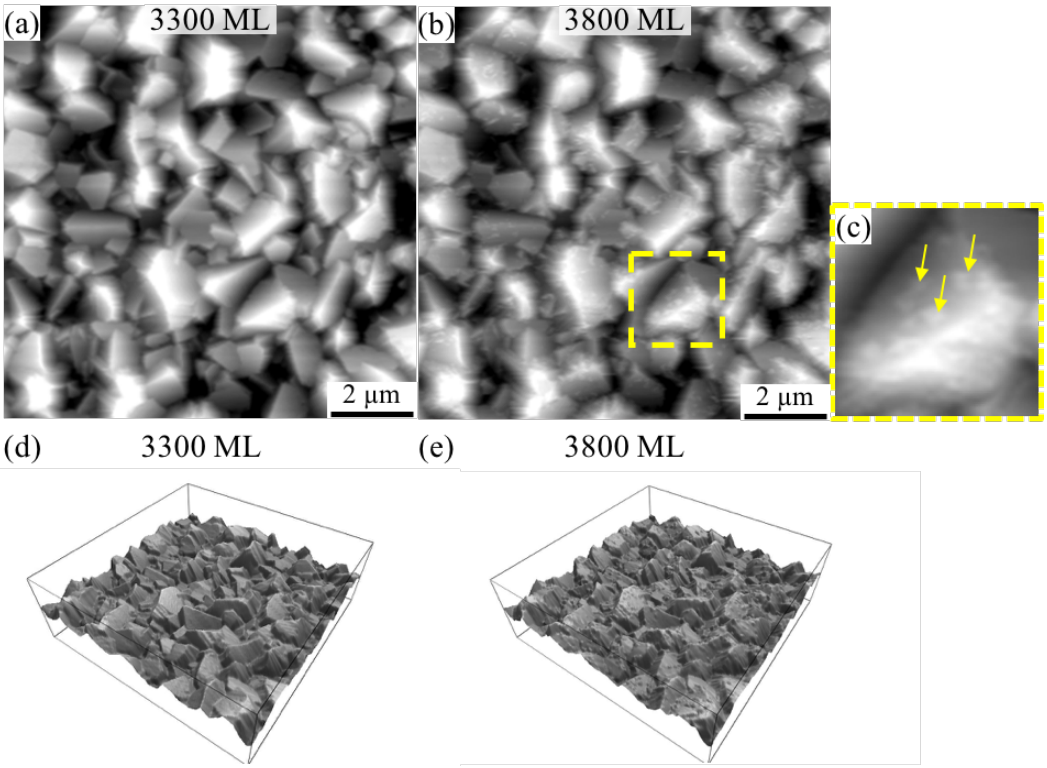

Figure 6.5, *In situ* AFM images (height channel) acquired from a polycrystalline Cu sample after electrodeposition of (a) 3300-ML-thick Zn from 0.1 M $ZnSO_4$ with pH = 3 at E_1 = -1.7 V and (b) an additional 500 ML from 0.1 M $ZnSO_4$ with pH = 4 at E_1 = -1.7 V. (c) A higher magnification image of a crystallite highlighted by a yellow dashed box in (b). (d) and (e) 3D perspective views of the images in (a) and (b), respectively.

6.4.4 *In situ* electrochemical quartz crystal microbalance (EQCM)

With the *in situ* AFM data (Fig. 6.3), I showed that only ZnO formed at E_2 = -1.465 V. In Chapter 5, I have demonstrated that the formation of ZnO at E_2 = -1.7 V is an electrochemical precipitation process, where OH^- ions are produced through reduction of dissolved oxygen and subsequently react with Zn(II) ions. In order to understand the ZnO precipitation process more precisely, I used *in situ* EQCM to study the deposition process at similar conditions with the same applied potential (E_2). The data is presented in Fig. 6.6. From the EQCM results, I observed that the ZnO deposition rate is linearly related to the potential. More specifically, the deposition rate is proportional to overpotential $\eta_{ZnO} = E_{WE} - E_{ZnO}^{expt}$. Overpotential is used to describe the driving force for electrochemical reaction away from thermodynamic equilibrium. ZnO growth rate is correlated with η_{ZnO}, because η_{ZnO} is the direct drive for ZnO to form. In addition, the ZnO growth rate is also correlated with $\eta_{Zn} = E_{WE} - E^0_{Zn}$, due to the fact that Zn electrodeposition is more likely to occur and cannot be ignored when overpotential increases.

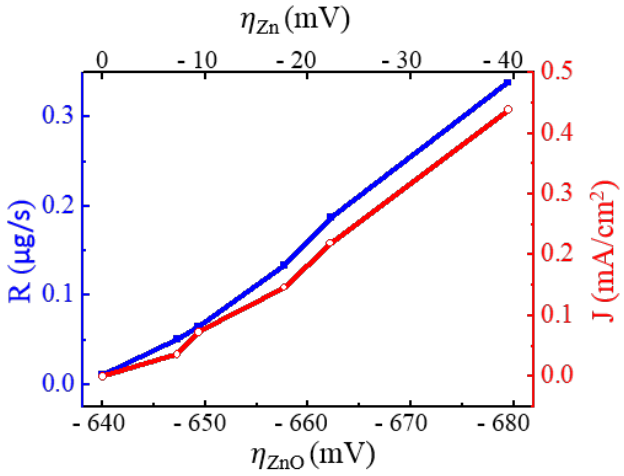

Figure 6.6, Plot of ZnO deposition rate R (blue curve) and current density J (red curve) as a function of overpotential η.

During the EQCM experiments, applied potentials are controlled around E_2. An increase in η_{ZnO} led to increasing rate of OH^- generation. Within a small range of η_{ZnO}, current density (J), the flux of charge transferred during the redox reaction for depositing ZnO, is also linearly related to the growth rate via the relation: $J = \frac{F \cdot M_{ZnO} \cdot \overline{n_e}}{A \cdot t}$,

where A is electrode area, t is time, F is Faraday's constant, $\overline{n_e}$ is the average number of electrons transferred to deposit one ZnO molecule, and $M_{ZnO} = \frac{\Delta m_{QCM}}{MW_{ZnO}}$ is the molarity of deposited ZnO.

Using data plotted in Fig. 6.6, I obtained $\overline{n_e}$ for various current densities J (Table 6.2). An average of 1.02 electrons ($\overline{n_e} = 1.02$) are transferred to the electrode to form one ZnO molecule. That is, electrodeposition of ZnO involves conversion of monovalent complex molecule into ZnO.

Table 6.2, The growth rate (R) versus overpotential (η_{OH-}).

η_{OH-} (mV)	R(μg/s)	J (mA/cm^2)	n_e
0	0.01	0	-
7.27	0.04	0.04	1.15
9.32	0.06	0.07	0.99
17.66	0.13	0.14	1.07
22.16	0.21	0.22	1.09
39.49	0.34	0.44	0.89

6.4.5 ZnO growth at lower overpotential

As discussed in the previous section, ZnO has a theoretical reducing potential at E_{ZnO}^{theory} = 0.29 V vs. MSE. The experimental reducing potential is observed at E_{ZnO}^{expt} = -0.8 V vs. MSE. Therefore, ZnO is expected to deposit at a potential lower (more negative) than E_{ZnO}^{expt}. And at a potential higher (less negative) than E_{Zn}^{0}, Zn metal is expected to oxidize and dissolve. Therefore,

as I showed in Fig. 6.1(a), when a potential E_3 is applied, preexisting Zn will dissolve and ZnO will precipitate out.

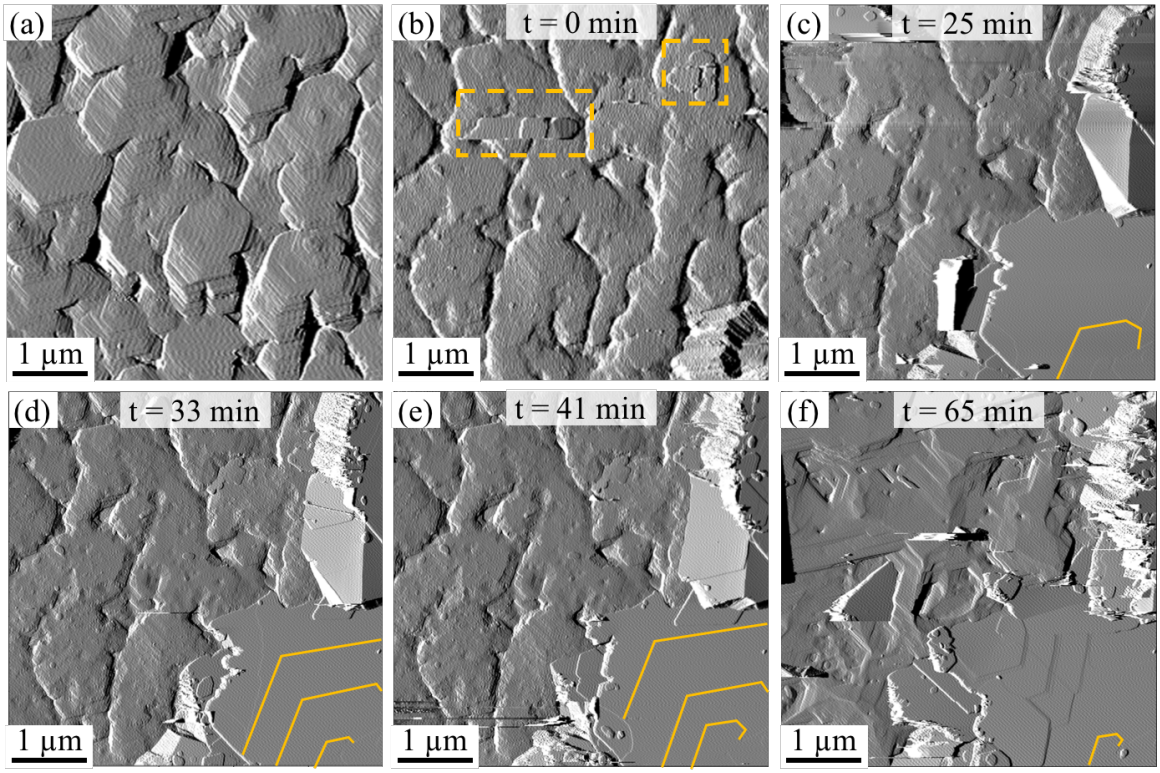

Figure 6.7, *In situ* AFM images (deflection channel) from (a) 3000-ML-thick Zn electrodeposited on Cu(111) at E_1 = -1.7 V vs. MSE in 0.1 M $ZnSO_4$ solution with pH = 3 and (b-f) the same surface with solution pH = 4. t = 0 is the time at which the electrolyte pH is changed from 3 to 4 and the potential set to E_3 = -1.42 V.

Figure 6.7 shows a series of time-lapsed AFM images acquired during the deposition of ZnO on a dissolving Zn surface. Fig. 6.7(a) shows the typical morphology of crystalline Zn(0002) surface obtained from electrodeposition of 3000 ML from 0.1 M $ZnSO_4$ solution at pH = 3 at E_1 = -1.7 V vs. MSE. At t = 0 min, electrolyte is exchanged with pH = 4 solution and potential is held at E_3 = -1.42 V vs. MSE. The current is observed to be positive indicating that Zn is getting oxidized and dissolving from the substrate. As a result, the concentration of Zn^{2+} ions in the vicinity of electrode surface increased, which facilitated the nucleation of ZnO. In Fig. 6.7(b), irregular shaped islands (yellow dashed box) of ZnO are visible but were unstable under the AFM,

similar to those observed in Fig. 6.3. However, compared to the ZnO islands formed at E_2 [Fig. 6.3(b)], the ZnO platelets yielded from lower overpotential E_3 are much bigger and more stable. Within 65 min [Fig. 6.7(f)], the original Zn surface is completely covered with ZnO films composed of flat ZnO platelets. However, during the growth of ZnO, the underlying Zn surface remained intact; Zn dissolution occurred preferentially from grain boundaries. This suggested that ZnO formation is a precipitation process that does not directly involve dissolution of Zn or transformation of Zn terraces locally into ZnO. ZnO nucleation and growth could also be observed in the time-lapsed AFM images, Figs. 6.7(c)-(f). Islands nucleated on top of basal planes and initially appear to be round or oval in shape. As they become larger, they aligned with the underneath crystal indicative of epitaxial growth of ZnO on the underlying ZnO facets. Due to the fact that nuclei formed randomly on flat facets, I speculate that ZnO colloids first form in the solution and subsequently attach to the existing surface.

6.4.6 Discussion

This chapter discussed the electrodeposition of ZnO carried out in different potential ranges. As I demonstrated in Fig. 6.1(a), at a potential more negative than E^0_{Zn} (e.g., E_1), both Zn and ZnO co-electrodeposit. At a potential slightly lower but very close to E^0_{Zn}, such as, E_2, ZnO precipitated without Zn electrodeposition. At a more positive potential with respect to E^0_{Zn}, such as, E_3, Zn is observed to dissolve while ZnO formation is facilitated.

In situ experimental results

The *in situ* WAXS data demonstrated that ZnO formed as a secondary phase in pH = 4 solution, while Zn is the only electrodeposition product from pH = 3 solution. In pH = 4, the both Zn and ZnO are co-electrodeposited from solution. For solutions with pH higher than 4, I expect that ZnO forms in the same manner. $Zn(OH)_2$ was not observed using *in situ* WAXS indicating

that crystalline $Zn(OH)_2$ is not a precursor for ZnO electrodeposition. However, the presence of amorphous $Zn(OH)_2$ transforming to ZnO cannot be ruled out.

In situ AFM enabled direct visualization of ZnO electrodeposition process. On single-crystalline Zn(0002) surfaces, ZnO formation is observed at E_2, where ZnO is verified as the only deposition product. During *in situ* AFM investigation, the observation of incomplete hexagonal crystals demonstrated that ZnO is directly formed through electrodeposition instead of transforming from crystalline $Zn(OH)_2$ precursor because $Zn(OH)_2$ is known to be orthorhombic or tetragonal instead of hexagonal structure. During ZnO formation, I did not observe any motion of the Zn steps. This verified my expectation that Zn growth and dissolution are hindered at applied potential E_2. *In situ* AFM studies of ZnO electrodeposition are also carried out on polycrystalline Cu substrates. ZnO formation adopted a different growth mechanism and altered the surface morphology. A discussion on overpotential is given based on various deposition morphologies acquired at different potentials. At a low overpotential, electrodeposited ZnO is observed to form a smoother film, while Zn dissolution occurs at the grain boundaries.

The growth mechanism of ZnO

Based on the AFM observations in combination with *in situ* EQCM data, I present the following ZnO electrodeposition mechanism. As pointed in Table 6.2, electrodeposition of one molecule of ZnO involves transfer of one electron through the circuit. In order to understand this process, first consider the reactants in Zn redox reactions. Zn hydrated complex molecules are known to have multiple forms and the concentration of soluble hydrated species varies with pH. In basic solutions, Li *et al.* showed that the $Zn(OH)_4^{2-}$ tetrahedra are the major species and the growth unit for ZnO. In order to convert a monovalent complex, I propose that $Zn(OH)^+$ plays an important role. The formation of $Zn(OH)^+$ is simply a hydration process:

$$Zn^{2+} + H_2O \longrightarrow Zn(OH)^+ + H^+. \quad [6.6]$$

One additional electron will cause $Zn(OH)^+$ to precipitate ZnO as

$$Zn(OH)^+ + e^- \longrightarrow ZnO, \quad [6.7]$$

which can be expressed as a combination of two following reactions:

$$O_2 + 2H_2O + 4e^- \longrightarrow 4OH^- \quad [6.8]$$

$$Zn(OH)^+ + e^- + \tfrac{1}{4}O_2 \longrightarrow ZnO + \tfrac{1}{2}H_2O. \quad [6.9]$$

Thus, I propose $Zn(OH)^+$ ion as the growth unit for the formation of ZnO in near neutral solutions.

6.5 Conclusions

From the *in situ* AFM analysis, I first visualized the electrodeposition of ZnO on Zn surfaces. From the observed morphology, I conclude that intermediate $Zn(OH)_2$ is not a precursor for the formation of ZnO during electrodeposition. Furthermore, with the proof from *in situ* WAXS, I showed that Zn is the only electrodeposition product from pH = 3 solution. However, ZnO precipitated simultaneously with Zn from pH = 4 solution. Therefore, I conclude that ZnO co-electrodeposited with Zn. *In situ* AFM is also used to investigate the growth morphology as a function of overpotential. I further demonstrated through *in situ* AFM experiments carried out in pH-controlled solutions that ZnO formation on an existing Zn surface altered the surface morphology due to the fact ZnO formation adopted a different nucleation and growth mechanism.

Chapter 7

7 Conclusions and Future work

7.1 Conclusions

Electrodeposition of Zn and ZnO have received attention because of their broad applications in energy storage and optoelectronic industries. The study of Zn electrodeposition allows a better understanding of dendrite formation and will facilitate the development of reliable rechargeable zinc-air batteries. The study of ZnO electrodeposition aims at achieving controllable morphologies and electronic properties, which will lead to various device designs.

This dissertation summarized my study on Zn and ZnO growth kinetics using a series of *in situ* characterization techniques, including *in situ* optical microscopy, atomic force microcopy (AFM), wide-angle X-ray scattering (WAXS), and electrochemical quartz crystal microbalance (EQCM). Chapters 3 and 4 utilized *in situ* optical microscopy as the primary approach in the study of Zn dendrite growth kinetics in a thin-layer liquid cell geometry. In these centimeter-scale cells, the Zn dendrites formed at a similar dimension to those formed in real zinc-air batteries. Therefore, understanding the dendrite growth dynamics in these cells will help develop new cell designs for improving the performance of rechargeable zinc-air batteries. Chapter 5 discussed *in situ* AFM studies of Zn electrodeposition kinetics. Studies focused on the nucleation and surface morphological evolution during the thin film deposition prior to dendritic growth. Chapter 6 utilized similar methodology but different chemistry to investigate ZnO electrodeposition. The motivation for me to study ZnO electrodeposition is two-fold: ZnO formation has always been observed during Zn electrodeposition in both basic and acidic (near neutral) solutions and electrodeposition of ZnO is considered attractive as a synthesis approach.

From the *in situ* optical microscopy experiments, I observed the growth of dendrites in various electrolyte concentrations with different macroscopic morphologies, such as diffusion limited aggregates (DLA), dense branched, and needle-like structures. However, the microstructures within all these structures exhibited the same crystalline symmetry of Zn. Based upon these results, I conclude that the growth of Zn electrodeposited dendrites is an interplay of diffusion/electrical Laplacian fields and anisotropic crystal growth. The effect of Laplacian fields is more pronounced in higher dimensions at lower concentrations, while the crystal anisotropy dominates the morphological evolution at higher concentrations. During the study of dendritic growth, I also observed oscillatory growth of Zn dendrites. Real-time optical microscopy movies show that the oscillation of growth rate is synchronized with electrical current fluctuation. A detailed morphological study revealed that the oscillatory Zn dendrites are composed of two sets of {0001}-oriented crystals tilted ~18° with respect to each other. I postulated a growth model based on the observations of growth behavior and morphological evolution.

From the AFM analysis, I first studied the growth kinetics of Zn during electrodeposition. On polycrystalline Cu substrates, I observed that the growth of Zn film with randomly oriented grains. On single-crystalline Cu(111) substrates, Zn layers preferentially grew via step-flow when the step density is high and via the formation of 2D islands or spiral steps when the step density is low. I also demonstrated that the Zn films deposited on single-crystalline Cu(111) are single-crystalline with {0002} orientation normal to the substrate. I discussed the effect of pH on film morphologies. As pH increased from 3 to 5, high aspect ratio flakes are observed along with the typical blocky electrodeposits. Based on energy dispersive spectra, I suggest that these flakes are made of ZnO. In solutions with pH = 4 and higher, I expect co-electrodeposition of Zn and ZnO. *In situ* EQCM is used to probe the process of ZnO formation. ZnO electrodeposition is found to

involve two steps: oxygen reduction and ZnO precipitation. The formation of ZnO in solutions with pH ≥ 4 is confirmed using *in situ* WAXS. Using *in situ* AFM, I studied the details of ZnO electrodeposition on Zn surfaces. On single-crystalline substrates, I observed nucleation events of ZnO. On polycrystalline substrates, the formation of ZnO altered the growth and morphologies of Zn because the ZnO growth mode is different -- the nuclei of ZnO form in solution. Furthermore, a morphological study based on overpotential is carried out using *in situ* AFM. I demonstrated that at a lower overpotential, where Zn was dissolving, ZnO growth could be facilitated due to a higher Zn ion concentration near the surface. Finally, I postulated a growth mechanism and a growth unit for ZnO.

To sum up, this dissertation addresses fundamental growth kinetics of Zn and ZnO during electrodeposition. *In situ* techniques are employed to perform direct observation and measurements, which provide new insights into the electrodeposition growth mechanisms.

7.2 Future work

This dissertation provided basic information for future extensive and systematic studies of Zn and ZnO electrodeposition. The direct observation of the nucleation and growth kinetics during Zn and ZnO electrodeposition is enlightening in terms of resolving Zn dendrite formation and obtaining controlled ZnO nanostructures.

Future work on Zn electrodeposition will be focused on addressing the morphological transitions from films to dendritic structures. The initiation of dendrite has been one of the ongoing challenges for mechanistic study of dendritic growth. *In situ* AFM will help to understand the early stage growth of dendrite at a more fundamental level. With proper control over the AFM technique and the growth conditions, the initiation of dendrite is expected to be tunable, which in turn allows more systematic studies or even mathematical modelling. In addition, the nucleation behavior of

Zn has unrevealed interesting aspects. For example, whether the nucleus forms on surface defects (heterogeneous nucleation) and whether the misaligned nucleus overcomes a lower nucleation barrier to form. Additional design and control are required to further discover all the aspects associated with Zn nucleation during electrodeposition.

Future work on ZnO electrodeposition will be focused on the studies of the roles of additives as well as impurities. Additives and impurities are known to have an impact on the ZnO morphology and band gap. However, mechanistic analysis coupled with experimental validation have not been conducted to-date. The effect of impurities on the ZnO growth kinetics postulated by literature, however, is never demonstrated. The work done in this dissertation set the foundation for growth kinetics study involving impurities. An extended study on electrolyte chemistry will be required based on the current experimental condition. AFM will be used as the primary experimental approach in direct understanding the impact of additive/impurity ions on ZnO steps. As a result, understanding the mechanisms of various additives/impurities will facilitate establishing recipes targeting various morphology and optoelectronic properties.

References

1. F. Beck and P. Rüetschi, Electrochimica Acta **45** (15), 2467-2482 (2000).

2. J. S. Lee, S. Tai Kim, R. Cao, N. S. Choi, M. Liu, K. T. Lee and J. Cho, Advanced Energy Materials **1** (1), 34-50 (2011).

3. J. Fu, Z. P. Cano, M. G. Park, A. Yu, M. Fowler and Z. Chen, Advanced Materials (2016).

4. G. Wranglén, Electrochimica Acta **2** (1-3), 130-143 (1960).

5. V. Fleury, Nature **390** (6656), 145 (1997).

6. N. Hecker, D. Grier, L. Sander, R. Laibowitz, B. Mandelbrot and D. Passoja, Materials Research Society, University Park, PA (1985).

7. Ü. Özgür, Y. I. Alivov, C. Liu, A. Teke, M. Reshchikov, S. Doğan, V. Avrutin, S.-J. Cho and H. Morkoc, Journal of applied physics **98** (4), 11 (2005).

8. M. Skompska and K. Zarębska, Electrochimica Acta **127**, 467-488 (2014).

9. A. Kołodziejczak-Radzimska and T. Jesionowski, Materials **7** (4), 2833-2881 (2014).

10. Y. Li and H. Dai, Chemical Society Reviews **43** (15), 5257-5275 (2014).

11. C. M. López and K.-S. Choi, Langmuir **22** (25), 10625-10629 (2006).

12. J. S. Langer, Reviews of Modern Physics **52** (1), 1 (1980).

13. S. Ohta, Research of Pattern Formation, 217-238 (1994).

14. R. Naybour, Electrochimica Acta **13** (4), 763-769 (1968).

15. J. W. Diggle, R. J. Fredericks and A. C. Reimschuessel, Journal of Materials Science **8** (1), 79-87 (1973).

16. R. Wang, D. Kirk and G. Zhang, Journal of The Electrochemical Society **153** (5), C357-C364 (2006).

17. B. Pal and D. Chakravorty, The Journal of Physical Chemistry B **110** (42), 20917-20921 (2006).

18. H. Pan, H. Sun, C. Poh, Y. Feng and J. Lin, Nanotechnology **16** (9), 1559 (2005).

19. D. G. Grier, K. Allen, R. S. Goldman, L. M. Sander and R. Clarke, Physical review letters **64** (18), 2152 (1990).

20. M. Matsushita, M. Sano, Y. Hayakawa, H. Honjo and Y. Sawada, Physical review letters **53** (3), 286 (1984).

21. E. Ben-Jacob and P. Garik, Nature **343** (6258), 523-530 (1990).

22. J. M. Huth, H. L. Swinney, W. D. McCormick, A. Kuhn and F. Argoul, Physical Review E **51** (4), 3444 (1995).

23. J.-N. Chazalviel, M. Rosso, E. Chassaing and V. Fleury, Journal of Electroanalytical Chemistry **407** (1-2), 61-73 (1996).

24. D. Grier, E. Ben-Jacob, R. Clarke and L.-M. Sander, Physical review letters **56** (12), 1264 (1986).

25. F. Sagués, M. Q. López-Salvans and J. Claret, Physics Reports **337** (1), 97-115 (2000).

26. Y. Sawada, A. Dougherty and J. P. Gollub, Physical review letters **56** (12), 1260 (1986).

27. C. Léger, J. Elezgaray and F. Argoul, Journal of Electroanalytical Chemistry **486** (2), 204-219 (2000).

28. J.-N. Chazalviel, Physical review A **42** (12), 7355 (1990).

29. P. Garik, D. Barkey, E. Ben-Jacob, E. Bochner, N. Broxholm, B. Miller, B. Orr and R. Zamir, Physical review letters **62** (23), 2703 (1989).

30. F. Suda, S.-A. Kawauchi and M. Ito, Japanese journal of applied physics **42** (10R), 6726 (2003).

31. G. Gonzalez, G. Marshall, F. V. Molina, S. Dengra and M. Rosso, Journal of the Electrochemical Society **148** (7), C479-C487 (2001).

32. T. N. Mhíocháin and J. Coey, Physical Review E **69** (6), 061404 (2004).

33. T. N. Mhıocháin, G. Hinds, A. Martin, A. Lai, L. Costiner and J. Coey, Electrochimica Acta **49** (27), 4813-4828 (2004).

34. V. Fleury, M. Rosso and J.-N. Chazalviel, Physical Review A **43** (12), 6908 (1991).

35. R. Suter and P.-Z. Wong, Physical Review B **39** (7), 4536 (1989).

36. F. Argoul, J. Huth, P. Merzeau, A. Arneodo and H. L. Swinney, Physica D: Nonlinear Phenomena **62** (1-4), 170-185 (1993).

37. S. Nakanishi, K. Fukami, T. Tada and Y. Nakato, Journal of the American Chemical Society **126** (31), 9556-9557 (2004).

38. K. Fukami, S. Nakanishi, H. Yamasaki, T. Tada, K. Sonoda, N. Kamikawa, N. Tsuji, H. Sakaguchi and Y. Nakato, The Journal of Physical Chemistry C **111** (3), 1150-1160 (2007).

39. J. A. Switzer, C.-J. Hung, L.-Y. Huang, F. S. Miller, Y. Zhou, E. R. Raub, M. G. Shumsky and E. W. Bohannan, Journal of materials research **13** (4), 909-916 (1998).

40. F. Argoul and A. Kuhn, Journal of Electroanalytical Chemistry **359** (1-2), 81-96 (1993).

41. K. Fukami, S. Nakanishi, T. Tada, H. Yamasaki, S.-I. Sakai, S. Fukushima and Y. Nakato, Journal of the Electrochemical Society **152** (7), C493-C497 (2005).

42. K. Fukami, S. Nakanishi, S.-I. Sakai and Y. Nakato, Chemistry letters **32** (6), 532-533 (2003).

43. M. Wang and N.-B. Ming, Physical Review A **45** (4), 2493 (1992).

44. S. Wang, K.-Q. Zhang, Q.-Y. Xu, M. Wang, R.-W. Peng, Z. Zhang and N.-B. Ming, Journal of the Physical Society of Japan **72** (6), 1574-1580 (2003).

45. T. Liu, S. Wang, M. Wang, R. W. Peng, G. B. Ma, X. P. Hao and N.-B. Ming, Surface and interface analysis **38** (6), 1019-1023 (2006).

46. T. Liu, S. Wang, Z.-L. Shi, G.-B. Ma, M. Wang, R.-W. Peng, X.-P. Hao and N.-B. Ming, Physical Review E **75** (5), 051606 (2007).

47. S. Zhong, Y. Wang, M. Wang, M.-Z. Zhang, X.-B. Yin, R.-W. Peng and N.-B. Ming, Physical Review E **67** (6), 061601 (2003).

48. F. T. Smith, Applied Physics Letters **43** (12), 1108-1110 (1983).

49. J.-J. Wu and S.-C. Liu, Advanced materials **14** (3), 215 (2002).

50. D. Montenegro, A. Souissi, C. Martínez-Tomás, V. Muñoz-Sanjosé and V. Sallet, Journal of Crystal Growth **359**, 122-128 (2012).

51. H. Fujisawa, C. Kobayashi, S. Nakashima and M. Shimizu, Journal of the Korean Physical Society **62** (8), 1164-1168 (2013).

52. W.-J. Li, E.-W. Shi, W.-Z. Zhong and Z.-W. Yin, Journal of crystal growth **203** (1), 186-196 (1999).

53. J. Yu, B. Huang, X. Qin, X. Zhang, Z. Wang and H. Liu, Applied Surface Science **257** (13), 5563-5565 (2011).

54. S. A. Kamaruddin, K.-Y. Chan, H.-K. Yow, M. Z. Sahdan, H. Saim and D. Knipp, Applied Physics A **104** (1), 263-268 (2011).

55. M. Izaki and T. Omi, Applied Physics Letters **68** (17), 2439-2440 (1996).

56. B. Canava and D. Lincot, Journal of applied electrochemistry **30** (6), 711-716 (2000).

57. J. Elias, R. Tena-Zaera and C. Lévy-Clément, Thin Solid Films **515** (24), 8553-8557 (2007).

58. T. Pauporté, D. Lincot, B. Viana and F. Pellé, Applied Physics Letters **89** (23), 233112 (2006).

59. J. Elias, R. Tena-Zaera and C. Lévy-Clément, Journal of Electroanalytical Chemistry **621** (2), 171-177 (2008).

60. J. Lin, W. Fu, L. Jing, Y. Qu and Z. Li, Science China Chemistry **53** (8), 1732-1736 (2010).

61. L. Xu, Y. Guo, Q. Liao, J. Zhang and D. Xu, The Journal of Physical Chemistry B **109** (28), 13519-13522 (2005).

62. S. Peulon and D. Lincot, Advanced Materials **8** (2), 166-170 (1996).

63. A. Goux, T. Pauporté, J. Chivot and D. Lincot, Electrochimica Acta **50** (11), 2239-2248 (2005).

64. J. Lee and Y. Tak, Electrochemical and Solid-State Letters **4** (9), C63-C65 (2001).

65. H. Wang, Y. J. Chen, F. Xu, H. N. Cui, B. Marí, M. Mollar and R. Wang, presented at the Advanced Materials Research, 2014 (unpublished).

66. G.-W. She, X.-H. Zhang, W.-S. Shi, X. Fan, J. C. Chang, C.-S. Lee, S.-T. Lee and C.-H. Liu, Applied physics letters **92** (5), 053111 (2008).